CAUSES OF DIURNAL GROUND MOVEMENTS AT OMOKOROA, NEW ZEALAND

A thesis submitted in partial fulfilment

of the requirements for the degree

of

Master of Science (Earth Sciences)

at

The University of Waikato

by

Tyler Manderson

THE UNIVERSITY OF
WAIKATO
Te Whare Wānanga o Waikato

2017

ABSTRACT

This study investigated processes acting on the Bramley Drive Landslide, located on the Omokoroa Peninsula. The landslide, first failed in 1979, and has become an important field site for assessing the processes affecting sensitive volcanic soils in the Bay of Plenty region that contribute to slope failure. Researchers from the University of Waikato and the University of Bremen, Germany observed daily displacements in a borehole inclinometer located on site that were attributed to amplification of Earth tide movements.

Potential factors contributing to exaggerated diurnal solid Earth tide strains were investigated, primarily: temperature, rainfall, Earth tides and microseisms. Measurements of displacements and forcing processes were obtained using a 3-axis 0.65 g precision accelerometer/seismometer, borehole inclinometer and weather station.

The accelerometer data indicate that microseisms, consistent with breaking waves on the open coast of Matakana Island, and a diurnal thermal component occur within the top 5cm of the ground profile. The measured ground accelerations are greatest in warmer summer months due to the larger changes in temperature throughout a day associated with higher insolation and reduced soil moisture.

The displacements within the borehole are a linear function of depth, but involve a series of sharp deviations, or steps, throughout the 42 m length measured. These steps coincide with boundaries between different stratigraphic units, usually where there is a change in soil type and soil strength. Therefore, the effects of the horizontal strain due to the solid Earth tide is exaggerated by differential and lagged displacement of the units.

This suggests that Earth tidal stress, may cause minor (usually temporary) shear surfaces at depths that may be the final trigger for an "at risk" slope that is already preloaded and ready to fail. Several examples where this may be a factor were identified, including all the events at Bramley Drive with a known time of failure. Failure occurred when the rate of vertical Earth tide displacement peaked close to the time of maximum horizontal displacement, which corresponds to a change in the direction of the stress caused by the combined Moon and Sun tide generating potential. Predicting the time of slope failure may be beneficial both locally and globally.

ACKNOWLEDGEMENTS

I would first like to thank my thesis chief supervisor Dr Willem de Lange for suggesting such an interesting topic. As with many who I explain my thesis to, I too had no clue what Earth tides were. It was a goal of mine for my thesis to research something that was interesting while also being distinct, and I feel this topic far exceeded my expectations.

I am grateful to Dr Vicki Moon for listening to, and encouraging my intention to return to University and begin my graduate studies after years of working.

I would also like to thank the Western Bay of Plenty Council for giving myself access to the Bramley Drive site, as well as Deutsche Forschungsgemeinschaft (DFG) via the Integrated Coastal Zone and Shelf Sea Research Training Group INTERCOAST and the MARUM Center for Marine Environmental Science at the University of Bremen for installation of inclinometer.

A massive thanks to Aleesha McKay, Francesca Spinardi, Benjamin Campbell, Tom Robertson, Rosie Hughes, Alex Harpur and Alyosha Podrumac, who all braved the miserably wet and windy weather when helping me record 25 hours of continuous measurements every half an hour, giving them no time to relax.

Finally, a massive thanks to my parents and sisters for supporting me through my studies.

Thank you, thank you, papa bless…

TABLE OF CONTENTS

LIST OF FIGURES

LIST OF TABLES

CHAPTER 1

INTRODUCTION

1.1 BACKGROUND

The Bramley Drive Landslide located on the Omokoroa Peninsula, has become the poster child for land instability caused by sensitive volcanic soils in the Bay of Plenty. Multiple failures have occurred at the site, along with other similar failures across other coastal cliffs in the region. The initial failure in August 1979 resulted in an astounding 20 m retreat of the cliff, with a heavy period of rain days before the failure deemed responsible for the activation. Reactivation of the landslide has since occurred in the past few years and multiple reports defining the ground conditions (Gulliver & Houghton, 1980; Moon *et al.*, 2013; Milner & Taylor, 2014; Moon *et al.*, 2015a), likely failure mechanics (Gulliver & Houghton, 1980; Keam & Milner, 2011; Milner & Taylor, 2014) and the mineralogy of the soils (Wyatt, 2009; Keam & Milner, 2011; Cunningham, 2012; Moon *et al.*, 2013; Moon *et al.*, 2015b; Steinborn, 2015; Kluger *et al.*, 2016; Mills, 2016) have been completed.

Since 2012 the Bramley Drive Landslide has been continually monitored by the University of Waikato with regular laser scanning to measure cliff degradation, piezometer, accelerometer and borehole inclinometer measurements along with an installed weather station recording temperature, wind speed and rainfall. A recent conference presentation at the 12th Australia New Zealand Conference on Geomechanics (Moon *et al.*, 2015a) provided a broad overview of this recent monitoring, including initial laser scan, inclinometer, cone penetration testing and pore water pressure results.

The borehole inclinometer measurements recorded between July 2013 and January 2014 returned very interesting results that had not been observed in any previous report of the landslide. While no developing shear surface was present, varying degrees of ground movement were recorded throughout the 43 m deep borehole. These variations were presumed to be formed by solid Earth tides, which are the semi-diurnal movements in the Earth due to the gravitational attraction of the Moon and Sun However, the measured strain was two orders of magnitude greater than predicted

Earth tide strain, with a defined elliptical motion. With measured Earth tides removed, tilted apparent diurnal motion caused by an unknown process was still observed.

This exaggeration of the Earth tide, if understood, can become an important variable for future land slope analysis in not just regional soil conditions, but any slope that partly consists of volcanic derived sensitive soils.

1.1.1 Bramley Drive Landslide, Omokoroa

1.1.1.1 Location and geomorphology

The Bramley Drive Landslide that was analysed in this thesis is located on the western margin of the Omokoroa Peninsula (Figure 1.1) on steep costal bluffs, 33 m above high tide (Moon et al., 2015a). The headscarp is steep, ranging between 50˚and 60˚ and reaching approximately 70˚ in the southern portion. The steep scarp begins to flatten out at approximately 25 m below the top of slope due to the extensive debris lobe formed by previous site failures (Figure 1.2-left).

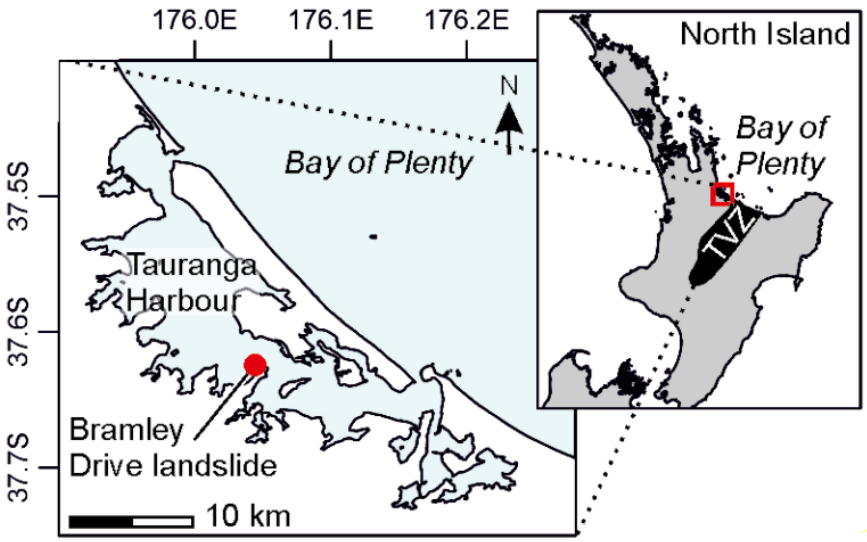

Figure 1.1: Map of Tauranga Harbour, New Zealand, with Bramley Drive Landslide Location (Kluger *et al.*, 2016).

The landslides debris lobe extends approximately 100m into the intertidal sand flats on the shore platform, where erosion caused by the tides is slowly removing the debris into the harbour (Figure 1.2–right). All full geomorphic map of the Bramley Drive Landslide can be found in Mills (2016).

Figure 1.2: Photos of Bramley Drive Landslide. Looking south from top of slope – 30th of July 2015 (left), looking northeast from top of slope looking down at runout – 14th of November 2016 (right).

1.1.1.2 Geology

Steinborn (2015) and Kluger *et al.* (2016) analysed a 43 m long sediment core, Omok-1, that was drilled in unfailed material behind the headscarp in March 2013. The sequence, consists of volcanic tephras approximately 40 m thick, underlain by Matua Subgroup Lignite. The tephras are split into four sequences, the lowermost being the Te Puna Ignimbrite (ca. 0.93 Ma) which comprises poorly graded silty sand. This is overlain by the Pahoia Tephras (ca. 0.93-0.35 Ma) which are informally split into upper and lower units by distinct paleosols, with the lower Pahoia Tephra comprising of typically pale coloured rhyolitic flow deposits that are likely in near permanent saturation and displaying high sensitivity and porosity that has been associated with landsliding throughout the Tauranga area (Moon et al., 2013). At the Bramley Drive site, an especially sensitive, clay-rich layer 0.3 m thick has been interpreted by Kluger *et al.* (2016) and is seen as the material driving slope movement due to its mineralogy and high sensitivity (Figure 1.3).

Successions of younger altered tephras named the Hamilton Ash beds (ca. 0.35-0.05 Ma) and more recent Quaternary ashes (< ca. 0.05 Ma) overlie the upper Pahoia Tephras, separated by defined paleosols.

Various reports and theses describe the geology in detail (Gulliver & Houghton, 1980; Briggs *et al.*, 1996; Oliver, 1997; Wyatt, 2009; Arthurs, 2010; Keam & Milner, 2011; Cunningham, 2012; Moon *et al.*, 2013; Moon *et al.*, 2015a; Moon *et al.*, 2015b; Steinborn, 2015; Kluger *et al.*, 2016; Mills, 2016).

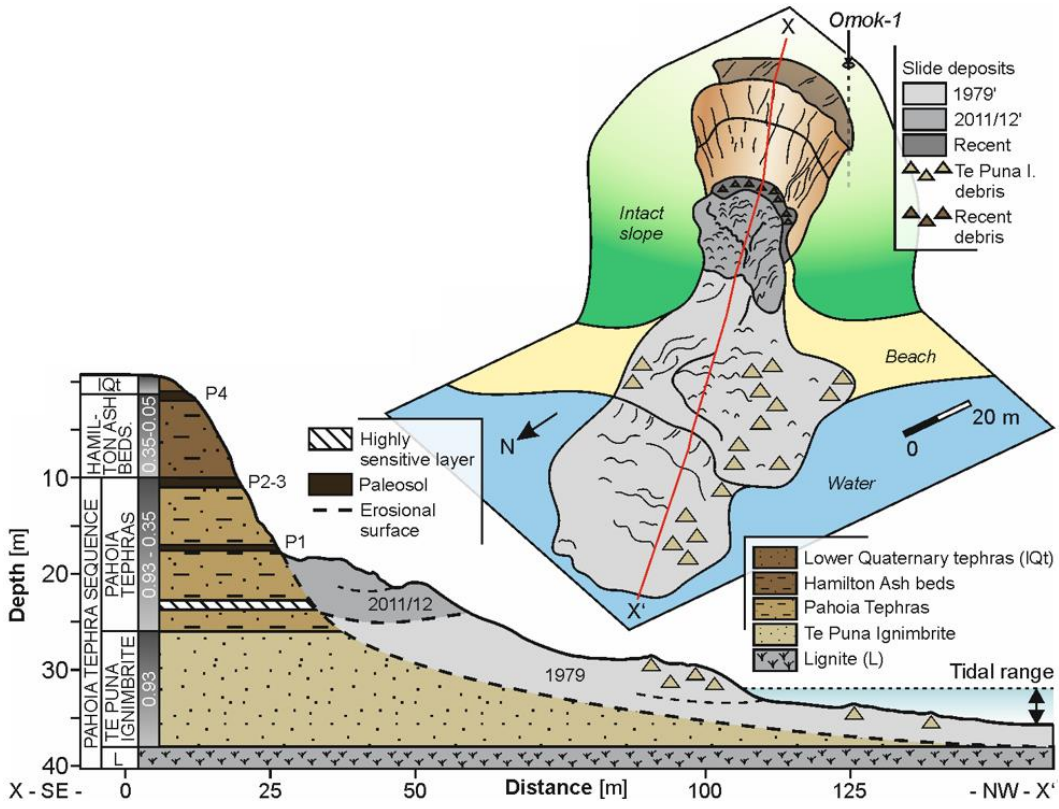

Figure 1.3: Cross-sectional (X-X') morphology and geology for the Bramley Drive landslide (Kluger *et al.*, 2016).

1.2 KNOWLEDGE GAP

Literature regarding an exaggeration of the Earth tide caused by unknown cyclic factors, resulting in ground movement was not encountered while preparing for this literature review. The hypothesis of increased cyclic loading and differential movement within sensitive volcanic soils by diurnal and semi diurnal processes, many of which are usually identified as background noise in seismic records is seen as a large knowledge gap when analysing a slope stability.

1.3 AIMS AND OBJECTIVES

The overarching aim of this thesis is to unravel the causes of exaggerated diurnal solid Earth tide strains at the Bramley Drive Landslide. Objectives to achieve this goal are:

1. Review previous reports and tests completed at the Bramley Drive site;
2. Give unbiased observations of data retrieved from the accelerometer, borehole inclinometer and weather station, to find possible cyclic trends that affect ground movement at the Bramley Drive site;
3. Interpret data using suitable statistical packages in an attempt to validate observations in the accelerometer and weather station;

4. Review Earth tide theory, local magnitude, and its effects on the installed borehole inclinometer in regards to observed semi-diurnal displacements;
5. Recognise what dynamic factors increase or decrease cyclic loading in the sensitive soils;
6. Relate finding to landslides worldwide;
7. Develop a hypothesis for the diurnal factors affecting the Bramley Drive site, and determine which contribute the most in regards to displacement observed on site.

1.4 THESIS ORGANISATION

Chapter 2 reviews literature of the Bramley Drive Landslide events, including the likely factors contributing to the failure events. Cyclic and non-cyclic processes that were proposed as factors that may contribute to diurnal ground movements at the site are also reviewed.

The instruments used to observe ground movement on site are described in Chapter 3, which includes the thesis methodology and observations of data collected, beginning mid-2013 to late 2016.

Interpretation of the collected data is in Chapter 4, where statistical analysis, as well as observations, are used to form hypotheses on what diurnal factors are causing ground movement, as well as their contribution. In Chapter 5 these interpretations are then used to suggest possible links in regards to slope failure timing worldwide.

Chapter 6 concludes the study, presenting summaries for the diurnal process that are proposed to contribute to diurnal displacement at the Bramley Drive site, followed by recommendations for further research.

CHAPTER 2

LITERATURE REVIEW

2.1 INTRODUCTION

The Bramley Drive Landslide, beginning in the late 1970s, has been well documented in regards to failure history and its proposed cause of failure. In this chapter, the failure history of the Bramley Drive Landslide will be summarised, along with a review of the causes of failure proposed by subsequent studies. Cyclic processes that may or may not also affect the sites stability are investigated due to previous works finding the possibility of diurnal processes acting on the site. Recent research involving monitoring of the site using various approaches beginning in late 2012, will also be reviewed below.

2.2 Previous Site Failures

Two large historic slope failures have contributed to the geomorphology of the site and are summarised below.

2.2.1 1979

The first large failure observed at the site (Figure 2.1) occurred at a time of prolonged heavy rainfall. Early indications of the developing failure occurred just minutes before the initial failure on the 9th of August 1979, when local residents noticed cracks within their lawns parallel to the bluff face. Approximately fifteen minutes later a segment of sea cliff 60 m wide and about 16 m deep failed, taking with it a reserve located in front of two homes (Gulliver & Houghton, 1980). Eyewitness accounts suggest the failure was catastrophic, moving as a single mass, entering the sea at a high velocity, and extending 150 m into the harbour. Further failures occurred over the next few days, removing up to 4 m further from segments of the cliff face resulting in a total of approximately 20 m recession of the 60 m wide failure (Gulliver & Houghton, 1980). Five houses were subsequently removed due to structural damages or endangerment of landslides (Figure 2.1).

10/08/1979 - Initial failure

(Gulliver & Houghton, 1980).

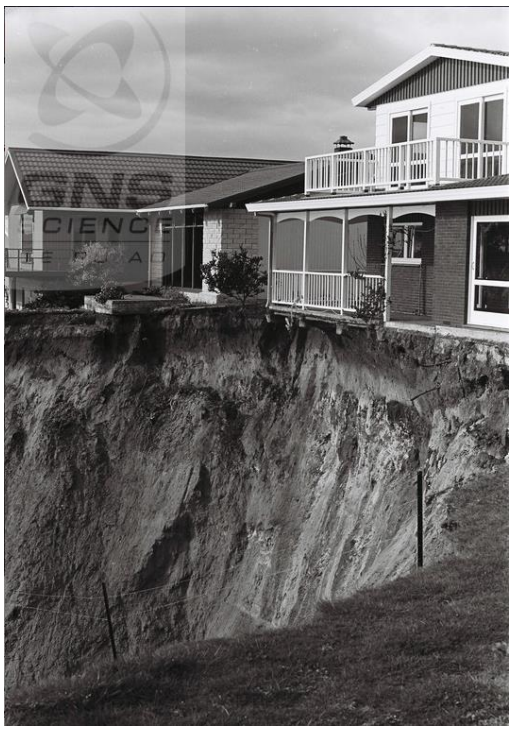

24/08/1979 – After further failures

(GNS Science, n.d)

Photo taken in "October" (1979), curtesy of D.J. Lowe. Note that concrete foundations of houses visible.

Figure 2.1: Photos following the 1979 Bramley Drive Landslide

After the failures a land stability investigation was conducted by Tonkin & Taylor (T&T) and the New Zealand Geological Survey (Gulliver & Houghton, 1980). The face of the landslide was examined, and the shape of its surface was described as a tight arc with hairline cracks parallel to its face. It was observed that the welded Te Puna Ignimbrite had a much greater thickness on either end of the failure suggesting that at the failure location a pre-existing valley cut through the ignimbrite, which had been infilled by the sensitive Pahoia Tephras.

2.2.2 2011 to present

Heavy rainfall caused the headscarp to reactivate again on the 11th of May 2011 (Keam & Milner, 2011). This resulted in a further 6 m regression of the headscarp and partial inundation of the original failure deposit located on the shore platform. The failure only affected the top 20 m of the face, resulting in a pronounced bench that coincides with the location of the sensitive soils observed within the Pahoia Tephra.

14/02/2007 – Before 2011 failure **27/01/2012** – After 2011 failure

31/08/2012 – After 2012 failures **17/11/2015** – Most aerial recent imagery

Figure 2.2: Aerial imagery of the Bramley Drive Landslide before, during and after the 2011-2012 slope failures. Note: scale in meters (images from Google Earth).

Since the failure in 2011 (Figure 2.2), the headscarp had further reactivations in 2012 causing an additional 4 m of cliff regression. Although some minor movement has occurred on the northern flank, no significant reactivations have been observed since 2012 (Moon *et al.*, 2015a; personal observations).

2.3 PROPOSED CAUSES OF FAILURE

2.3.1 Sensitive soils

In the Northern Hemisphere, sensitive soils are synonymous with glacial retreat and the deposition of illite dominant clay within shallow marine clay terraces (Torrance, 2014). In New Zealand, sensitive soils are predominantly found in rhyolitic (silica-rich) pyroclastic materials, including fall and flow deposits that can be observed across most of the North Island of New Zealand. In the Bay of Plenty region of the North Island, sensitive soils are responsible for large landslides and infrastructure damage due to the halloysite clay minerals within the volcanic soil that have high porosity and low permeability, which release large quantities of water upon remoulding (Moon *et al.*, 2015b). Multiple reports have been published explaining the effects of sensitivity in soils within the Bay of Plenty region, including reports for the Pahoia Tephra located at Bramley Drive (Wyatt, 2009; Keam & Milner, 2011; Cunningham, 2012; Moon *et al.*, 2013; Moon *et al.*, 2015b; Kluger *et al.*, 2016; Mills, 2016) that define the soils' varying structure, characteristics and effect on pore water pressure as they are in an almost constant state of saturation.

For a soil to be classified as sensitive, its remoulded strength after failure must be drastically lower than its undisturbed, undrained peak strength (Selby, 1993). This is defined as the shear strength ratio, a quantified ratio of undisturbed to remoulded undrained strength at equal water contents (Moon *et al.*, 2015b), as summarised in Table 2.1.

Table 2.1: NZGS guidelines for defining the Sensitivity of Soil (New Zealand Geotechnical Society (NZGS), 2005).

Descriptive Term	Shear Strength Ratio $\frac{undisturbed}{remoulded}$
Insensitive, normal	< 2
Moderately sensitive	2 - 4
Sensitive	4 - 8
Extra sensitive	8 - 16
Quick	> 16

The greater the sensitivity ratio, the higher tendency the soil has to spread or flow from varying intensities of cyclic loading including tremors, manmade cyclic vibrations or ocean microseisms.

It is widely agreed (Gulliver & Houghton, 1980; Keam & Milner, 2011; Cunningham, 2012; Moon *et al.*, 2013; Milner & Taylor, 2014; Moon *et al.*, 2015b; Steinborn, 2015; Kluger *et al.*, 2016) that the sensitive Pahoia Tephra is the likely cause of the multiple landslide events at Bramley Drive based on combined on-site and laboratory observations including obvious seepage from the base of the tephra after each major event (Gulliver & Houghton, 1980; Keam & Milner, 2011; Milner & Taylor, 2014), high induced pore water pressures observed whilst undertaking standard and vibratory CPTu measurements, and various laboratory analysis proving the tendency for the tephra's shear strength to dramatically decrease once exposed to increased pore water pressures and cyclic stress (Gulliver & Houghton, 1980; Oliver, 1997; Wyatt, 2009; Arthurs, 2010; Moon *et al.*, 2013; Mills, 2016).

The recent paper by Kluger *et al.* (2016) indicates altered rhyolitic tephras found in the North Island of New Zealand contain abundant mushroom cap-shaped spheroidal halloysite, that govern the soils sensitivity. When these cap-shaped spheroids weak electrostatic and van der Waals interactions separate, the repulsion between the spheroid surfaces result in a high sensitivity and low remoulded shear strength. A mushroom cap-shaped spheroidal rich halloysite layer at 23 m depth within the Pahoia Tephra at the Bramley Drive site displays much higher sensitivity and lower remoulded shear stress than the rest of the volcanic deposits (Figure 2.3). This layer is identified as the likely location of failure in the 1979 event and contributed to its long run out distance.

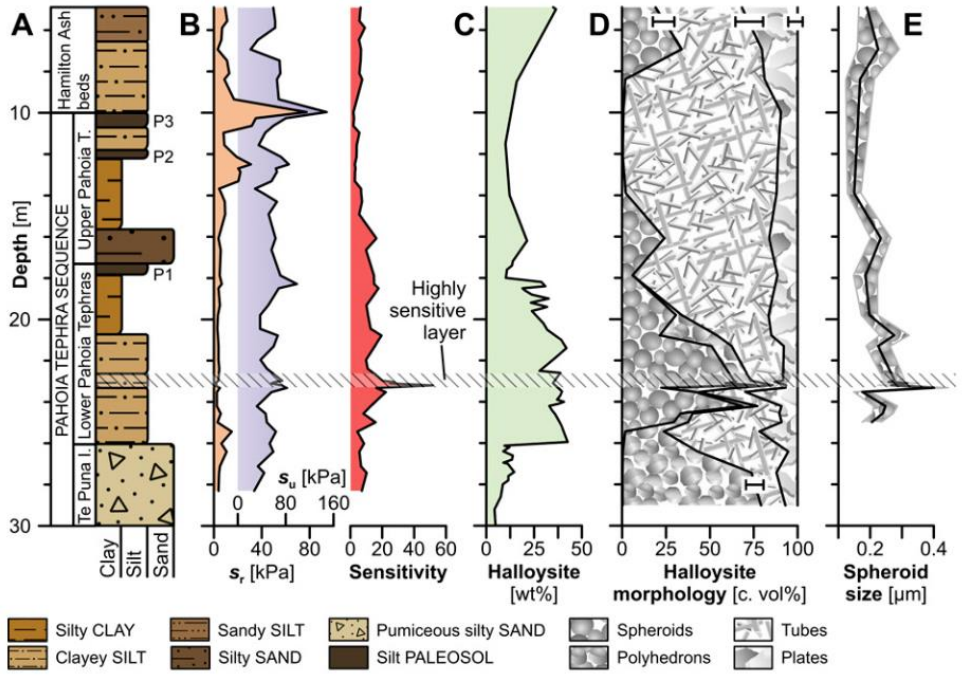

Figure 2.3: (A) Stratigraphy of the Bramley Drive site. (B) Undisturbed (blue) & remoulded (orange) shear strength and sensitivity. (C) Halloysite bulk concentration. (D) Cumulative volume percent of halloysite morphologies. (E) Average spheroid sizes. Taken from Kluger *et al.* (2016).

2.3.2 Excess rainfall and pore pressure

If the inherent structure of the Pahoia Tephra is seen as the cause of the Bramley Drive site failures, excess rainfall and the associated increase in pore water pressure can be seen as the trigger. The three investigations of the Bramley Drive Landslide by consultants (Gulliver & Houghton, 1980; Keam & Milner, 2011; Milner & Taylor, 2014) all noted prolonged rainfall immediately pre-failure, along with seepage observed from the head scarp at multiple locations post-failure, primarily at the base of the Pahoia Tephra. Semi-permanent seepage over winter months was also observed. This led to the installation of twenty-two 18 m long horizontal drains at the base of the exposed scarp in an attempt to lessen pore pressures within the sensitive tephra (Keam & Milner, 2011).

Permanent water courses are rarely observed on Omokoroa Peninsula, instead, highly permeable younger tephras deposited above the sensitive Pahoia Tephra provide a high rate of rainfall infiltration limiting the volume available for surface water runoff. This means any rainfall or other inflow of water at and/or near the Bramley Drive Landslide will predominantly percolate through the permeable volcanic soils, having the potential to rapidly raise groundwater level, along with increasing the degree of soil saturation further down (Gulliver & Houghton, 1980). This excludes water lost from evaporation or removed by road storm water catchments.

Culliver and Houghton's (1980) stability investigation pointed out some interesting correlations with cumulative rainfall and land failure in the Omokoroa region that have not been followed up to either prove or disprove their hypothesis. They suggest rainfall directly before land failure may trigger a landslide, but that the cumulative rainfall 6 months to one-year prior is the true cause of the failure, stating that if ground water level is already high due to a long period of wet weather, only a small influx of additional water could be sufficient to initiate slope failure. Using historic rainfall data from the weather station at Tauranga Airport, provided by the N.Z Meteorological Service, from 1910 to October 1979, they showed that although pre-failure July rainfall was nearly twice the average, this degree of departure was not uncommon, with return periods of various maximum rainfall durations being less than two years. Instead, the extraordinary 504 mm rainfall recorded in March 1979 was the highest monthly rainfall recorded since 1910. Based on the cumulative rainfall over 6-month intervals, the period between February and July 1979 was the wettest 6-month period recorded since 1910 with a total of 1,160 mm. Other landslides located in the Omokoroa area occurred in November-December 1962, and December 1968, both of which coincided with the sixth and tenth wettest 6-monthly totals. December 1962 also had the second highest monthly rainfall since 1910 with 447 mm.

Culliver and Houghton's (1980) investigation indicate that extraordinary rainfall over long periods (6-12 months) may influence the occurrence of land failure events, with short duration rainfall events merely triggering the event. This is a cause for concern as this could indicate average, not extraordinary rainfall events may have the ability to cause massive destruction.

2.4 MONITORING

Since September 2012, the University of Waikato and University of Bremen, Germany, have been monitoring the Bramley Drive Landslide with laser scans, borehole inclinometer, piezometer and accelerometer readings, as well as installing a weather station. Additionally, vibro- and static-CPTu measurements were undertaken behind the scarp of the landslide in February 2012. Subsequently, drill cores were obtained from two boreholes to a depth of 50 m, which were used to interpret the local stratigraphy of the area, as well as provide soil material to be later tested for in-depth laboratory work (Steinborn, 2015). The initial analysis undertaken by Moon *et al.* (2015a) of both the borehole inclinometer, three pore pressure transducers and vibro-CPTu

showed interesting and unforeseen patterns that have become the basis for this thesis and have been summarised below.

2.4.1 Borehole inclinometer

The inclinometer has been used to measure cumulative displacement over the depth of 42 m (base of casing) since early 2013. Two different inclinometers have been used: the first measurements were taken by a hired instrument as the University of Waikato did not acquire an inclinometer until May 2013, Moon *et al.* (2015a) used the first measurement in June 2013 as the baseline for assessing the deviations for subsequent observations. Cumulative plots were created from the available data; all of which showed no apparent shear surface within the inclinometer casing, instead, they showed unexpected fluctuations in both the A-axis (approximately north-south) and B-axis (approximately east-west) directions that varied seasonally. On the 22th of October 2013 a series of hourly measurements were recorded to see if the fluctuations occurred over shorter time periods, rather than the weekly to monthly intervals previously sampled. Once plotted, it was apparent the same seasonal fluctuations first noted were occurring diurnally, with movement toward the headscarp (positive) in early readings, and movement away from the headscarp (negative) in later readings. What was most interesting was that the largest magnitude fluctuations were in the B-axis, meaning some force was primarily causing the area to oscillate in an east-west direction throughout the day. This was believed to be caused by some process amplifying the effects of solid Earth tides (Moon *et al.*, 2015a).

2.4.2 Vibro-CPTu

As expected, once the static-CPTu reached the sensitive, low permeability Pahoia Tephras, pore water pressure began to quickly rise. However, what was more significant was that there was a dramatic increase in pore water pressures between 17-20 m in the vibro-CPTu run that showed induced pore water pressures up to 3 times higher than that of the static-CPTu run, suggesting a potential response to cyclic stresses in the material, which could contribute to a reduction in soil strength (Moon *et al.*, 2015a).

2.4.3 Piezometers

Since May 2013, three pore pressure transducers at depths of 12, 21 and 27.5 m have been logging changes in pressure. Moon *et al.* (2015a) observed that the 12 m piezometer responds directly with air pressure, while the 21 m piezometer shows a

similar but damped response to air pressure and the lowest 27.5 m piezometer shows no correlation with air pressure. It was hypothesised that there are two discrete aquifers, one in the Pahoia Tephras that is open to the atmosphere, and one within the Te Puna ignimbrite that responds independently (Moon *et al.*, 2015a). Notably, intense rainfall events show a temporary increase in pore pressure in both the 12 and 21 m piezometers, confirming that within the low permeability Pahoia Tephras pore pressure are strongly influenced by large episodic rainfall events.

2.5 CAUSES OF DIURNAL GROUND MOVEMENTS

The daily fluctuations observed in the borehole inclinometer (Moon *et al.*, 2015a), along with the local volcanic tephras response to induced cyclic stresses (Mills, 2016) means it is of great importance to understand and unravel the causes of the observed ground deformations in order to identify factors that may contribute to slope failure. There are a mixture of cyclic and non-cyclic potential factors that may contribute to slope failure, which are expanded upon below. Each of these factors potentially contribute different proportions to the total displacement.

2.5.1 Cyclic processes

Cyclic loading refers to a rhythmic system of loading that exhibits a fairly regular magnitude and frequency (O'Reilly & Brown, 1991). Engineered structures must take into account these phenomena as they are highly dependent on the structures resonance frequency and regularity of applied loading. In soil, cyclic loading may occur any time the soil is in a non-static state. The cyclic loading behaviour in soil is largely dependent on strain rate, stress reversals and drainage patterns (release of pore water pressures), while the regularity of the loading in many cases is of little concern (O'Reilly & Brown, 1991).

Numerous processes can cause cyclic loading within a rock or soil structure; many being a daily occurrence. Predictable diurnal and semi-diurnal movements of the Moon and Sun, and changes in ocean tidal loading exert relatively frequent increases and decreases of stress, while non-cyclic factors such as rainfall and wind periodically occur, usually increasing stress or lowering shear strength to a higher degree than daily expected stress reversals. Unpredictable events like earthquakes and man-made vibrations from machines or vehicles are examples of abrupt changes in soil or rock from a relatively static state to a dynamic state, causing effects like mass failure, liquefaction, lateral spreading or settlement.

2.5.1.1 Wave induced pressure variations and microseisms

Ocean waves transfer energy, and are provided by multiple sources including wind, atmospheric pressure, and gravity. These waves come in many different sizes and frequencies depending on the processes forming them; the most prominent being the gravitational attraction of the Moon and (to a lesser extent) the Sun which forms ordinary tidal waves, and wind that forms ordinary gravity waves (Johnson & Council on Wave Research, 1951). Figure 2.4 shows the classification of ocean waves according to wave period, beginning with capillary waves with a period of less than 0.1 seconds. These capillary waves are more affected by surface tension than by gravity, while also being responsible for the apparent roughness of the surface, determining the effectiveness of the wind dragging over the surface of the water. A detailed history and review of capillary waves was provided by Longuet-Higgins (1963).

Ultra-gravity waves and ordinary gravity waves owe their existence to the wind (Johnson & Council on Wave Research, 1951) as they are a result of the winds within distant weather systems blowing over a fetch of water. These "wind waves" are inherently random, with waves varying in height, duration and shape, but they are primarily between periods of 3-10 seconds and are the most commonly observed waves reaching the coastline, either as swell or breaking waves (surf), before reflecting and returning to the ocean. The characteristics of these waves greatly change depending on both the local and distant weather, with storms usually both raising wave period and amplitude. The interaction of gravity waves with the shore can generate small seismic waves within the ground, which are called microseisms. Residents that live on coastal cliffs sometimes report ground shaking due to storm waves; however this has not been well quantified (Young *et al.*, 2011).

Infragravity waves are similar to previous ultra-gravity and ordinary gravity waves in that they are partially formed by wind, as well as being related to the variability in the shorter period waves (Johnson & Council on Wave Research, 1951). They typically occur at periods between 30-300 seconds and can modulate breaking wave (surf) characteristics, resulting in a series of alternating high or low breakers, which in turn increase or decrease relative water level (Young *et al.*, 2011). This regular occurrence within the nearshore is known informally as "surf beat" due to its almost heartbeat-like pulsation. Together, a proportion of the energy of these waves is transferred to the solid Earth, and although small, can be recorded by seismometers.

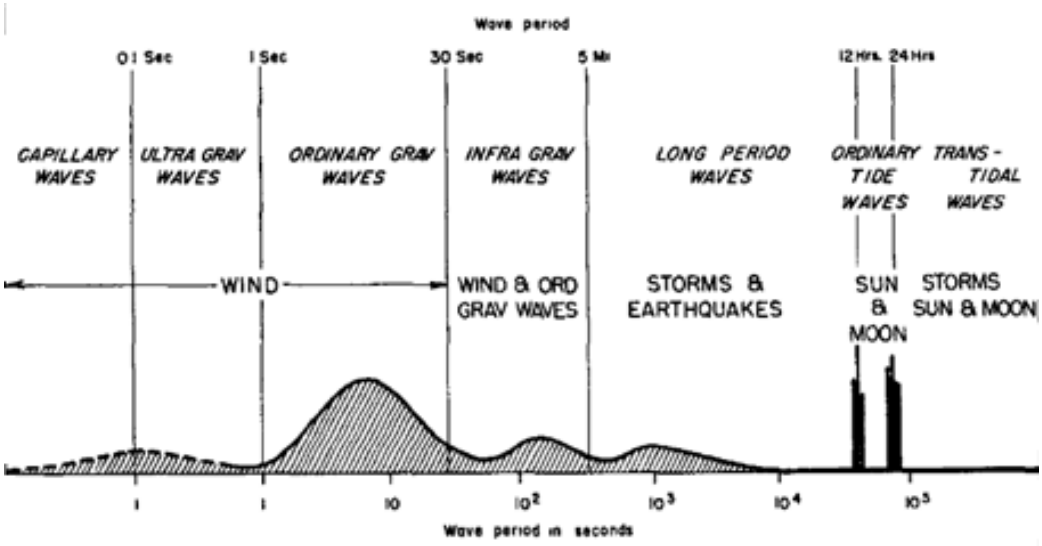

Figure 2.4: Classification of ocean waves according to wave period. Relative amplitude is displayed by the curve (Johnson & Council on Wave Research, 1951).

These faint Earth tremors, or "microseisms" describe the continuous oscillations of the ground and have been researched to assess their impacts on rock stability (Adams *et al.*, 2005; Young *et al.*, 2011; Young *et al.*, 2012; Brain *et al.*, 2014).

Ocean derived tremors, unrelated to earthquakes and local anthropogenic sources, can be classified as either primary or secondary microseisms and are interpreted as short-period P waves. Haubrich *et al.* (1963) first identified these two distinctive frequency bands and they are investigated in-depth in both his original paper as well by Cessaro (1994), which covers the sources of these two types of microseisms.

Primary microseisms have periods ranging between 13-300 seconds and are formed by the direct conversion of ocean wave energy at the sea floor to seismic energy, hence, they have periods that match those of the incoming ocean waves (Haubrich *et al.*, 1963).

Secondary microseisms are generated by the interaction of incident waves with those reflected back off the coast, which forms a standing wave with half the period, or twice the frequency, as the original ocean waves (Kedar *et al.*, 2008). This second-order pressure term effect does not dissipate with depth and can travel large distances, being recorded as background noise in seismometers 100's or even 1000's of kilometres away from the ocean (Ardhuin *et al.*, 2011).

As two identical wave trains meet they create a pressure oscillation (Equation 1) at the sea floor that is a function of mean pressure P at the seafloor and P_0 at the surface (Bhatt, 2014).

$$\frac{P-P_0}{\rho} - gh = -2a_1a_2\omega^2\cos(2\omega t) \qquad \text{(Equation 1)}$$

ρ = fluid density
h = water depth
a_1 & a_2 = amplitudes of each wave
ω = angular frequency ($2\pi f$)
g = gravity (9.81 ms-1)
t = time

From Equation 1 it is evident that if either a_1 or a_2 become zero the pressure oscillation will vanish, demonstrating a single wave cannot create a pressure disturbance on the seafloor (Bhatt, 2014).

Adams *et al.* (2005) hypothesised that while microseisms are largely unrecognised as a geomorphic process, they may in fact be significant, and suggests that observed ground motions within exposed sea cliffs are comparable to being bombarded by a geomorphic wrecking ball every 4-25 seconds.

Considering the effects of microseisms on rock stability, Brain *et al.* (2014) suggest that micro-seismic ground displacements caused by ocean wave derived microseisms may contribute to the weakening of rock discontinuities. However, it is recognised that multiple processes can affect subcritical crack growth and rock weakening. It is also hypothesised that any significant damage by microseisms is episodic (such as storms), while solely tidally-controlled displacements are ineffective. It was appreciated that other storm related episodic damaging processes would likely also contribute to failure, including pore water pressures (Brooks *et al.*, 2012) and ocean wave impact and loading at the base of the cliff (Salih Kirkgöz, 1990).

No published studies could be found that have assessed the effects of microseisms on cohesive sediment coastal bluffs like at Omokoroa Peninsula; so only broad, generalised correlations between a hard rock cliff and the impacts of microseisms possibly acting on the Bramley Drive Landslide can be made. These include the possibility that episodic effects may affect observed magnitudes of microseisms (if any) and that they are unlikely to be a sole cause of slope failure due to the additional processes accompanying storm events such as rainfall, increased pore water pressure, wave impact and wind speed.

2.5.1.2 Solid Earth tides and ocean loading

Just as the oceans are affected by the gravitational pull of the Moon and Sun resulting in tidal waves, the Earth's lithosphere is distorted by the strain these celestial bodies exert. This was first considered by William Thompson (1824-1907), who developed the first theory of the Earth as an elastic solid, with one of his students George Darwin (1845-1912; a son of Charles Darwin) applying Thompson's theory by comparing tidal amplitudes at multiple locations on an elastic Earth to that on a rigid Earth. With this simple comparison being significantly smaller than 1, Darwin proved that Earth tides existed (Ekman, 1993).

With this discovery, Darwin also attempted to predict the existence of loading tides by calculating the effect of ocean loading by ocean tidal waves on an elastic crust. This additional force also deforms the elastic Earth, and Figure 2.5 illustrates the distortion of the Earth's surface in response to ocean loading. It indicates that the effect, while strongest in coastal areas, can also affect land far away from the ocean.

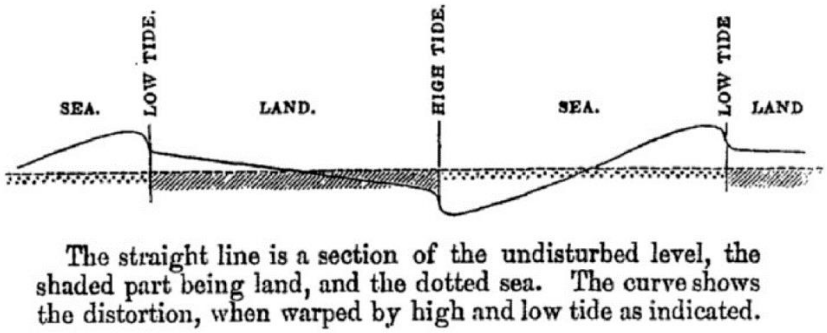

Figure 2.5: Ocean loading tides illustrated by Darwin (1882), from Ekman (1993).

Further study into Earth tides over that past century, summarised by Ekman (1993) has led to well established models for Earth tide and ocean load prediction worldwide, and will be further explained in Section 4.3

2.5.1.3 Generalised Earth tide propagation

The Moon accounts for most of the gravitational force, while the Sun accounts for the rest (Agnew, 2015). This in turn creates semi-diurnal ground movements within the Earth as the Moon orbits at a slight angle to Earth's equator. At high tide the Moon is either at its closest location to that part of the Earth, thus imposing its greatest gravitational attraction towards Earth, or the Moon is on the opposite side of Earth, where the gravitational attraction towards the Earth is at its weakest. The changes in

gravitational attraction, combined with the centrifugal force of the Earth's orbit around the lunar orbital axis, cause a bulge in the Earth's surface (McCully, 2006).

Each semi diurnal cycle is approximately 12 hours 25 minutes in length, which is approximately half of one lunar day (Darwin, 1989). Using this knowledge, a 6-hour interval will account for the mean greatest rise or fall in vertical amplitude at a point. As the Earth's orbit is tilted, this gravitational effect will cause an elliptical movement of the ground as the Moon rises from the east and sets in the west (similar to the Sun), whilst also slightly moving latitudinally across the Earth (declination of the lunar orbit) (McCully, 2006).

Other factors that affect the amplitude of solid Earth tides are the distance from Earth to the Moon, and the Moon's velocity. The Moon follows an elliptical orbit, meaning the strength of the lunar gravitation is not always the same due to the change in distance from Earth. When the Moon is at its closest it is called the perigee, and when the Moon is at its farthest point from Earth it is called apogee. The Moon is approximately 50 000 km closer to the Earth at perigee, however this elliptical orbit is constantly changing in rhythmic cycles like all other celestial bodies. Its velocity also changes due to the elliptical orbit, as the Moon orbits towards the Earth it gains momentum due to the increase in Earth's gravitational attraction to the Moon. As the Moon orbits away from the Earth it begins to decelerate due to the same gravitational force trying to pull the Moon back towards Earth (McCully, 2006).

As the Sun is also responsible for some gravitational attraction towards Earth, times where both the Moon and Sun are aligned with Earth (spring tides), the solid Earth tides in theory should be at their greatest amplitudes, with the highest high tide, and lowest low tide throughout the cycle. As the Earth follows an elliptical orbit as well, the Earth's distance to the Sun has much the same effect as the Moon's distance to Earth, changing over the annual cycle, increasing the amplitude of the tides due to the Earth's distance and velocity (McCully, 2006). Further explanation of Earth tides and their ability to deform the Earth to varying degrees can be found in Section 4.3.

As with microseisms, solid Earth tides are usually seen as a source of noise in most seismic observations (Poulsen, 2009), with magnitudes so low that instruments such as the inclinometer used at the Bramley Drive site cannot usually detect them due to the inadequate sensitivity of the equipment.

2.5.1.4 Generalised Ocean Tide Loading Propagation

Fluctuations in the ocean tide have the potential to cause varying degrees of deformation of the solid Earth due to the increase and decrease in water mass (Figure 2.6). This periodic loading and unloading of the ocean tides has both a vertical and horizontal component at the surface, subjecting coastal areas such as shore platforms and cliffs to semi-diurnal stresses that can in theory cause cyclic loading within the soil or rock due to near constant amplitudes and frequencies (Rafiq & Santos, 2004).

Unlike Earth tides, water mass movement (ocean tides) and ocean loading both have tidal periods, however neither are necessarily in phase with Earth tides due to coastal topography and frictional lag (Jentzsch, 1997). Coasts that are exposed to larger high and low tide amplitudes or locations with only diurnal tides will exert a larger ocean tide load to the surrounding land due to the increased or prolonged duration of the applied water mass. To summarise, ocean loading during a rising tide causes the surrounding land to move in a negative direction vertically due to the increased water mass at high tide, then unloading with a falling tide effectively lets the elastic Earth relax and move in a positive vertical direction as water mass decreases. Tidal phases such as spring and neap tides all affect the effect of ocean loading at a chosen location (Goring & Walters, 2002).

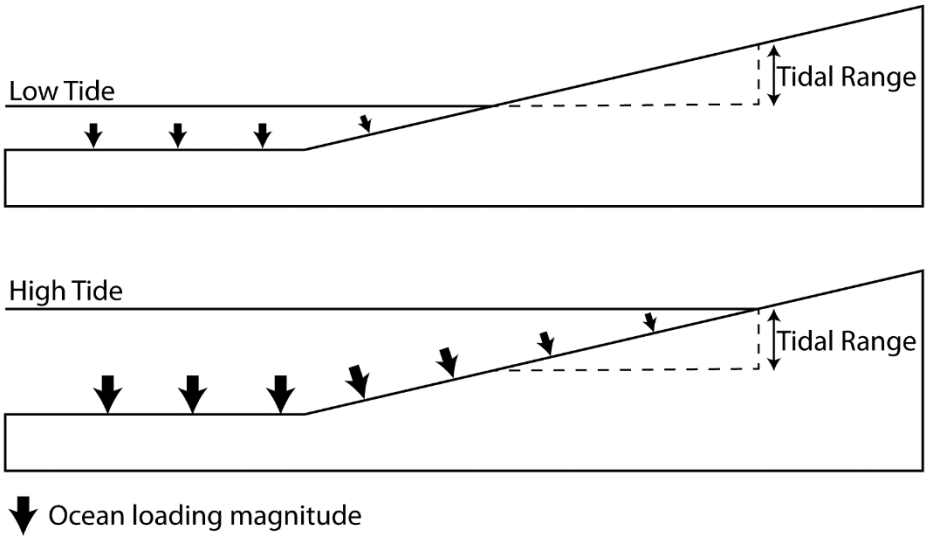

Figure 2.6: Generalized mechanism of ocean tide loading.

2.5.1.5 Soil Temperature

The increase and decrease in soil temperature throughout any given day has the potential to contract and expand the exposed surface by the removal of moisture, which can affect vertical oscillation. This is most apparent in soils with a moderate to

high concentration of shrink-swell clay minerals, which are predisposed to significant increases and decreases in volume in response to temperature changes, due to their ability to release liquid during hot dry conditions, while being able to reabsorb liquid when moistened (Fernandes *et al.*, 2015).

While the ability of a certain soil to expand and contract due to moisture content is likely the most apparent when looking at vertical displacement, thermal properties including the storage and movement of heat in soils may also be an important factor for volume change in soils (Abu-Hamdeh, 2003). This possible thermal expansion could be highly seasonal as the temperature and heat flux in a soil is extremely dependent on its moisture content.

At its most basic, an example would be the temperature of sand at the surface on a beach. In colder and wetter months that are prevalent in winter and spring, surface temperature is similar to air temperature, whereas, in warmer and drier months during summer and autumn the surface sand temperature can far exceed air temperature, making it unbearable to walk across at times. The heating of beach sand is primarily by solar radiation (insolation); however, the thermal properties, and the proportions of available pore space that can be filled with either air or water in the sand also plays a role (Abu-Hamdeh, 2003; Romagnoli *et al.*, 2003; Lal & Shukla, 2004). This explains why wet sand at the beach during summer has a distinctly lower temperature than nearby dry sand.

The reason why air warms faster than water is due to its much lower heat capacity (1.01 J/g ºC, dependent on the amount of water vapour present), compared to water (4.18 J/g ºC). This means that the amount of specific heat required to raise 1 gram of water by one degree is approximately 4 times higher than 1 gram of air. This also means it is easier for air to lose heat energy (cool), so hot and dry periods where the moisture content of the soil is low will have much warmer soil temperature in the days and much cooler (relative) soil temperatures at night, returning a much higher change in diurnal temperature compared to the same soil with a higher moisture content.

Changes in temperature also have the potential to create chemical reactions within soil depending on the mineralogy (Gislason & Oelkers, 2003). While it is assumed that there is a chemical reaction effect caused by temperature within certain types of soils, literature is sparse and it is a subject requiring further investigation.

2.5.1.6 Insolation

Much of the absorbed energy that varies temperature on Earth is derived from radiation from the Sun. Approximately 31% of this energy is scattered or reflected by cloud cover, aerosols and Earth's surface (Houghton, 1996), with the rest warming the Earth's surface and atmosphere (Figure 2.7). Once solar radiation hits the surface, the surface temperature begins to increase, and depending on the surface composition (water, soil, concreate, forest) it will heat at different rates due to varying heat capacities and different reflectivity.

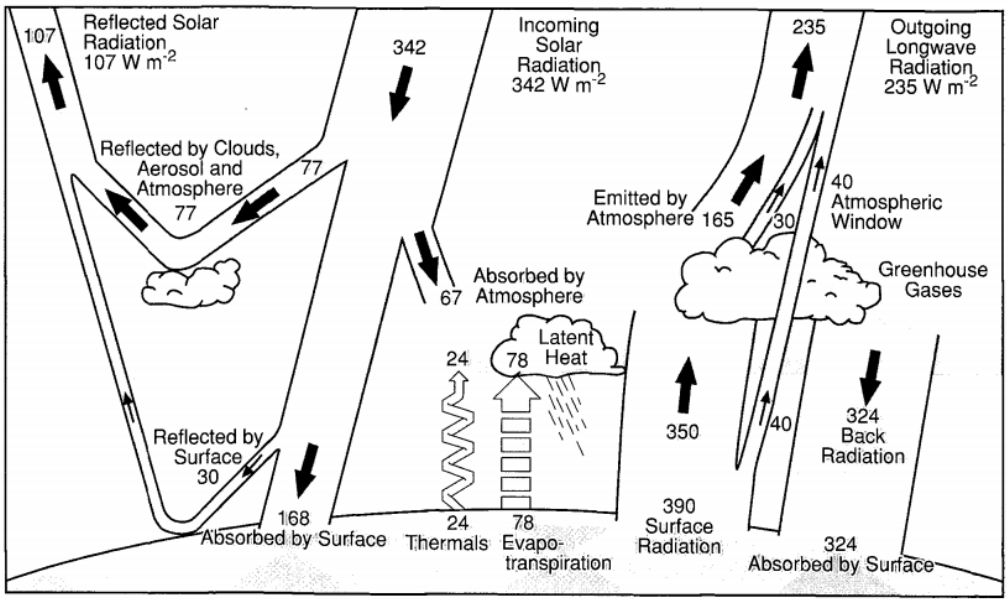

Figure 2.7: The mean, annual Earth's radiation and energy balance, with net incoming solar radiation of 342 W m^{-2}. Reflection, and absorption by multiple factors are shown (Houghton, 1996). This energy budget is formed using data from (Kiehl & Trenberth, 1997).

Due to the spherical shape of Earth, half the Earth is exposed to solar radiation at any time while the other half of the Earth is obscured from the Sun. At its most basic, this means surface temperature increases in the day as the incoming energy from the Sun exceeds energy losses, while at night, no solar radiation is there to offset surface energy loss. This is associated with diurnal temperature fluctuations.

Each hemisphere also experiences both a winter and summer season due to the tilt of the Earth's rotation (Figure 2.8), with the Sun's radiation increasing and decreasing relatively (Pidwirny, 2006). This change is not caused by fluctuations in solar radiation intensity (although intensity does slightly fluctuate annually due to the elliptical orbit of Earth), but rather the total daylight hours an area will be subjected to, and at what angle incoming solar radiation hits the surface.

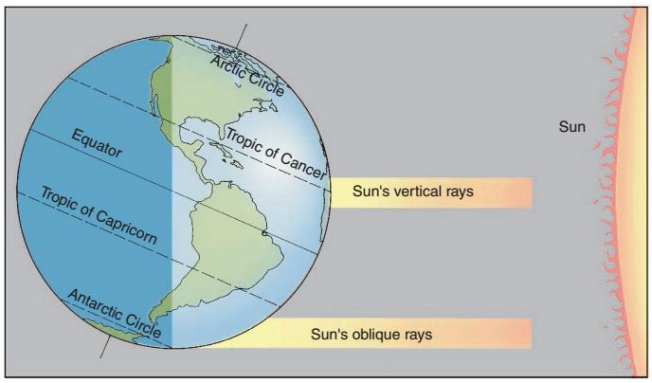

Figure 2.8: Diagram representing winter conditions in the southern hemisphere, when solar radiation strikes perpendicular on the Tropic of Cancer (Pidwirny, 2006).

Figure 2.9 shows how steeper angled Sun rays that occur in summer are more concentrated than low angled Sun rays that spread out (Pidwirny, 2006). While incoming solar radiation is the same in both the summer and winter months, the steeper incidence angle of solar radiation occurring in the summer months provides a higher incoming energy to the atmosphere and surface of the earth. This leads to a higher surface temperature in the summer; whereas, in the winter months the lower incidence angle of solar radiation provides less incoming energy, and thus, a lower surface temperature.

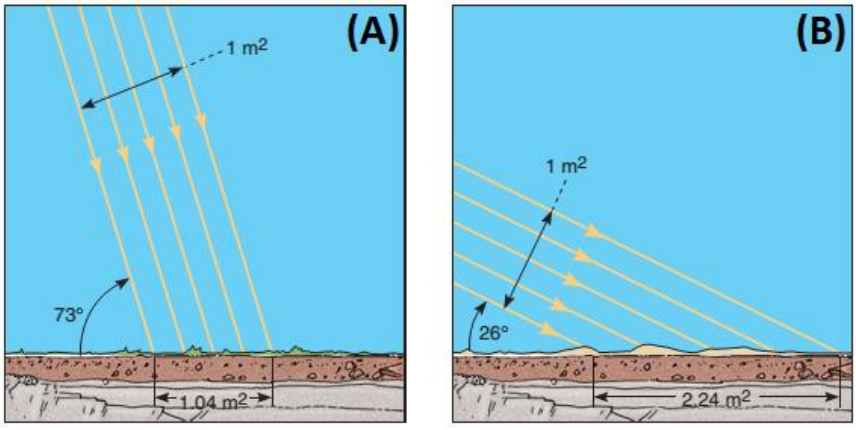

Figure 2.9: (A) Generalized relationship of Sun's rays in summer and (B) Sun's rays in winter (Pidwirny, 2006).

Cloud cover and the location of the Earth's surface also play a minor role, decreasing the amount of direct sunlight and solar radiation to the affected surface. At the Bramley Drive Landslide, due to its north-westward orientation of the headscarp, early morning solar radiation from the east is unable to directly hit the surface until the Sun is high enough in the sky. Also due to the landslide's size and shape, some areas of the slope are subject to prolonged exposure of direct sunlight and greater amounts of solar

radiation compared to other areas on the same slope. This may induce different responses in different parts of the slope.

2.5.1.7 Atmospheric tides

Although deemed very minor, the atmosphere can affect the surface of the Earth as the barometric weight either increases or decreases (McCully, 2006). Atmospheric highs are associated with an increase in barometric pressure which leads to an increase in the gravitational force exerted on the surface, while atmospheric lows decrease gravitational force. This is more apparent in oceans where a small increase or decrease in barometric pressure will cause the ocean to rise or fall by a few centimetres to over a meter (McCully, 2006).

Schulz *et al.* (2009), suggested that atmospheric tides were deemed responsible for daily ground movements at the Slumgullion Landslide located in south-western Colorado, USA. This landslide is classified as a translational slide, failing along boundary faults. It is 3.9 km long and averages approximately 300m wide. Results showed that daily ground movement was primarily observed during diurnal low atmospheric tides, which cause air and water to flow vertically, causing changes in soil shear strength. They also suggested that rapid changes in barometric pressure during fast moving storm events could trigger a similar response.

2.5.2 Non-cyclic processes

Non-cyclic or episodic processes also play a large role in the stability of slopes and cliffs. These processes, although not a daily and predictable occurrence, can impart great dynamic strain on the surrounding soil increasing the risk of slope failure. These events make different contributions to slope failures, rainfall and wind which are predominantly caused by episodic storm activity, are considered the most important events.

2.5.2.1 Rainfall

Rainfall has been identified as a major contributing factor to slope instability, particularly for triggering failure at the Omokoroa Peninsula and within the wider Bay of Plenty region. Intense periods of rainfall saturate the volcanic soils present, increasing pore water pressure while also increasing total weight of the soil. This saturation of the sensitive soil also causes halloysite clay minerals to break apart and separate almost instantaneously due the increased pore pressure (Kluger *et al.*, 2016) while greatly decreasing its total shear strength, triggering ground movement as the

excess fluid attempts to escape laterally out of the exposed surface of the slope (Gulliver & Houghton, 1980; Oliver, 1997; Keam & Milner, 2011; Cunningham, 2012; Moon *et al.*, 2013; Milner & Taylor, 2014; Moon *et al.*, 2015a; Steinborn, 2015).

Rainfall and its triggering effect on landslides can be separated into two separate events: rainfall occurring in a period before the failure event (antecedent rainfall), and rainfall on the day of the event (Glade *et al.*, 2000). Crozier and Eyles (1980) first introduced the "antecedent daily rainfall model" (Equation 2), which is calculated by a combination of these two types of events, as an empirical predictor for regional landslide-triggering thresholds within New Zealand.

$$ra_0 = kr_1 + k_2 dr_2 + k_3 dr_3 + \cdots + k_n\, dr_n \qquad \text{(Equation 2)}$$

ra_0 = antecedent daily maximum precipitation (mm)
r_n = maximum regional precipitation (mm) on the nth day before 0
k = constant representing the outflow of the regolith (0.84, refer Bruce & Clark, 1966)
d=hydrographic recession curve coefficient d (refer Glade et al., 2000)
n = number of days before the day 0 (n= 10 days, refer Glade, 1997)

Although this method was not applied within the Bay of Plenty, instead using stream flow data from Ottawa, USA and an antecedent period of 10 days (Glade, 1997), Crozier and Eyles (1980) suggested the Antecedent Daily Rainfall Model may be useful throughout New Zealand with further study (Glade *et al.*, 2000). This model shows that there is a definite relationship between rainfall and landslide triggering.

To relate this to the sensitive soils observed at the Bramley Drive Landslide in Omokoroa, a minor but prolonged rainfall event that would saturate the soil initially, with a heavy rainfall over one day triggering failure has previously been suggested as an important factor (Gulliver & Houghton, 1980).

2.5.2.2 Wind

The vibrational effect of strong winds on vegetation in a sloped environment has been hypothesised as contributing to slope failure. It is assumed non-cyclic storm events providing high winds could potentially cause localised cyclic loading within the soils that host the vegetation's root systems. However, published studies of this effect are minimal, which makes it difficult to assess the importance of this factor. For large trees the wind effect at storm force wind speeds of 90 km/hr (25 m/s or ~50 knots) was found to add < 1 kPa to shearing stresses to the soil (Hsi & Nath, 1970).

With regard to slope stability however, it is agreed that vegetation has the ability to increase soil shear strength by mechanical reinforcement of the soil by root networks, provided the added surcharge caused by the vegetation's weight does not affect the slopes stability (Selby, 1993).

2.6 SUMMARY

As with many coastal cliffs in the Bay of Plenty, the Bramley Drive Landslide is inherently unstable and unless a viable option of remediation is found it is likely to fail again in the future. Investigations by multiple researchers have concluded that sensitive soils within the Pahoia Tephra are responsible for the failures due to their ability to fail catastrophically under cyclic loading and increased pore water pressure. Ongoing recording of the onsite borehole inclinometer shows that diurnal effects are somehow amplifying ground displacement within the borehole presumed to be from solid Earth tides, thus multiple cyclic and non-cyclic processes were reviewed.

Considering the location of the Omokoroa Peninsula and its distinct lack of large vegetation due to remediation works over the years, the effect of the wind on ground deformation will not be investigated in this thesis. The investigation of atmospheric tides will also be excluded from this thesis due to the lack of a barometer on site(Schulz *et al.*, 2009). The only paper proposing that landslides may be triggered by atmospheric tides refers to a presently moving, slow translational slide covering an area of 1.2 km^2, and shows no similarities to the geology, morphology or failure history with the Omokoroa Peninsula.

Microseisms, Earth tides, insolation, rainfall and temperature seem to be the most relevant in regards to diurnal ground displacement on site and will be investigated in this thesis.

CHAPTER 3

RESEARCH METHODOLOGY AND OBSERVATIONS

3.1 INTRODUCTION

Using instruments previously installed on-site, this chapter provides an unbiased or un-interpreted observation of recorded data obtained by a weather station an accelerometer that records averaged 10-minute data, and a borehole inclinometer that is measured periodically throughout the year. These combined data will be displayed, noting obvious trends in regards to daily, seasonal and yearly observations.

The instrument locations on site are shown in Figure 3.1 and Figure 3.2.

Figure 3.1: Photo viewing south. viewing Bramley Drive site and instrument location (circled) in regards to landslide head scarp– photo courtesy of W.de. Lange.

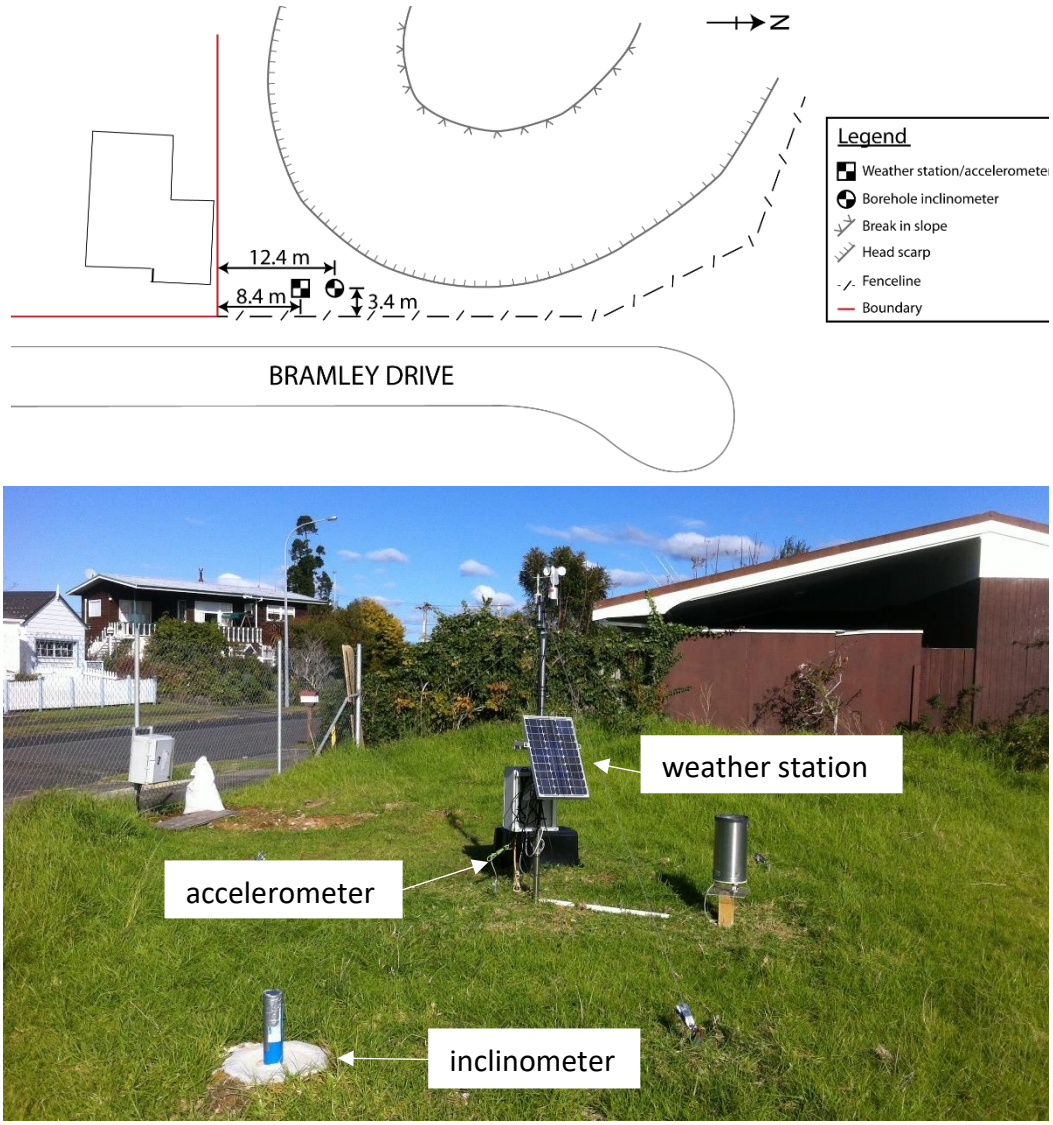

Figure 3.2: Site plan, including instrument location and approximate head scarp location at present (above), Photo viewing southeast. showing inclinometer and weather station (below) – photo courtesy of W.de. Lange.

3.2 FIELD INSTRUMENTS AND INSTALLATION

3.2.1 Inclinometer

Since June 2013 borehole inclinometer measurements have been recorded at weekly to monthly intervals using a Digitilt inclinometer probe in conjunction with the Digitilt DataMate II data logger from Slope Indicator™. The borehole location is approximately 5 m behind the central area of the Bramley Drive Landslide head scarp (Figure 3.2), and extends to a total depth of 43 m below the ground surface. Its location was chosen as being the area most likely to fail in the future given the trend of previous regressive failures over time, while also being close to the center of the slide so that any movement may be representative of the entire failure area. The borehole's A-axis guide grooves were aligned at 320 °T, perpendicular to the most recent regression scarp, so that the A-axis will predominantly measure movement in

the direction of the slope face (*ca.* N-S component), while the B-axis will measure movement parallel to the slope face (*ca.* E-W component) (Figure 3.3).

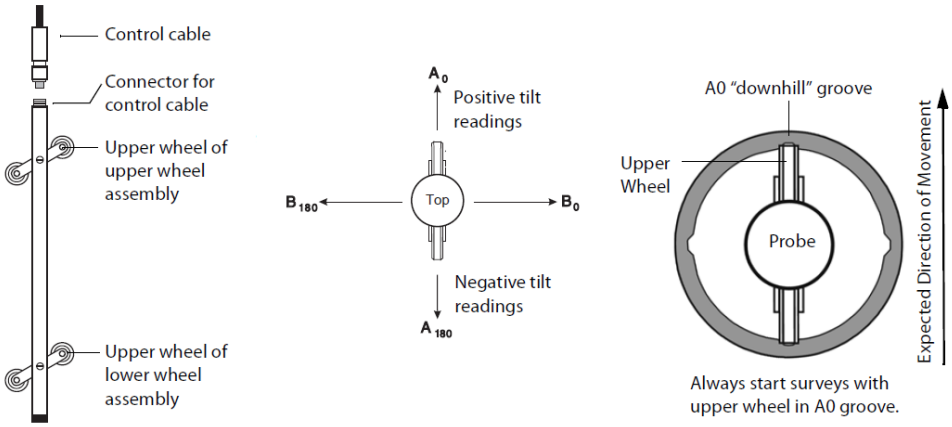

Figure 3.3: Schematics of the inclinometer probe, axes direction and installation instructions. Note borehole inclinometer is orientated in the A0-A180 direction (perpendicular to head scarp), with the B0-B180 direction being calculated after measurements are taken (Digitilt Inclinometer Probe user manual).

At its most basic, tilt measurements recorded by the inclinometer are used to calculate the side opposite of angle θ from the vertical (Figure 3.4). This is calculated using simple trigonometry as both the angle and hypotenuse (measurement interval) is known. For this study a measurement interval of 0.5 m was used, which corresponds to the separation of the wheel assemblies (Figure 3.3). Figure 3.4 shows how a simple understanding of trigonometry allows calculation of the borehole displacement, as both the interval deviation at the recording depth, and cumulative deviation over the whole borehole. To minimise any instrument bias error and preserve the direction of tilt, two measurements for the A-axis were taken during each recording, firstly when the probe is orientated in the "A0" direction, and the second in the "A180" direction, where the probe is rotated 180° before taking the second set of measurements.

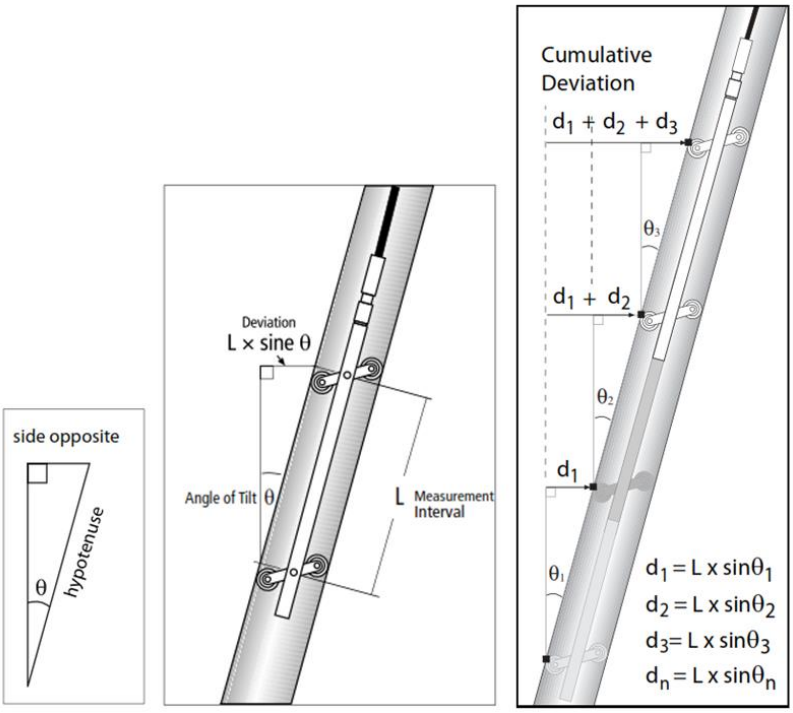

Figure 3.4: Schematic of how the borehole inclinometer measure tilt from the vertical which give the opportunity to calculate lateral movement using trigonometry to calculate borehole deviation (Digitilt Inclinometer Probe user manual).

3.2.2 Accelerometer

An AC-43 Force Balance Accelerometer from GeoSIG™ was installed (Figure 3.5) on the 24th of June 2014 and has since been recording average acceleration in X, Y and Z directions over 10 minute intervals, which returns the acceleration in each direction. Placement was orientated as close to true north as possible, meaning the accelerometer was installed approximately 20° offset from magnetic north. This ensures X measures north-south acceleration, Y measures east-west acceleration and Z measures vertical acceleration.

Figure 3.5: Installed accelerometer showing placement (above) and orientation (below) – photo courtesy of Dr W.de. Lange.

This triaxial accelerometer was designed for urban and industrial applications, including earthquake surveys and vibration monitoring. For this study cyclic vibrations/patterns were investigated at different time periods in an attempt to define and separate cyclic causes contributing to ground accelerations.

One-second data were also recorded from August 2015 to July 2016, and was used to find factors that are less than 10 minutes, such as wind waves (1-30 s) and infragravity waves (30-300 s) (Figure 2.4 and Table 3.1.)

Table 3.1: Classification of ocean waves and their respective wave periods (Johnson & Council on Wave Research, 1951).

Classification	Period
Capillary waves	>0.1 sec.
Ultra-gravity waves	0.1 – 1 sec.
Ordinary gravity waves	1 – 30 sec.
Infragravity waves	30 sec. - 5 min.
Long-period waves	5 min – 12 hours
Ordinary tides	12 – 24 hours
Trans-tidal waves	>24 hours

3.2.3 Weather Station

A weather station was installed on the 24th of June 2014 next to the accelerometer to record rainfall, wind direction and speed, internal temperature and battery volts in 10 minute intervals (Figure 3.2). Additional sensors including air temperature, soil temperature (5cm deep) and solar irradiance were installed on the 14th of May 2015.

3.3 INCLINOMETER OBSERVATIONS

As the inclinometer data has been collected intermittently, trends in diurnal displacement will be difficult to quantify as only a few daily recordings have been collected since July 2013. Two different inclinometer instruments have been used to obtain the data. The initial data were obtained by a Digitilt inclinometer hired from Geotechnics Ltd between the 13th of March 2013 and the 2nd of July 2013. The University of Waikato purchased the system described above, and started using it on the 26th of June 2013. Measurements were made with both inclinometers on the 2nd of July 2013, to allow for calibration of the earlier data. Since then only the University of Waikato system has been used.

This study will only use the data obtained by the University of Waikato system, as it was subsequently determined that an unknown component of the different borehole profiles recorded by the two systems may be due to the deformation of the borehole during and between the measurements. Recordings have been collected primarily by Dr Willem de Lange, as well as various students and staff, who all follow the same written instructions on how to setup and use the same borehole inclinometer. Therefore, it is assumed all data (excluding highly irregular recordings that will not be used) is consistent.

3.3.1 Observations at different time periods

This section of the report will identify changes in the borehole profile and when these changes occurred.

3.3.1.1 Borehole profile change since July 2013

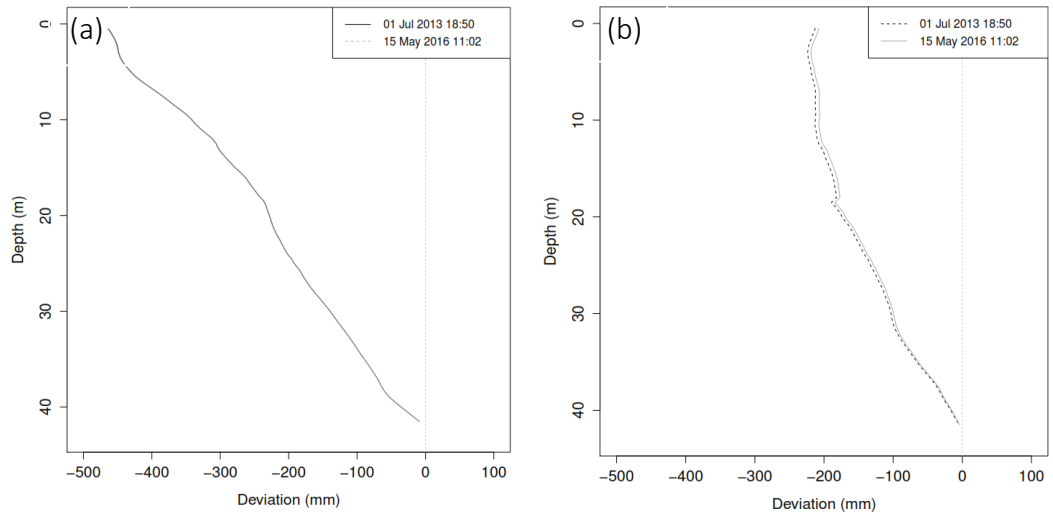

Figure 3.6: Borehole profile change from July 2013 to May 2016 in the (a) A-axis and (b) B-axis.

By calculating the inclinometer's tilt at defined depths, cumulative displacement can be calculated that reveals the borehole's shape, total depth and direction. Figure 3.6 shows that the borehole is not exactly vertical, but is slightly askew, moving north-west from the borehole starting location (closer to the face of the slope). As the borehole is 43 m deep, a slight trend of less than 0.5 m from the vertical over the length of the borehole is not uncommon for standard drilling practices and amounts to less than 1° deviation from vertical.

After four years, almost no change in the borehole profile has been observed (Figure 3.6). With regards to slope stability this is a good outcome for local residents, as the primary use of a borehole inclinometer is to show sharp horizontal discontinuities within a borehole that define shear boundaries. To show just how little change has occurred, additional plots showing a zoomed in view of the start of the borehole show that after almost four years less than 1 mm northwards displacement in the A-axis, and a maximum of 5 mm westwards displacement in the B-axis is observed (Figure 3.7).

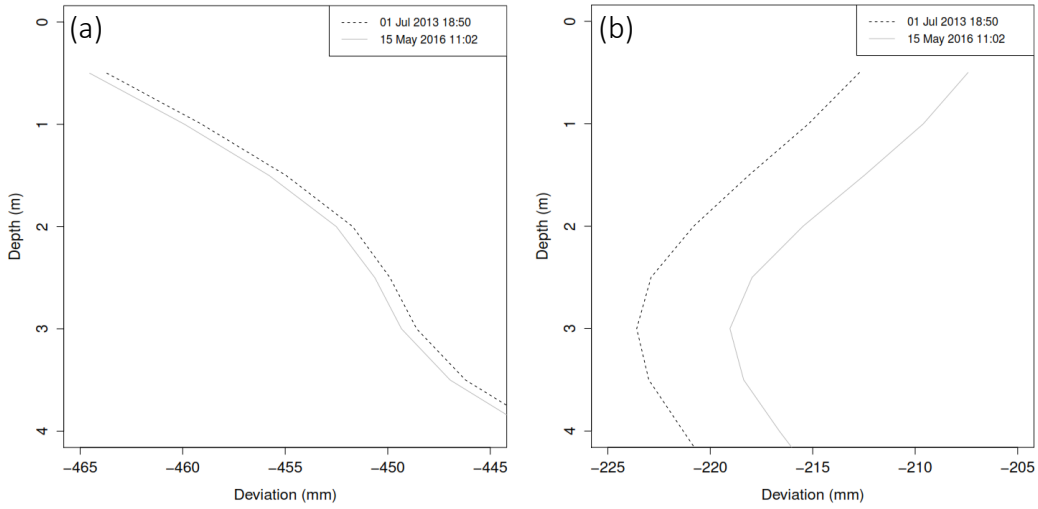

Figure 3.7: Zoomed in view of borehole profile change from July 2013 to May 2016 in the (a) A-axis and (b) B-axis.

Although the overall shape of the borehole has not changed very much over four years, significant changes between surveys were measurable.

3.3.1.2 Cumulative displacement since installation

Using the first inclinometer test recorded at 18:50 on the 1st of July 2013 as the baseline profile, 48 recordings were superimposed to show the large deviations in the borehole since its installation (Figure 3.8). Now instead of observing minimal total displacement between two tests almost four years apart, fluctuations of approximately ±2 mm in the A-axis and ±10 mm in the B-axis between surveys are clearly shown. These exceed the expected error of ±1.2 mm and indicates a far from static environment at the Bramley Drive site. It is obvious that there are sharp changes in deviation throughout the borehole. These predominantly occur in the same depths, suggesting that the heterogeneity of the volcaniclastic materials forming the slope may play an essential part in either amplifying or dampening the processes acting on the slope.

This aspect will be considered in more detail within the Chapter 4, particularly the possibility that changes in displacement correlate with specific horizons within the slope.

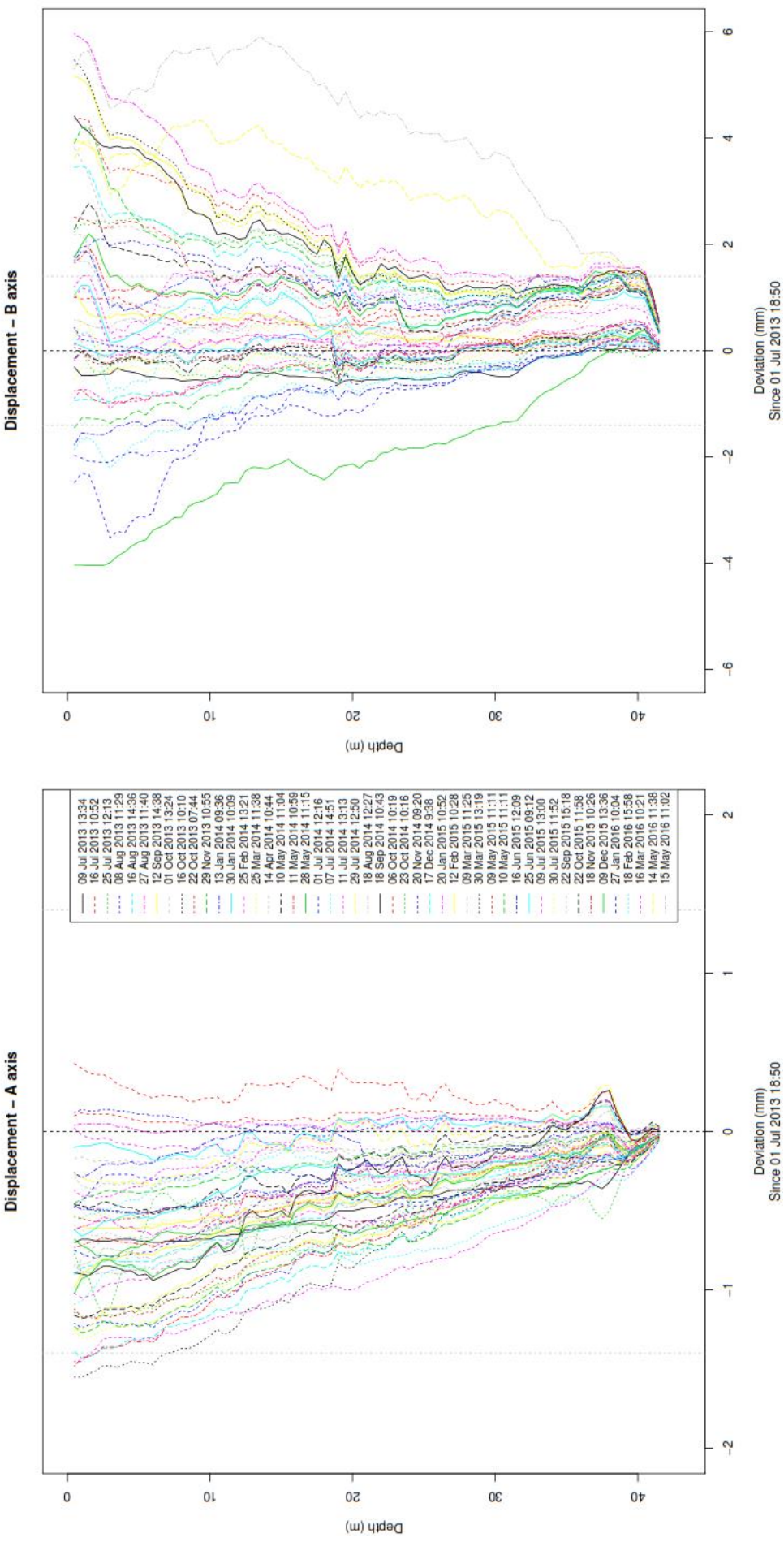

Figure 3.8: Cumulative deviation plots of both the (a) A-axis and (b) B-axis, including recording beginning July 2013 until May 2016. Instrument error bars are shown as grey dotted lines at 1.4 mm, however due to the observed link between recordings, data within these error bars are mostly relevant. Displacement in the A-axis is primarily in a negative direction, meaning displacement prefers a southern direction when using 1 July 2013 18:50 as an initial recording, while the B-axis prefers a positive direction, meaning displacement is primarily in the eastern direction.

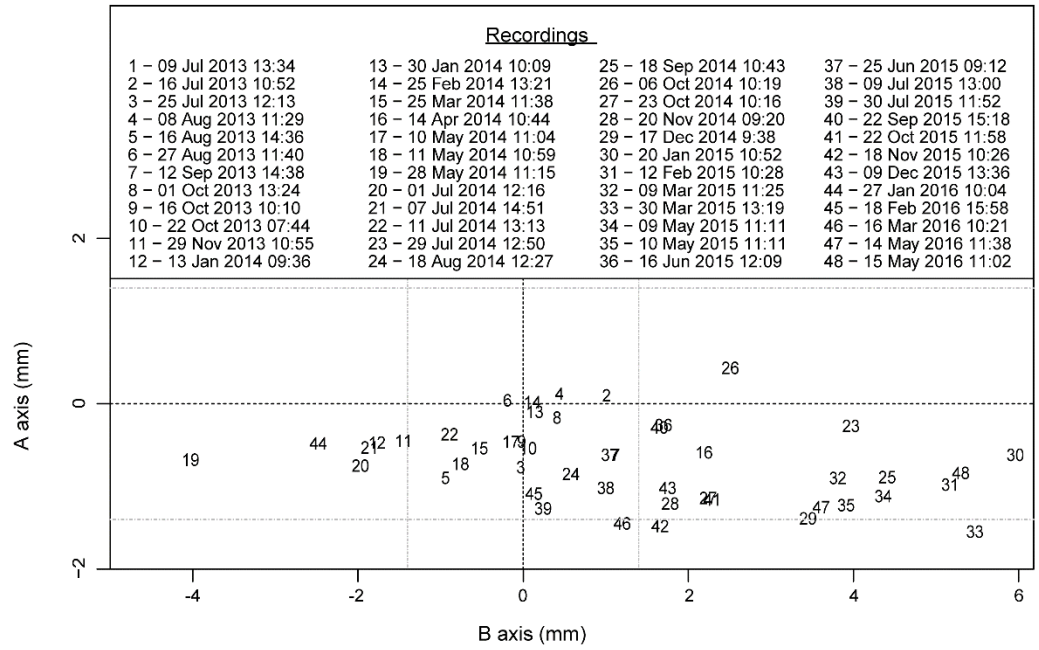

Figure 3.9: Plan view of borehole location. All 48 recordings shown in regards to their cumulative deviation from 1 July 2013 18:50 at 1 m below ground surface. There is a general trend towards the southeast, with deviation possibly increasing with time.

In plan view (Figure 3.9), a southeast trend is clearly visible, however the cause for this trend is not obvious. This will be discussed further in Chapter 4.

3.3.1.3 Yearly deviation

Using the first inclinometer measurement recorded at 18:50 on the 1st of July 2013 as the baseline for consistency, years 2013-2014, 2014-2015, and 2015-2016 were separated in an attempt to find a yearly trend in the inclinometer data (Figure 3.10). Displacement in the A-axis is almost entirely in the negative (southern) direction, and usually less than the assumed instrument error, which is ±1.2 mm. Hence, it could be argued that it is not significant. However, due to the systematic variations displayed it is suggested that, even if it doesn't exceed the assumed instrumental error it should be regarded as a relevant, oscillating and negative trend observed each year. With regards to the B-axis, results are much less equivocal. Relatively large displacements occur from time to time, with displacement reaching up to 6 mm from the initial profile, although most measurements are within the assumed error of the inclinometer. These changes appear to be conclusive evidence of cyclic movement in some form.

Seasonality doesn't seem to play a large factor in displacement direction. For 2013-2014, May showed the largest negative (western) B-axis displacement with 4 mm from the boreholes starting location, while April had the most positive displacement (eastern) of approximately 2 mm. Further examples are recordings in May, October, January,

February, August and July showing almost identical cumulative deviation to the original measurement in July 2013. Expected average temperatures for summer and winter months do seem to have an effect on total cumulative displacement, however, with warmer months like January, February, March, April and May deviating the most from the baseline survey, meaning air temperature when the test was recorded may be important, and will need to be investigated.

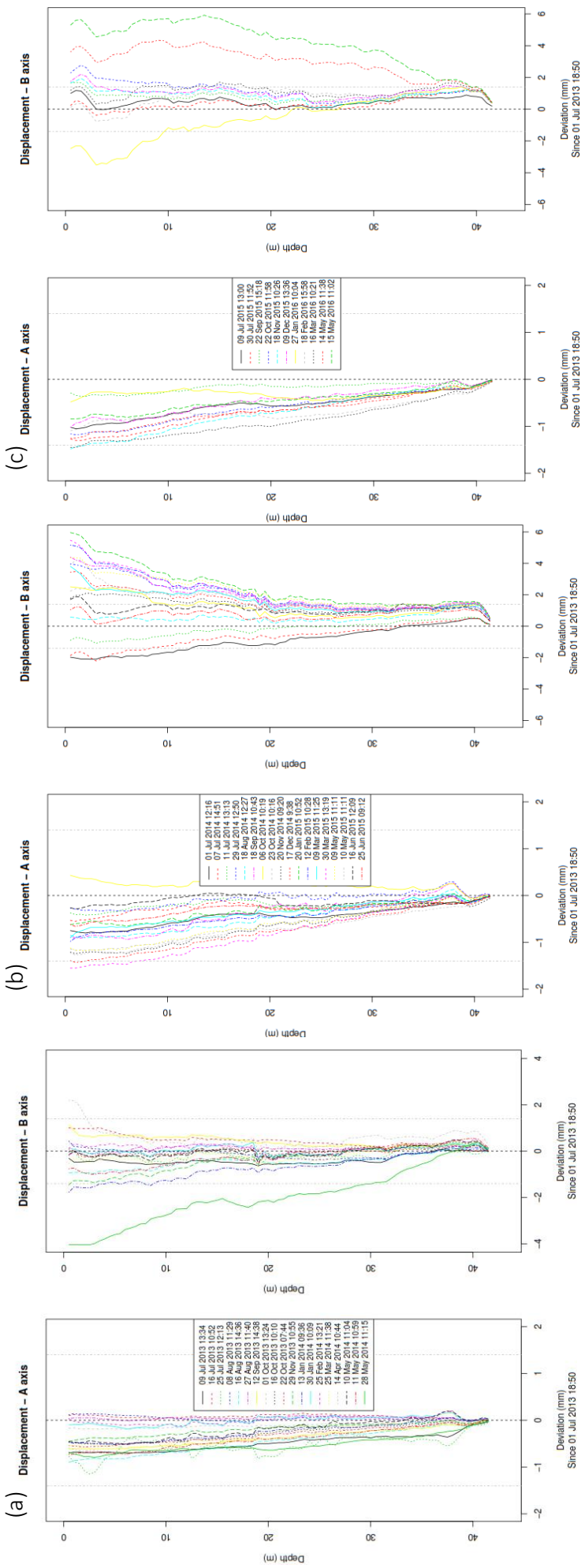

Figure 3.10: Cumulative deviation plots over the years (a) 2013-2014, (b) 2014-2015, (c) 2015-2016. Displacement tend to exceed the limitations of the instrument in the A-axis giving inconclusive results, while deviation in the B-axis is large enough to conclude that there is a definitive east-west movement. No clear yearly cycle is apparent; however seasonal effects may dictate deviation size from the initial recording. Time of day seems to be the most obvious cause of the borehole inclinometer direction.

3.3.1.4 Daily deviation

As stated earlier, half-hourly to hourly borehole inclinometer readings have been completed over short periods in an attempt to observe diurnal ground displacement. Once a year, a class of students from the University of Waikato use the Bramley Drive site as a field trip location. Over a weekend, multiple borehole inclinometer recordings are completed in approximately 1 hour intervals in the middle of the day over both Saturday and Sunday. These data, along with data collected on the 15th of April 2016 and 14-15th of November that span 12 hour and 25 hour periods respectively, in half hour intervals will be used to assess diurnal or semi-diurnal displacements.

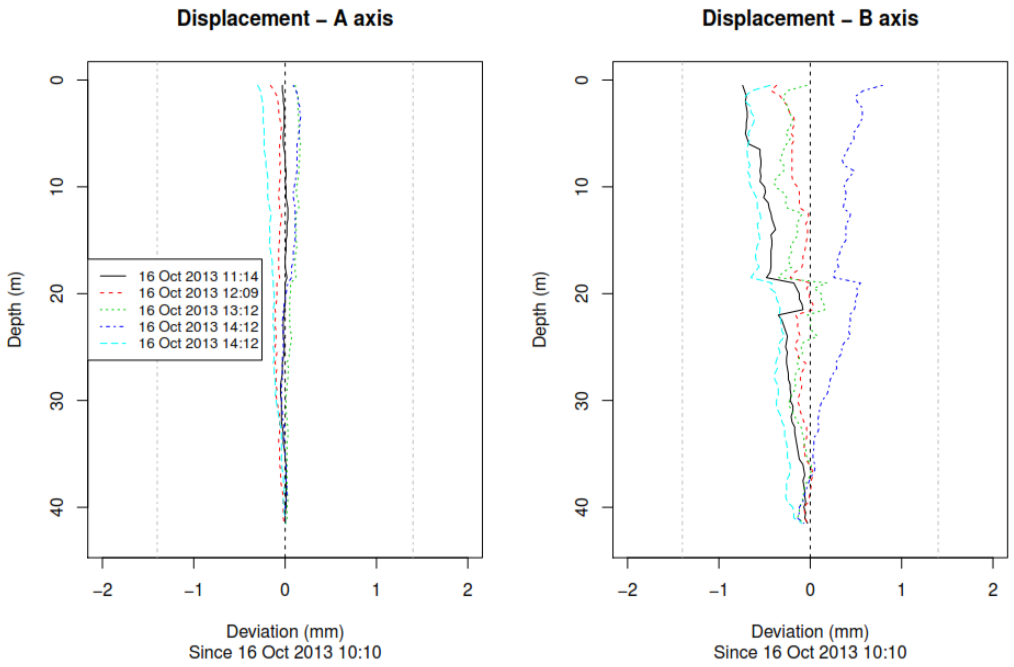

Figure 3.11: Cumulative deviation recorded on the 16th of October 2013.

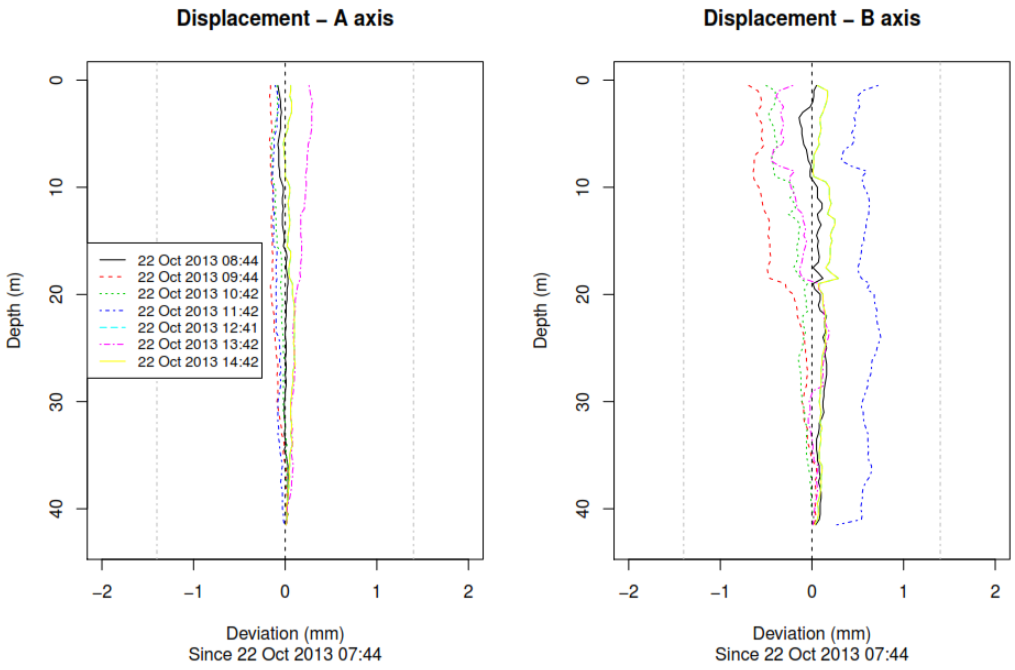

Figure 3.12: Cumulative deviation recorded on the 22th of October 2013.

From Figure 3.11 and Figure 3.12 presented above, and the results of Moon *et al.* (2015a), which used the same data with a different methodology, it's now obvious that a measurable displacement occurs throughout the day.

The data collected on the 16th (Figure 3.11) and 22nd of October 2013 (Figure 3.12) were collected by staff familiar with the equipment so there is high confidence in the resulting data even though the variations are smaller than the assumed limits of the inclinometer, meaning the data may possibly have no significance. The deviation occurring at 11:42 where displacement is completely disconnected from the first (base) inclinometer reading measured at 07:44 in the B-axis on the 22nd of October 2013 may not be a valid measurement is it is offset from zero at the base. The sharp change in deviation at approximately 20m in the B-axis on the 16th of October 2013 should also be treated with caution, although this is present in all the measurements.

Greater displacement was observed in the B-axis for both days.

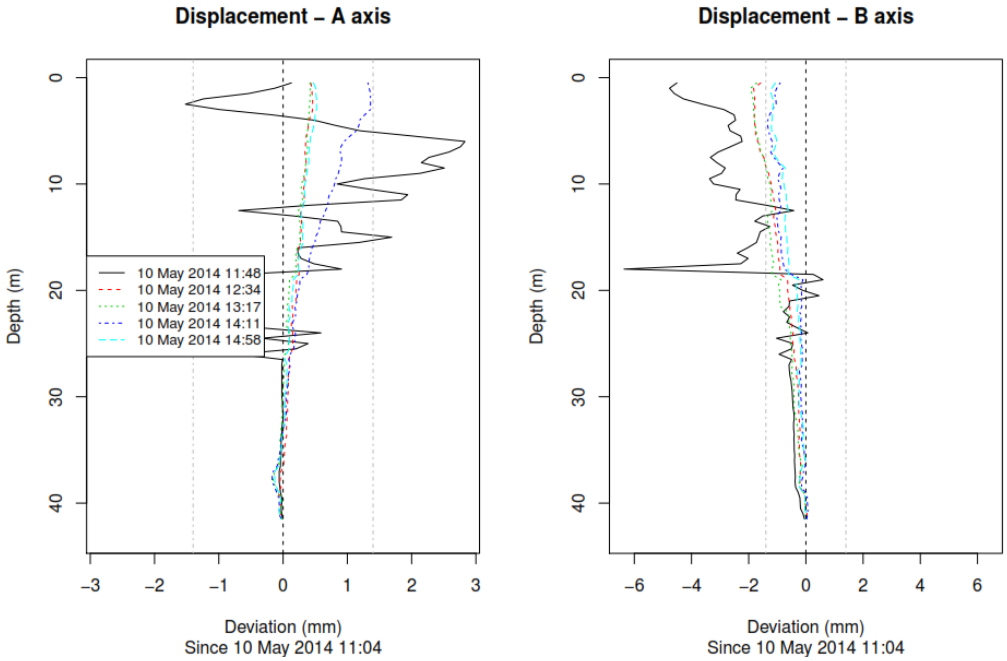

Figure 3.13: Cumulative deviation recorded on the 10th of May 2014.

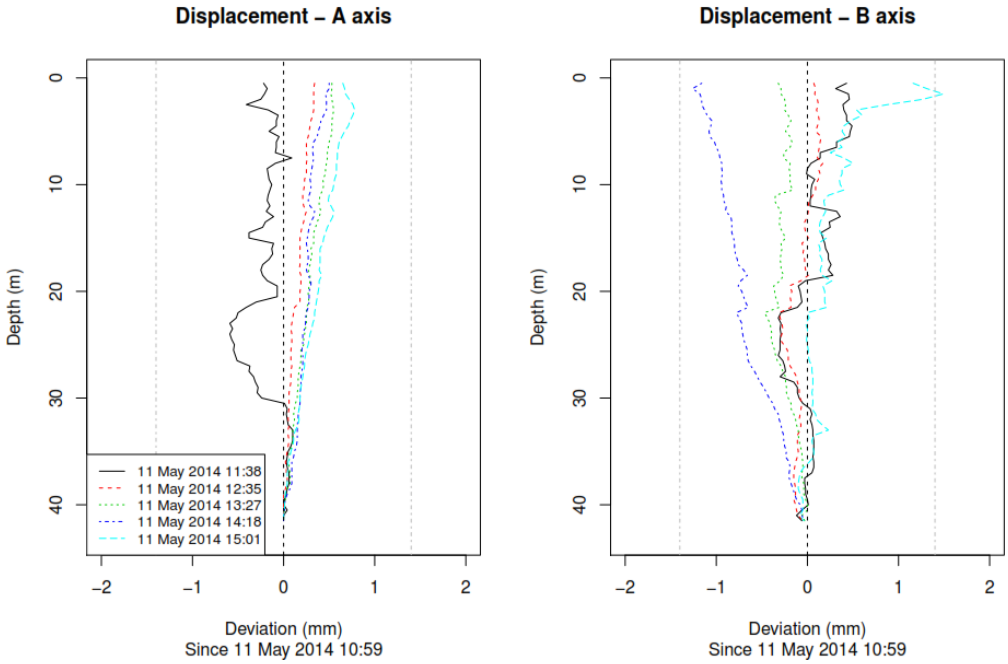

Figure 3.14: Cumulative deviation recorded on the 11th of May 2014.

These measurements recorded on the 10th (Figure 3.13) and 11th of May 2014 (Figure 3.14) were by various operators throughout an undergraduate field trip. This was their first use of the equipment, and therefore some data may be incorrect due to operator error. This is most apparent in measurements taken at 11:48 on 10 May 2014 and 11:38 on the 11th of May 2014, where sharp deviations occur that do not follow patterns observed at other times. Overall, the displacement in the A-axis was always positive, with displacement in the B-axis on the 10th of May 2014 beginning negative and

moving in a positive direction, while the 11th of May 2014 beginning positive and moving to a negative direction, until jumping sharply back in a positive direction between 14:18 and 15:01.

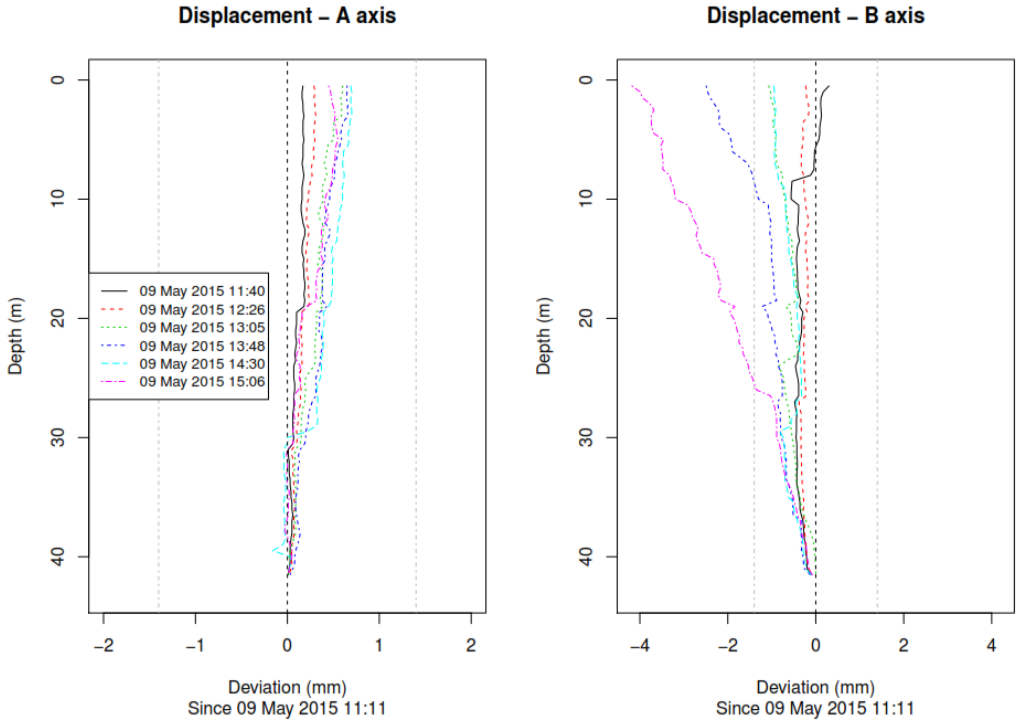

Figure 3.15: Cumulative deviation recorded on the 9th of May 2015.

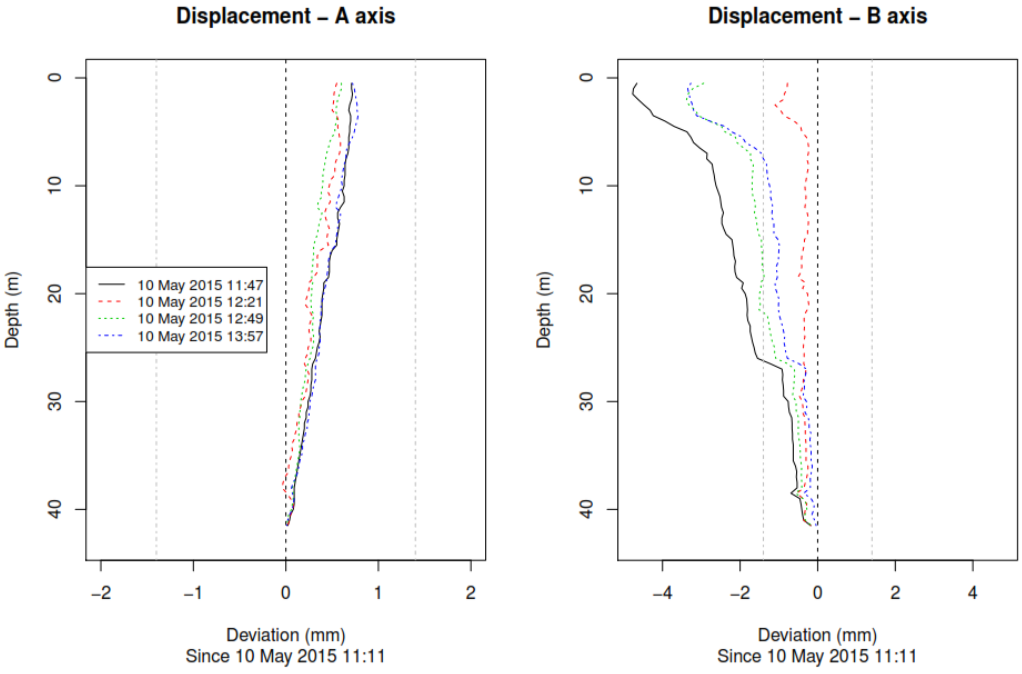

Figure 3.16: Cumulative deviation recorded on the 10th of May 2015.

In 2015, the A-axis followed the same trend as the previous two years, only showing displacement in the positive direction. As for the B-axis, movement was negative with

significant displacement of over 4 mm on both the 9th (Figure 3.15) and 10th of May 2015 (Figure 3.16). For all measurements taken on those days, no obvious pattern of generally moving left or right is apparent. However, very rapid changes occurred, with cumulative displacement rapidly moving from maximum values to being almost indistinguishable to the original measurement (or vice versa) between consecutive readings. This was most apparent in the B-axis on both days, with a change of approximately 3 mm between 14:30 and 15:06 on the 9th of May 2015, and a change of almost 4 mm between 11:47 and 12:21 on the 10th of May 2015.

Discernible "kinks" are evident the profile at 10, 20, and 28 m depth in B-axis for the 9th of May 2015, as well as at 6, 28 and 39 m in B-axis on the 10th of May 2015. The significance of these in relation to the geologic profile will be discussed in the Chapter 4.

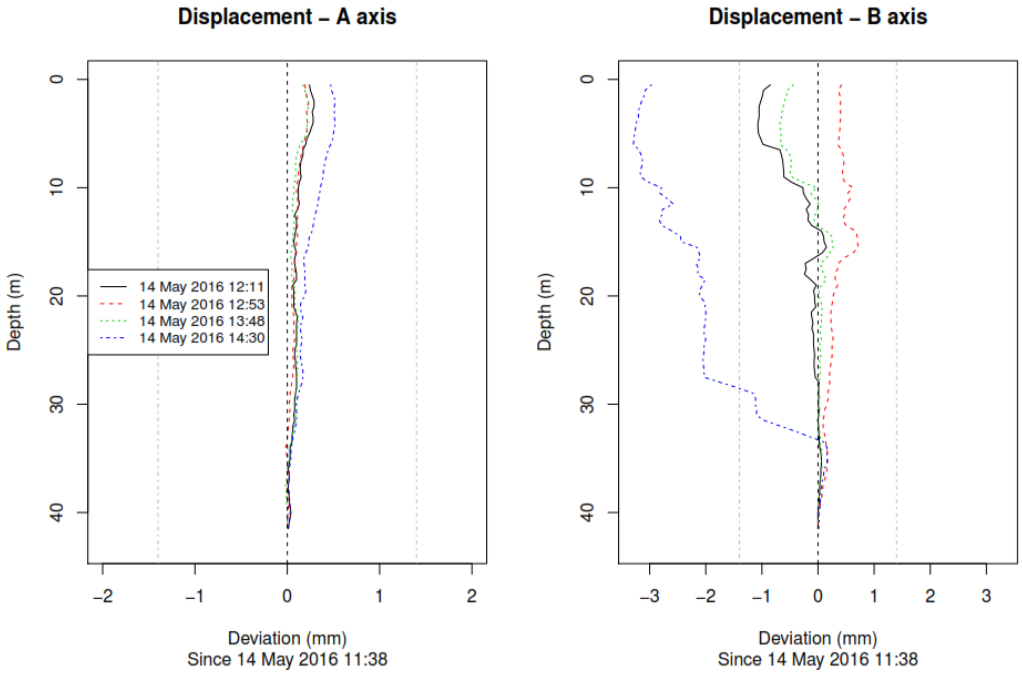

Figure 3.17: Cumulative deviation recorded on the 14th of May 2016.

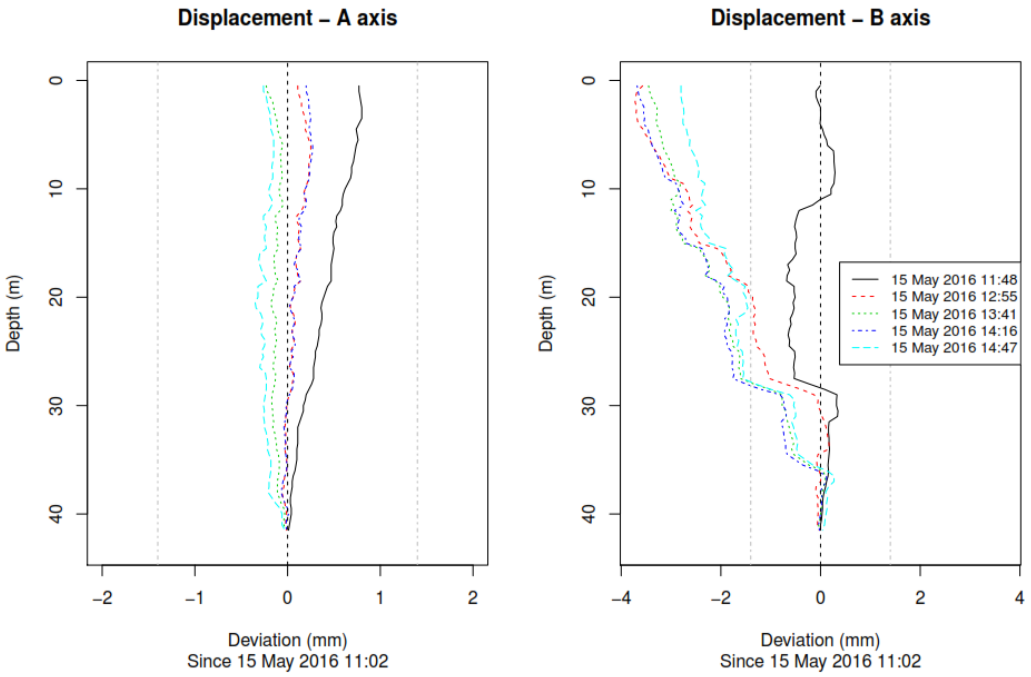

Figure 3.18: Cumulative deviation recorded on the 15th of May 2016.

Once again, on the 14th (Figure 3.17) and 15th of May 2016 (Figure 3.18), the A-axis deviation was only in a positive direction. However, the B-axis appears to be very different to the previous year's observations and could be due to slope evolution between successive years or systematic operator error. There were some similarities to 2015, with the maximum displacement in the negative direction reaching 4 mm, and pronounced sharp changes in deviation at approximately 28-29 m depth on the B-axis. It was also noted that measurements at or near noon had the least deviation from the original reading, with the deviations getting progressively larger later in the afternoon.

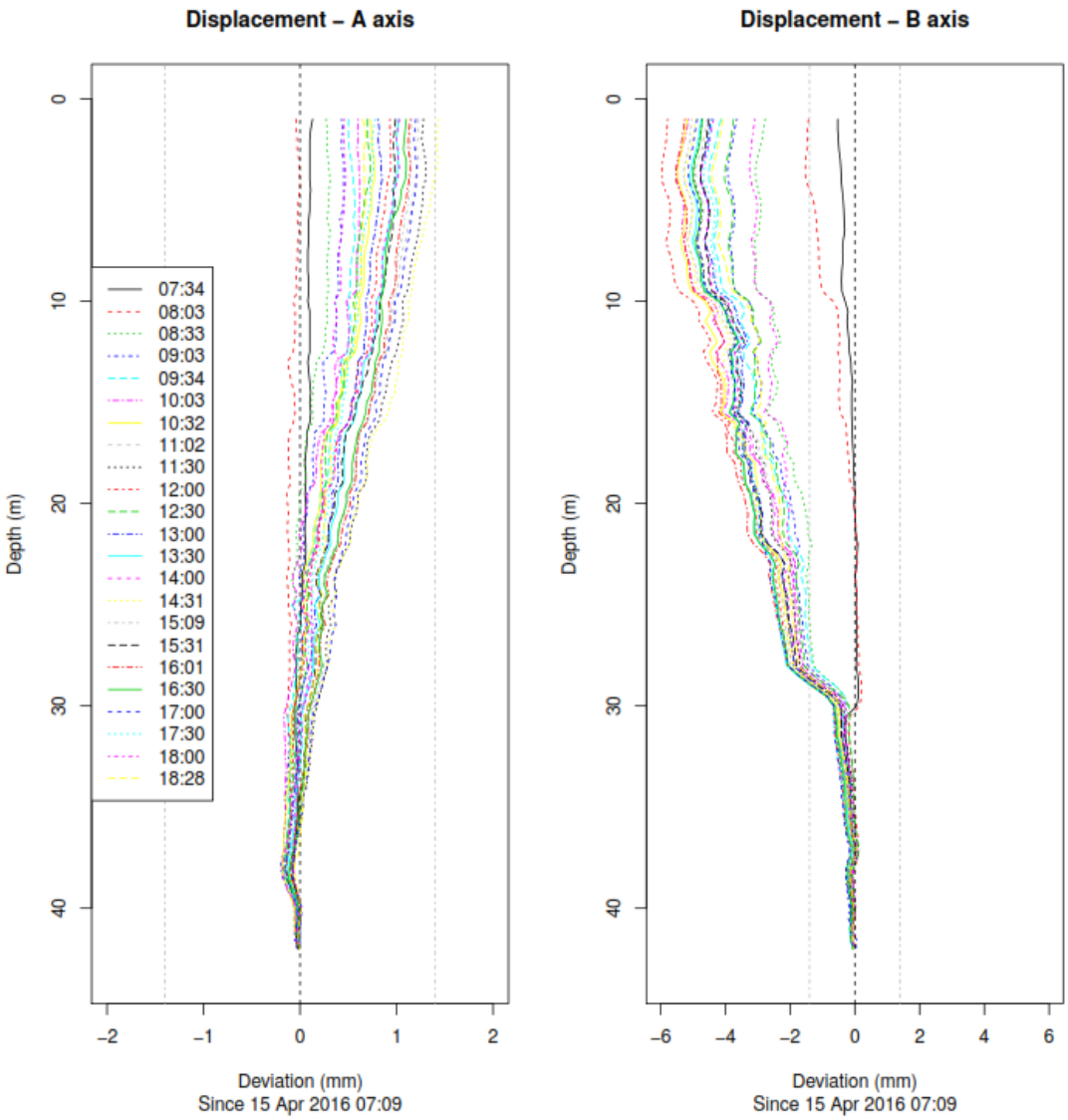

Figure 3.19: Cumulative deviation recorded on the 15th of May 2016, covering a 12-hour period, with recordings completed every half-hour. The initial recording of 07:09 on the 15th of April 2016 was used as a base, returning the general observation of a primarily positive trend in the A-axis and a negative trend in the B-axis.

Based on the previous data, it was decided that it was important to obtain longer sequences of repeated measurements during a day as it had become apparent that diurnal changes caused by temperature changes and possibly Earth tides, as suggested by Moon *et al.* (2015a), could play a major role in the measured cyclic movements within the borehole. It was planned to record at least 12 continuous hours of measurements in April 2016 using a single operator, and at least 24 continuous hours using multiple operators on shifts in November 2016 with the shortest possible intervals between measurements

Due to limited daylight in April 2016 only 11.5 hours of measurements at half hour intervals was possible, providing 24 observations (Figure 3.19). The plotted data

support the hypothesis that the observed movements discussed above did not show a yearly or seasonal trend in cumulative deviation, but a daily cycle such that the time of measurement affected the measured profile. This is illustrated by comparing the difference for the 15th of April 2016 data using the first test of the morning (07:09) to calculate cumulative deviation (Figure 3.19), instead of the initial reading in July 2013 as the baseline (Figure 3.20).

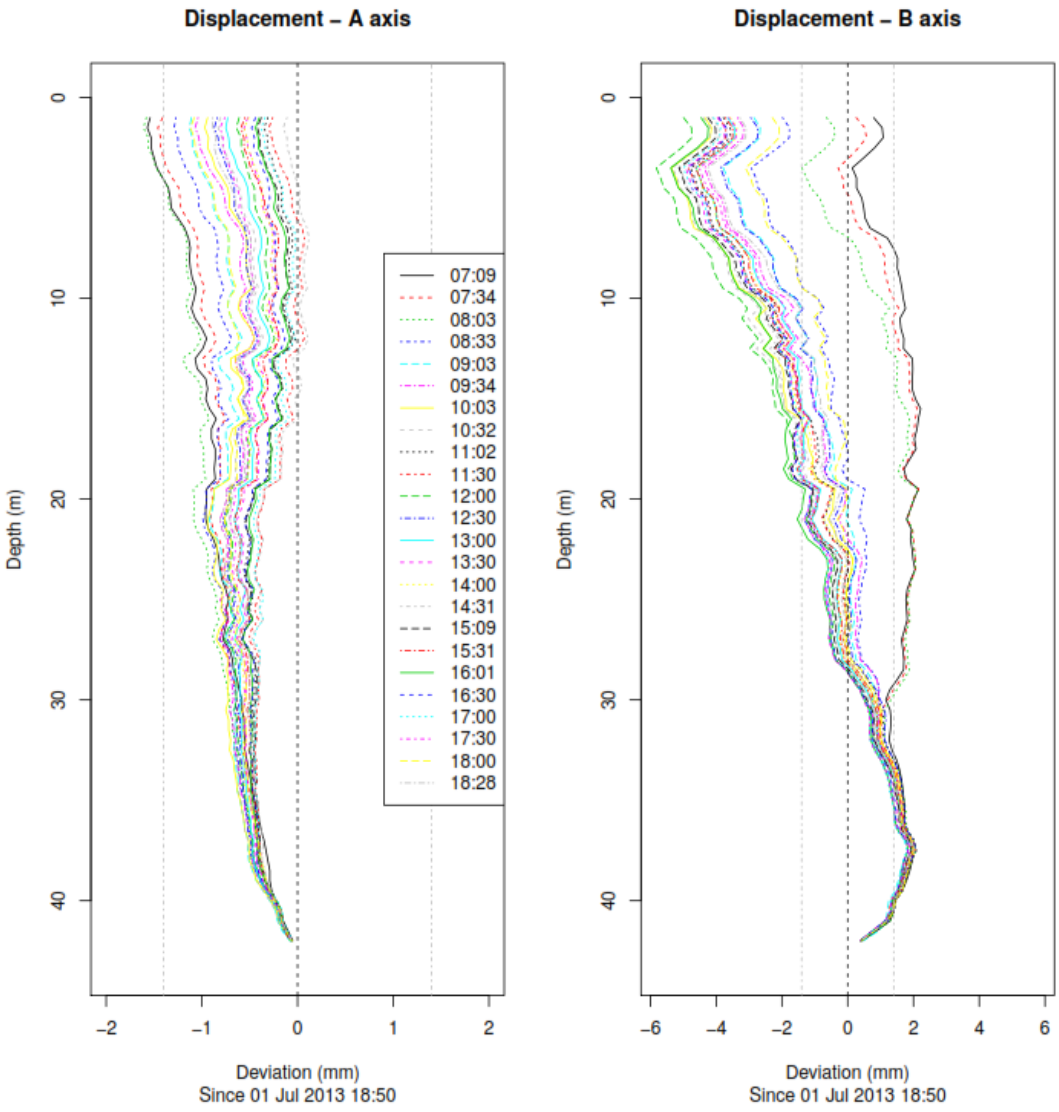

Figure 3.20: Cumulative deviation recorded on the 15th of May 2016, covering a 12-hour period, with recordings completed every half-hour. The initial recording of 18:50 on the 1st of July 2013 was used as a base to see if the initial recording would greatly effect deviation direction and/or magnitude.

Doing so changes the apparent placement of the A-axis. For Figure 3.19 all A-axis displacement occurs in the positive direction, while in Figure 3.20 all displacement is negative. Additionally, comparing cumulative deviation at 07:34 for both figures show that the initial, baseline recording greatly changes the boreholes apparent location at that time, with no deviation occurring between 07:09 to 07:34 in Figure 3.19, and maximum, negative deviation at 07:34 in Figure 3.20.

The B-axis cumulative deviation exceeds 6 mm in both Figure 3.19 and Figure 3.20, which is six times larger than deviation observed in the A-axis. The two figures also share the trait of sharply deviating westward at approximately 08:30. There is also a sharp deviation at a depth of approximately 20 m, showing almost 2 mm of displacement over 0.5 m, which was also evident in earlier sets of hourly measurements made by undergraduate students. Other sharp changes are also apparent and will be investigated further in Chapter 4.

The idea of gathering additional inclinometer recordings to cover an entire lunar day was decided once the diurnal movement of the borehole was observed in April 2016. As the Moon's rotation around the Earth relative to a fixed Earth location is approximately 25 hours (including the movement of the Earth itself), thus 25 continuous hours was proposed. This was undertaken with measurements beginning at 14:32 on the 14th of November 2016.

The A-axis displays both positive and negative displacement throughout the period, while displacement is almost entirely negative within the B-axis (Figure 3.21). As this was recorded over a full lunar cycle it can be assumed diurnal movement of the Bramley Drive site is irregular, having the ability to fluctuate more or less on different days. It also shows that any net displacement caused over one diurnal cycle may be permanent. Multiple depths are noted to show sharp movements within the borehole and will be investigated further in Chapter 4.

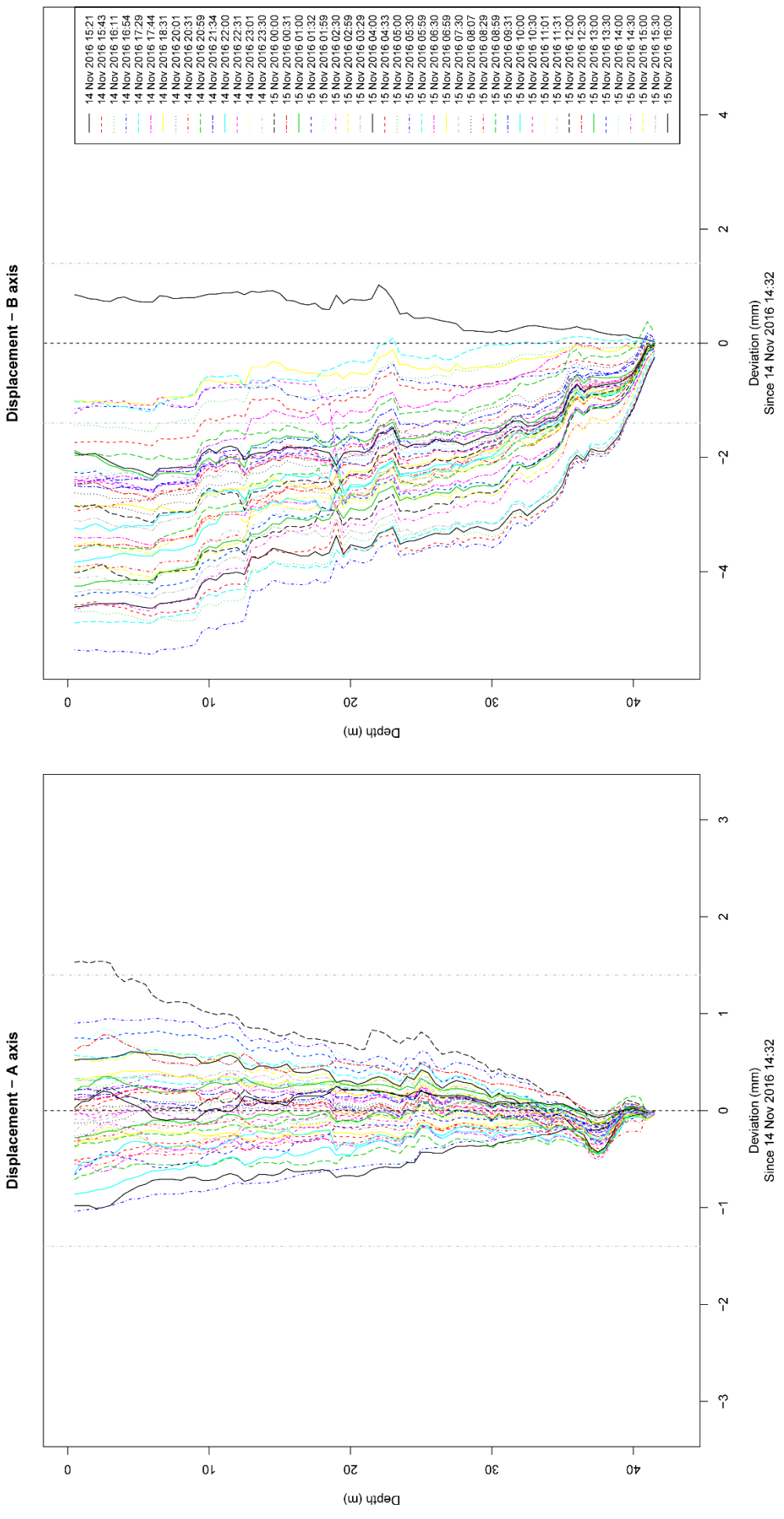

Figure 3.21: Cumulative deviation recorded on the 14-15th of November 2016, covering a 25-hour period, with recordings completed every half-hour. The initial recording of 14:32 on the 14th of November 2016 was used as a baseline, returning the general observation of a primarily negative trend in the B-axis.

3.3.2 Summary

The borehole inclinometer recordings over the past four years raise many more questions than answers. There are no obvious long-term trends, with the time of the year likely having a minor effect, however, there are clearly cyclical daily movements observed. Cumulative displacement never smoothly increased or decreased showing a direct relationship with the time of the day and amplitude, but there was usually at least a general trend in either a positive or negative direction depending on when the measurement relative to the initial recording used as the baseline profile. There does appear to be a trend for the amplitude of the daily displacements to increase since July 2013.

To summarise what was observed in the borehole inclinometer recordings:

1. From July 2013 to May 2016, the borehole profile has undergone a very slight change in shape;
2. No consistent deviation associated with a potential shear surface is apparent anywhere in the borehole;
3. The B-axis appears to be much more active, with higher magnitude displacements than the A-axis. Measurements switching the A- and B- axes confirmed that the displacement magnitudes are larger for the B-axis, and that it was not an instrument error;
4. Sharp but minor changes in deviation occur throughout the borehole inclinometer readings, possibly caused by changes in local stratigraphy;
5. When using the 1st of July 2013 as an initial measurement, recordings made in the morning and afternoon are predominantly in a negative (south) direction, while measurements close to noon appear to have the same shape as the baseline;
6. Seasonality doesn't seem to play a large factor in displacement direction. Summer and winter months do seem to have an effect on total cumulative displacement;
7. Changes in the borehole shape from the maximum deviation to almost none (and vice versa) can occur in less than one hour at times;
8. The direction of the final deviation (positive/negative) is dependent on the time of the initial measured profile.
9. Over a diurnal cycle, the net borehole movement, while small, may be permanent.

3.4 ACCELEROMETER AND WEATHER STATION OBSERVATIONS

The accelerometer was used to assess if the ground movements causing the changes in the borehole shape first observed by the borehole inclinometer could be due to weather effects including rainfall, air and soil temperature, and solar insolation. With the accelerometer pointing true north it is possible to split observations into respective axes, which were X (north-south), Y (east-west) as well as Z (elevation).

3.4.1 Observations at different time periods

This section of the thesis will examine the correlations between the accelerometer data and parameters measured by the weather station at Omokoroa.

3.4.1.1 Annual (2-year comparison)

In Figure 3.22 all recorded data beginning from late-June 2014 until August 2016 is shown, and highlights the different installation dates for the sensors. It is evident that there is a block of missing data from the 7th of November 2015 at 08:40 to the 17th of December 2015 at 02:30. The cause of this missing data is unknown and does not coincide with dates that the equipment was serviced or inclinometer measurements were made. It was likely caused by an interruption in the transfer of data to the server, as all recorded data was uploaded to a server via a cell phone link and not permanently recorded within the datalogger. Around this period the telecommunications company providing the cellular service made changes to the cell phone network in the area, which may have disrupted the data link.

Another known issue is that rainfall recorded by the rain gauge in January of 2015 was uncharacteristically low. This was found to be due to the tipping bucket mechanism inside rain gauge being covered by spider webs. Although these were removed when the gauge was serviced, it appears that they were rapidly reconstructed and prevented rainfall from being recorded. The fitting of protective mesh over the drainage holes in the base of the rain gauge stopped this problem. Unfortunately, comparison of rainfall data from the weather station with nearby stations showed very poor correlation due to the frequent occurrence of often intense, and very localised rain events within the Tauranga region (Quayle, 1984).

The measured accelerations in Y- and X-axes appear to be slightly biased due to the accelerometer not being perfectly level and set at exactly 0°T (Figure 3.23). The

levelling was achieved by relatively coarse adjustments of three screws in the base combined with a spirit level. Hence the X-axis data are predominantly positive while the Y-axis is primarily negative. For the purpose of this thesis the tilt bias in the accelerometer should not be an issue. However, manipulating the data to determine deviations without considering the tilt bias could skew any resulting outcome.

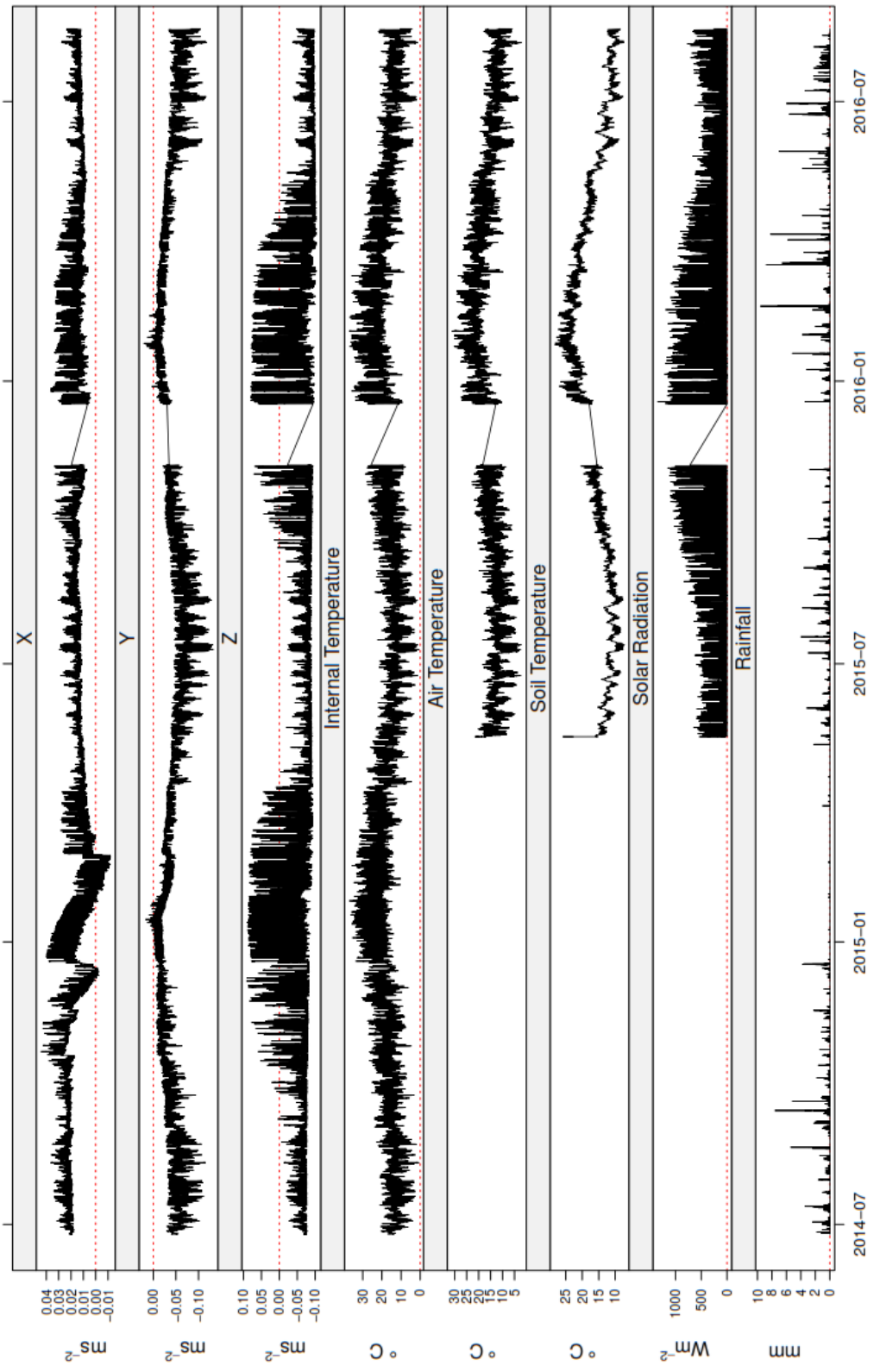

Figure 3.22: Raw accelerometer and weather station data spanning from late June 2014 until August 2016.

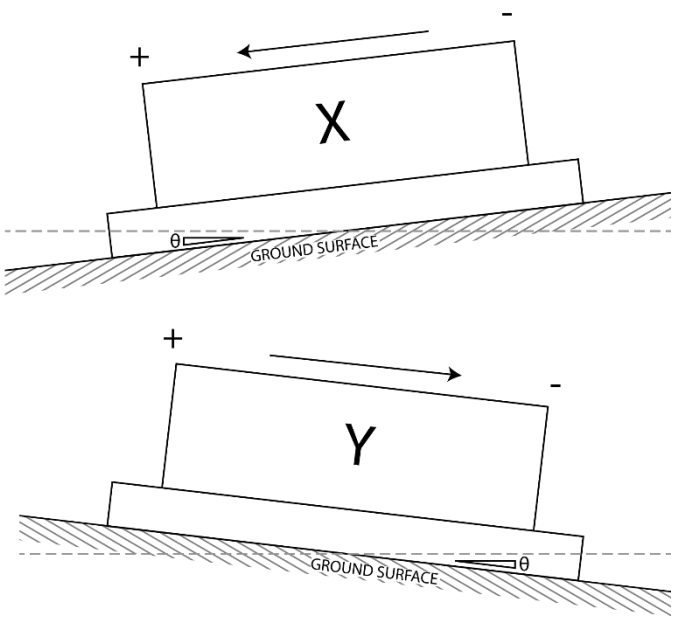

Figure 3.23: Illustration showing the observed tilt within the onsite accelerometer. Tilt leans positively for the X-axis and negatively for the Y axis, meaning acceleration changes will be slightly skewed in the northwest direction.

Temperature at the site has been recorded at three different locations on the weather station, with the surface temperature of the solar panel (internal temperature) being recorded the longest. The remaining measurements are from a shielded air temperature sensor at a height of ~2 m, and a soil temperature sensor located at a depth of 5 cm. All three show a general trend of higher temperatures, as well as larger diurnal changes in temperature, during the warmer seasons compared to the cooler seasons (Figure 3.24). Soil temperature clearly shows the effect of heat retention, with a much smaller range of temperature changes. Therefore, it is assumed that the temperature effect would greatly decrease with depth, which could be confirmed by installing additional thermal probes at greater depths.

As expected, solar radiation is higher in the summer months due to the Southern Hemispheres tilt toward the Sun in these months that makes the Sun radiate its rays at a steeper angle (increased inclination of Sun rays) in relation to the surface, as previously explained in Chapter 2, as well as the Earth being closer to the Sun at this time in the Earth's elliptical orbit.

Considering the accelerometer observations, the Y-axis (east-west) is primarily negative due to the tilt of the accelerometer, with a positive (eastward) trend from July to January and a negative (westward) trend from January to July. Fluctuations are also dampened in warmer months compared to cooler months, with sporadic, larger and

grouped amplifications occurring after June that seem to coincide with sharp changes in soil temperature.

For the X-axis (north-south) acceleration amplitudes are much lower, at less than half of acceleration observed in the Y-axis and a quarter of acceleration observed in the Z-axis. Also compared to the other axes, possible causes of its fluctuations are hard to identify. If looking at data from mid-2015 to mid-2016, an increase in acceleration in

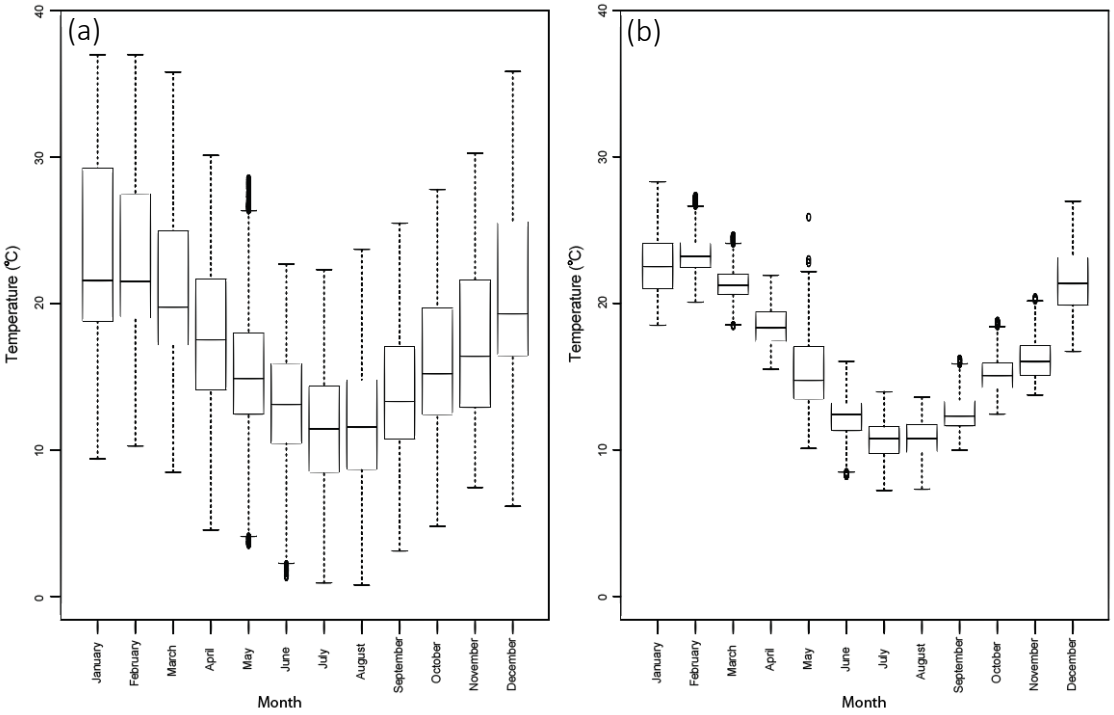

Figure 3.24: Box and Whisker plots of (a) internal temperature and (b) soil temperature over each month, using all available data.

warmer months is apparent, however data collected before mid-2015 does not show the same correlation and instead shows a higher "resting" state, as well as a sharp, negative deviation, which may have been caused by a one-off change in the N-S tilt of the instrument, beginning in late December 2014 and lasting a few months which does not occur in either the Y-axis or Z-axis.

A quick examination of the data shown in Figure 3.22 shows an apparent correlation between elevation (Z-axis) and temperature change. The resting, or baseline acceleration of between -0.05 ms^{-2} and -0.1 ms^{-2} has not changed over the past two years, but acceleration reaches up to almost 0.1 ms^{-2} in the warmer months and seems to be dependent on soil temperature. Months between December and April are the hottest at Omokoroa, with both internal temperature and soil temperature reflecting this at the weather station data. These months are also expected to have the largest

diurnal temperature range as explained earlier (Figure 3.24), and it the most likely cause of the increased acceleration in the Z-axis during warmer months.

3.4.1.2 The effect of rainfall and temperature change

Changes in both temperature and rainfall are proposed to have a major effect on the accelerometer recordings. Figure 3.22 shows the obvious link of soil temperature and acceleration in both the Y- and Z-axes, where larger amplitudes in acceleration are caused when there are larger changes in soil temperature over a full day. In the case of Figure 3.26 which is from the 1st of June until the 3rd of July 2016, the Y-axis peaks in a positive direction with maximum soil temperature while the Z-axis almost mirrors the Y-axis with maximum negative peaks. At this time of year acceleration amplitude in both the Y- and Z-axes seem similar (although mirrored), giving the appearance that the same diurnal causes may affect both the E-W component and elevation in the same way.

This is most obvious with the introduction of rainfall. Even small amounts of rainfall, which is assumed to be associated with an increase in cloud cover and reduced solar flux, dampens both the Y- and Z-axes. For this period in Figure 3.26, rainfall is associated with increases in soil temperature as raindrops are assumed to have the same temperature as ambient temperature (Byers *et al.*, 1949), which is retained overnight, reducing movement of the accelerometer.

Cloud cover also hinders solar irradiance, which both decreases available solar radiation that would heat soil, and reduces outgoing long wave surface radiation losses to the atmosphere (Figure 3.25) (Graham, 1991). In regards to rainfall itself, its effect is the continued dampening of the accelerometer records for days after the rainfall event and can be seen after each downpour.

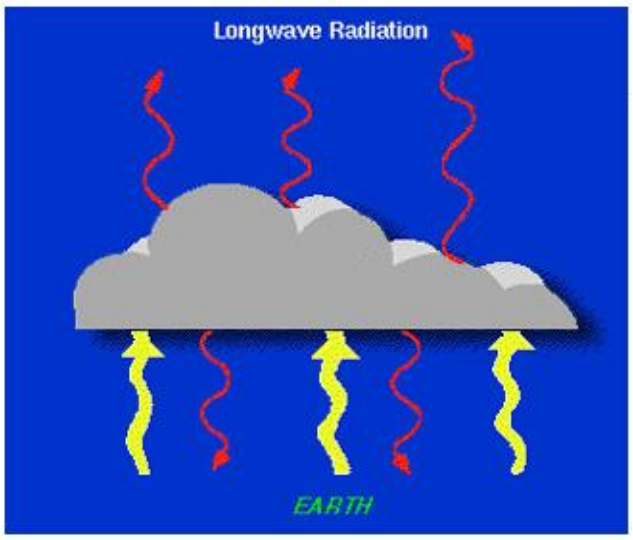

Figure 3.25: Illustration of longwave radiation waves emitted by the Earth. Note that some waves are absorbed and reemitted by a cloud, towards the surface. Thicker arrows indicate more energy (Graham, 1991)

When looking from the 20th of March to the 20th of April 2016 (Figure 3.27), which encompasses the day where multiple borehole inclinometer readings from the 15th of April were recorded, similarities with the recordings from June/July can be seen. The main being that when rainfall is introduced, the diurnal soil temperature range is reduced, dampening both Y- and Z-axes.

However, the amplitude in the Z-axis has more than doubled at points, while Y-axis variation is much less, at almost half of that shown in Figure 3.26. The two primary causes of the changes observed in the Y- and Z-axes must be due to increased solar irradiation and soil temperature in in these months (Figure 3.24), which would explain the steep increase in Z-axis acceleration (elevation). What is surprising is that maximum positive Z-axis acceleration now occurs around noon instead of midnight.

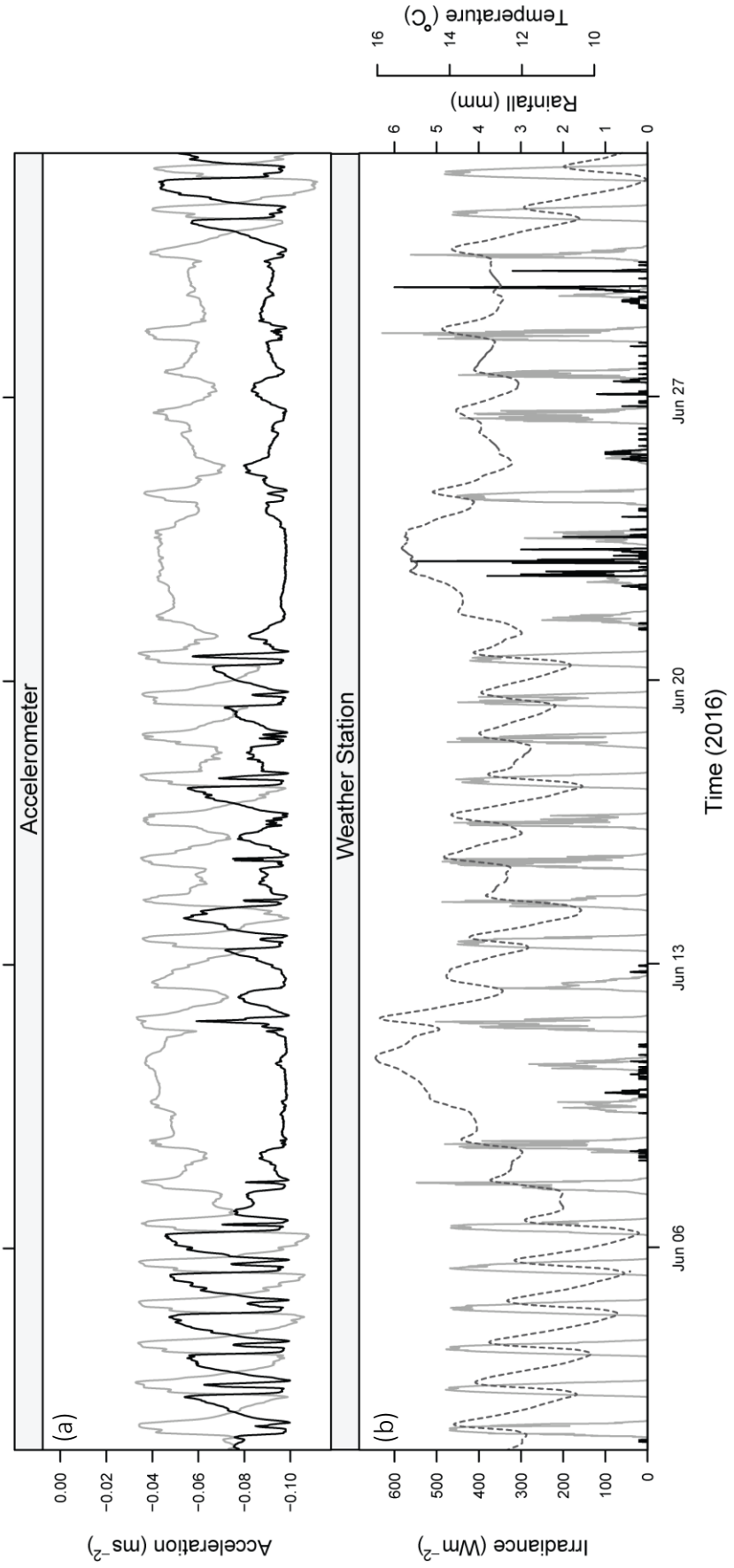

Figure 3.26: (a) Plot comparing acceleration in the Z-axis (black) to Y axis (grey). (b) Showing the relationship between rainfall (black), solar irradiance (grey) and soil temperature (dotted).

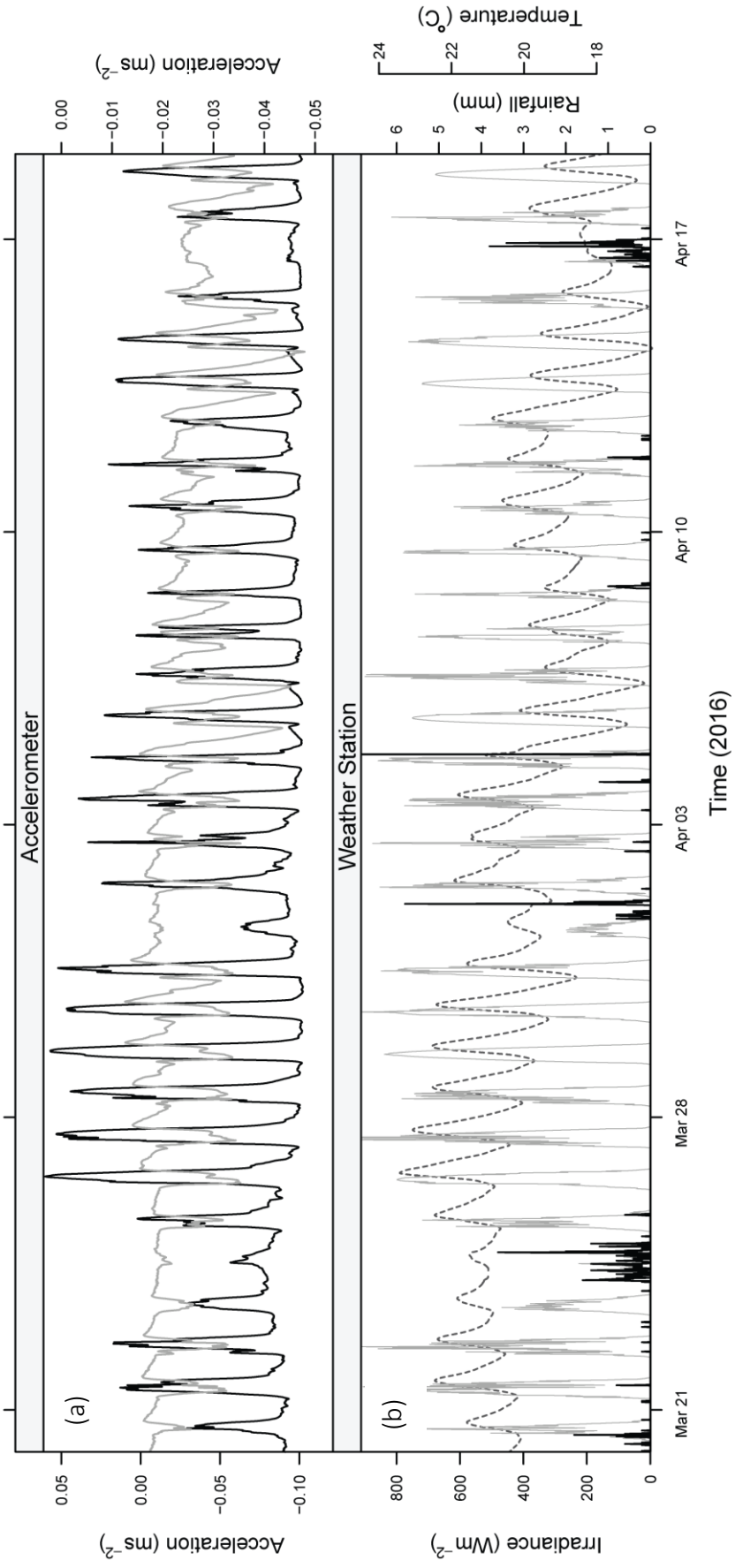

Figure 3.27: (a) Plot comparing acceleration in the Z-axis (black) to Y axis (grey). (b) Showing the relationship between rainfall (black), solar irradiance (grey) and soil temperature (dotted).

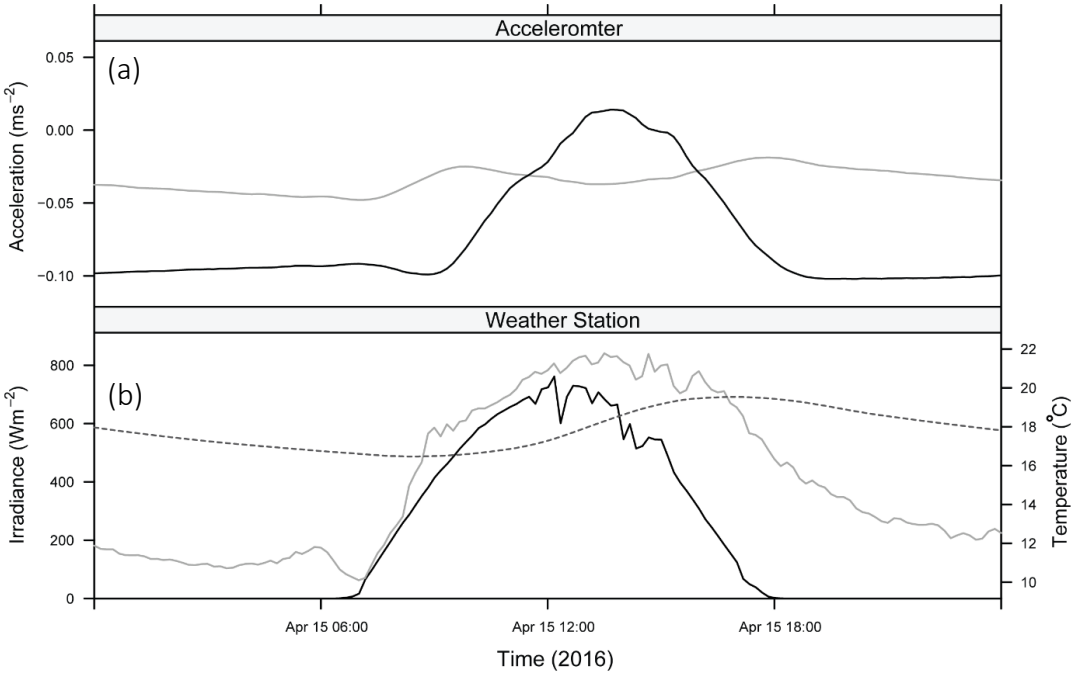

Figure 3.28: (a) Plot comparing acceleration in the Z-axis (black) to Y-axis (grey). (b) Showing the relationship between solar irradiance (black), air temperature (grey) and soil temperature (dotted).

Figure 3.28 shows both accelerometer (Y- and Z-axis) and weather station (solar irradiance, soil temperature and air temperature) data for the 15th of April 2016, which is the same day that half-hour inclinometer readings were taken. Once again acceleration in the Z-axis is greatly affected by temperature change caused by the increase in solar irradiance, in this case in a positive direction. As for acceleration in the Y-axis, minor movement is observed, with peaks around 10:00 and 18:00 and a minimum at approximately 13:00. Solar irradiance begins at sunrise (06:42), reaches a maximum at 12:00 where sunlight is at its steepest angle, then falls until reaching sunset (17:49), returning to 0 Wm^{-2}.

Minor cloud cover throughout the day likely caused the observed slight dips in solar irradiance. As expected, air temperature is correlated with solar irradiance, with a sharp increase in temperature as irradiance increases in the morning. Air temperature then reaches its peak along with irradiance, where it stays for the afternoon until irradiance drops enough to decrease air temperature in the late afternoon, where it continues to decrease overnight. Finally, soil temperature is lagged and much less variable compared to air temperature, it also does not seem to affect either the Y- or Z-axis, as most acceleration change had occurred well before soil temperature began to rise. As the

soil temperature probe is 5cm below the soil and thus below the accelerometer, air temperature seems to be a better option to monitor diurnal changes in the Z-axis.

1.1.1. One second data

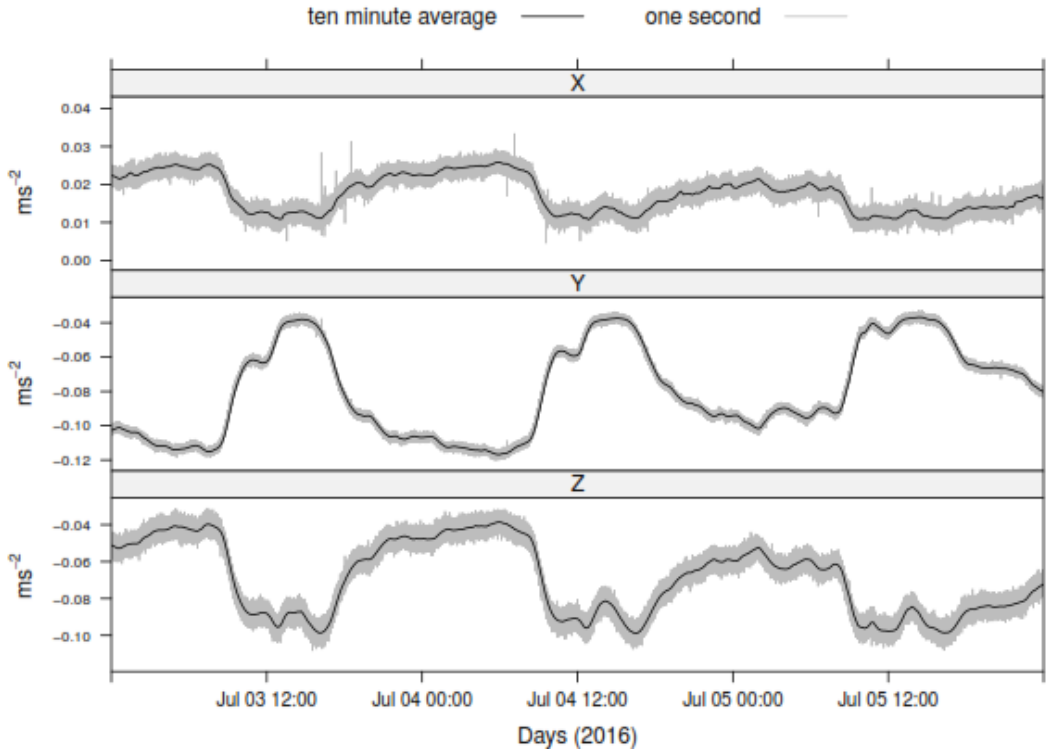

Figure 3.29: Comparison of averaged 10-minute data and continuous one-second data.

As all previous accelerometer data has been an average over a 10-minute interval, it is important to ensure using 10-minute average recordings are suitable. Figure 3.29 shows a few days of data of both one-second measurements and 10-minute averages between the 3rd of July and 6th of July 2016. Daily noise has been dampened by taking averages, but the trend is the same, indicating that the use of 10-minute averaged data is adequate to see the overall acceleration patterns. It should be noted that that the Y-axis on these days shows much less noise when observing the one second recordings, compared to both X- and Z-axes.

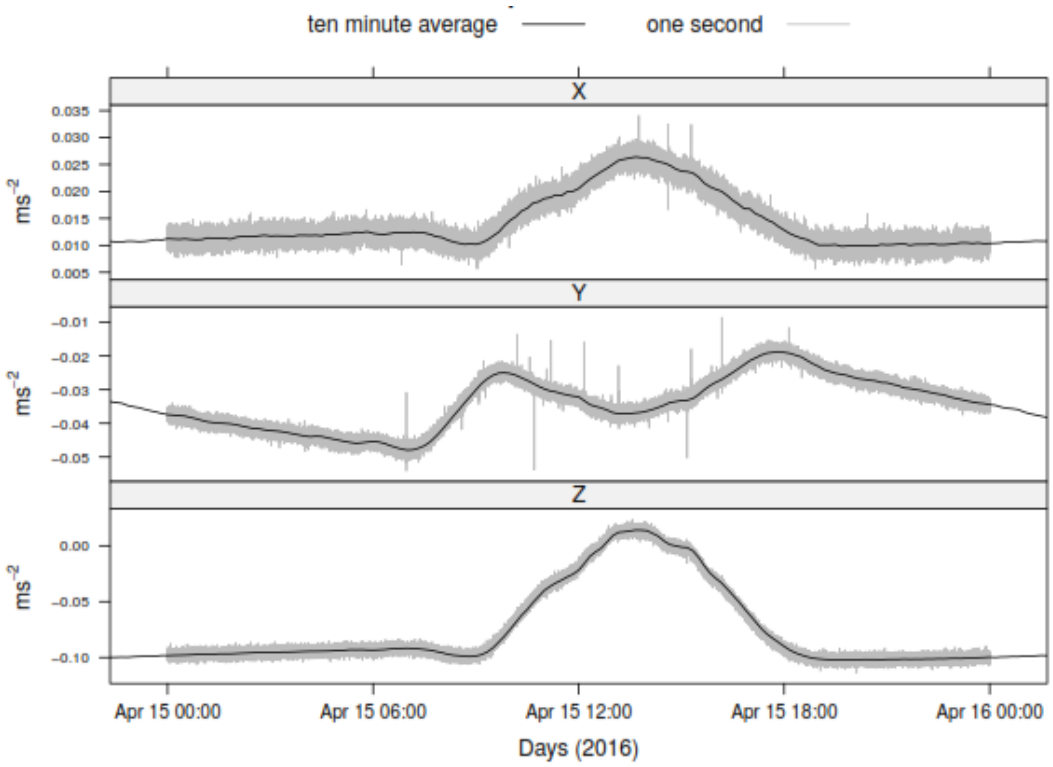

Figure 3.30: Comparison of averaged 10-minute data and continuous one second data.

Figure 3.30 shows 10-minute average data and one second data for the 15th of April 2016, which is the same day that half-hour inclinometer readings were taken. Large outliers evident in the one-second data are not shown in the averaged 10-minute data which is beneficial when looking at the trend. These outliers could be caused by a plethora of unrelated ground vibrations that could not be predicted or accounted for when looking at constant diurnal processes and may include one off ground vibrations caused by vehicles, animals and other anthropogenic causes such as operating the inclinometer.

The constant hum shown in both Figure 3.29 and Figure 3.30 reveal the presence of minor but constant high frequency waves, better known as microseisms. To find what frequencies are observed manipulation of the one second data will be undertaken using spectrum analysis in the Chapter 4.

3.4.2 Summary

Data recorded by both the accelerometer and weather station over the past two years gives some idea of what diurnal and seasonal factors may be causing ground movement at Omokoroa, the most obvious being the combined effect of solar irradiance (temperature) and rainfall. At its most basic, acceleration fluctuations in the Y-axis are at their largest in the cooler months, while acceleration fluctuations in the Z-axis are

at a maximum in the warmer months. Acceleration in the X-axis is much smaller than the other axes, and often reflects the acceleration change observed in the Z-axis with a smaller amplitude. However, the accelerometer instrument used is most likely tilted, thus judging acceleration by how often it is trending negatively or positively could be misleading. It also means manipulation of the data, such as double integration to extract deviations, should be done with extreme care.

To summarise what was observed in the accelerometer and weather station data:

1. X-, Y- and Z-axes all show a yearly cycle that has not changed since data has been recorded;
2. There is an apparent correlation between the Z-axis accelerations and temperature;
3. Maximum acceleration fluctuations occur in the Z-axis during warmer (late summer) months, while maximum acceleration fluctuations occur in the Y-axis during cooler (late winter) months;
4. The internal temperature of the solar panel follows a similar trend to air temperature, while soil temperature lags behind the other two. The soil also retains heat for longer, depending on the soil moisture content;
5. All three temperature probes are directly correlated to the amount of solar irradiation, which appears to vary with amount and type of cloud cover (although this has not been measured at the site);
6. Solar irradiance is highest in the summer months, when the Earth is also closest to the Sun;
7. Rainfall brings with it increased cloud cover, dampening the fluctuations in soil temperature, and sometimes increasing soil temperature;
8. Rainfall also appears to dampen acceleration change in all axes during the rainfall event, as well as a few days after;
9. Trends in the Z-axis can be unpredictable with maximums occurring either at noon or midnight with no obvious reason why;
10. 10-minute averaged recording are an accurate reflection of the one second data, while removing outliers;
11. One-second data shows an obvious hum throughout the day, which includes high frequency waves known as microseisms.

CHAPTER 4

INTERPRETATION

4.1 INTRODUCTION

The ground movements observed in the borehole inclinometer, as well as the accelerations recorded by the accelerometer, show that the Bramley Drive site is in a state of constant flux. This study was established to identify and characterise the factors that may be contributing to its dynamic state, by assessing potential trends and relationships between the data obtained by the recording instruments.

This chapter outlines attempts to characterise the observational data; concentrating on diurnal effects that cause ground movement at the site. As discussed previously in Chapter 3, changes in temperature, rainfall, solar insolation, tidal phases, and an underlying high frequency vibration were noted in the observations. Since these may be indicative of the factors that directly affect both the accelerometer and borehole inclinometer, they will be assessed separately below. The literature review (Chapter 2) has provided background information for each factor, as well as a brief overview of the Bramley Drive site stratigraphy and recent history in regards to ground failure, which is relevant to the interpretation of the data.

4.2 WAVE INDUCED PRESSURE VARIATIONS AND MICROSEISMS

Pressure variations caused by the passage of ocean waves may induce both primary and secondary microseisms (Chapter 2). These microseisms could potentially be the source of the observed high frequency vibration or "hum" within the one-second accelerometer data, and due to their typical periods of 3-300 seconds, they would be absent in the 10-minute averaged data. Longer period ocean waves, including ocean tides will be considered separately. Shorter period capillary and ultra-gravity waves will not be considered due to their extremely high frequency and negligible amplitude, which means that any pressure pulses generated would be too small to detect.

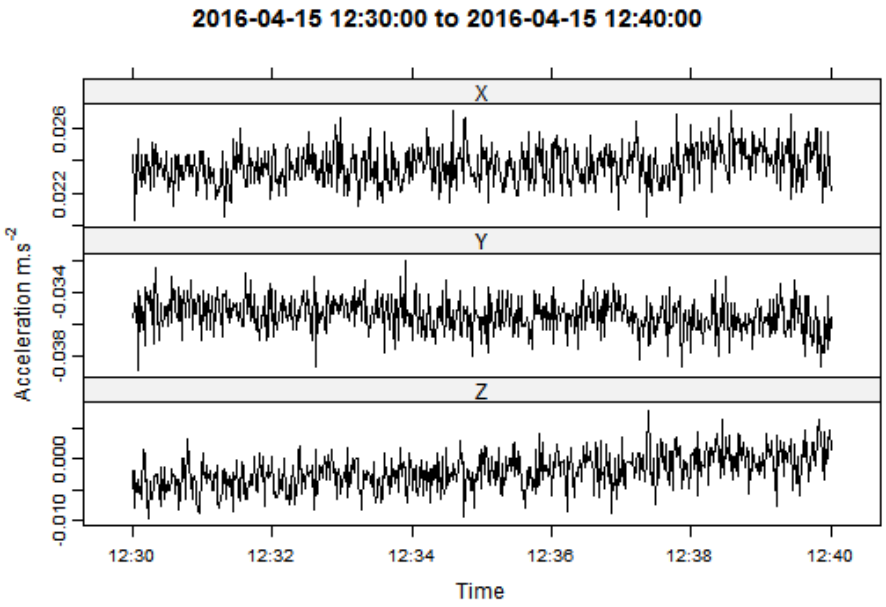

Figure 4.1: 10 minutes of one second data for the X-, Y- and Z-axes recorded by the onsite accelerometer on the 15th of April 2016.

Initially, a 10 minute window of one-second data from the 15th of April 2016 (Figure 4.1) were decomposed using simple Loess decomposition (STL) within the statistical software R (using RStudio© version 0.99.489), to separate the time series into three components (Cleveland *et al.*, 1990), which are labelled "seasonal", "trend" and "remainder" (Figure 4.1 & Figure 4.2). Essentially this allows the separation of the long period variations (trend) from the medium period (seasonal) and short period fluctuations (remainder).

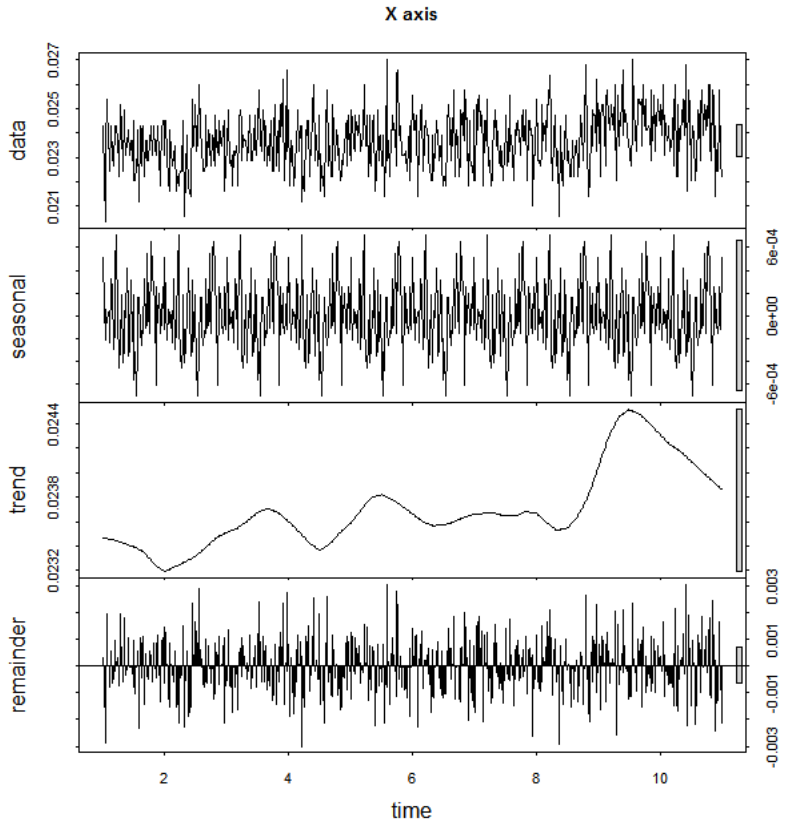

Figure 4.2: STL decomposition of X-axis, one-second data recorded over 10 minutes on the 15th of April 2016, beginning at 12:30 to separate seasonal, trend and remainder components.

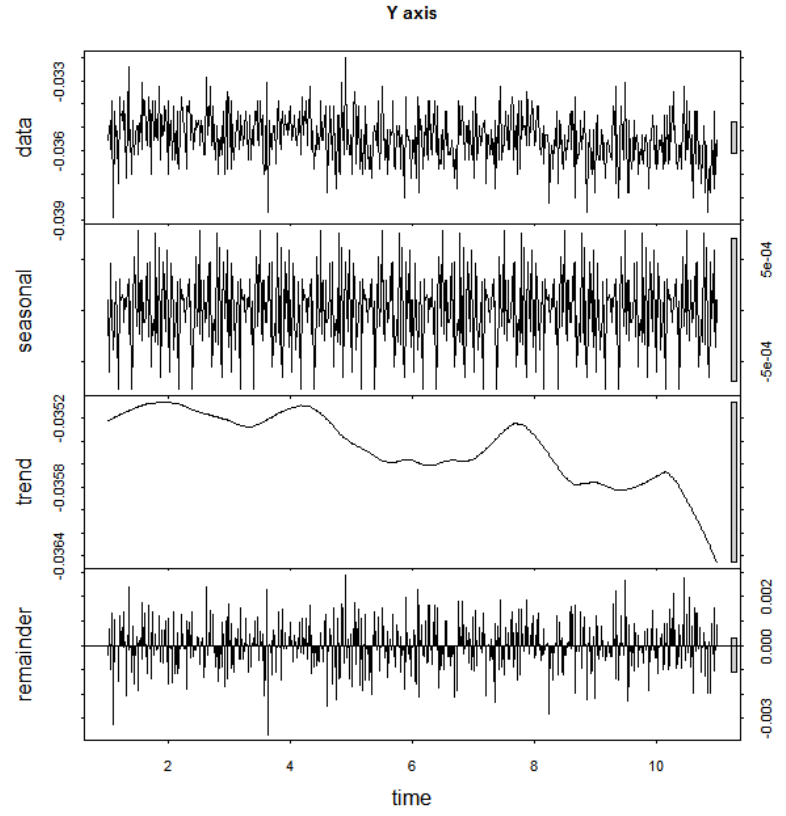

Figure 4.3: Decomposition of Y-axis, one-second data recorded over 10 minutes on the 15th of April 2016, beginning at 12:30 and using simple loess decomposition to separate seasonal, trend and remainder components.

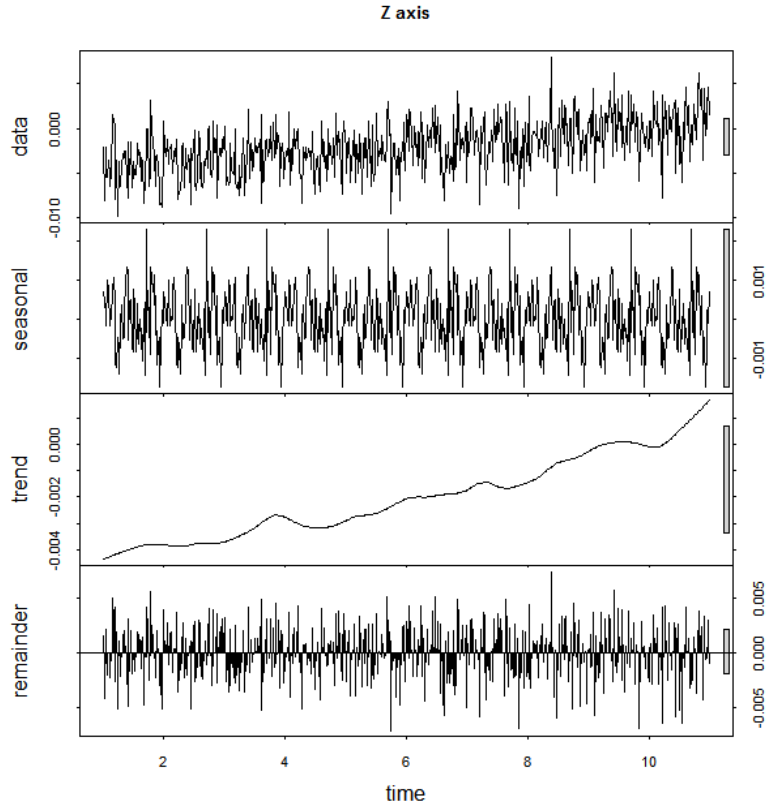

Figure 4.4: Decomposition of Z-axis, one-second data recorded over 10 minutes on the 15th of April 2016, beginning at 12:30 and using simple loess decomposition to separate seasonal, trend and remainder components.

STL was chosen as the first step for analysing the one-second data due to its rapid compute time and basic visual layout of the results. As shown in Figure 4.3 and Figure 4.4 cyclical behaviour is observed within all three components, indicating that multiple waves contribute to the signal in all X, Y and Z directions. The appearance of the seasonal component is similar to that of typical measurements of "groupy" ocean waves that have a significant infragravity component (known as surf beat). However, while the seasonal component shows the most consistent pattern of fluctuations, the scale of these is smaller than the fluctuations in the trend and remainder components.

The energy distribution with frequency can be used to diagnose either primary or secondary microseisms, as well as longer infragravity waves. Hence spectral density estimation (SDE) with smoothing was undertaken within the statistical software R (Figure 4.5). SDE estimates the power spectral density of a random signal over time, identifying peaks in the spectrum that help to define any periodicities in the data. Major peaks observed in the X-axis are at 0.05, 0.15-0.24 and 0.4 Hz, which correspond to 30, 90-150 and 240 second spikes that are well within the range of wave periods for infragravity waves (30-300 s). The Y-axis shows similar peaks; primarily at 0.25 and 0.4 Hz (90 and 240 s) suggesting that infragravity waves induced microseisms influence

acceleration in all directions on site. As for the Z-axis (elevation), peaks are observed at 0.15, 0.25, 0.37 and 0.45 Hz which indicates that acceleration in the Z-axis is also affected by surf beat associated with ocean waves breaking offshore of Matakana Island.

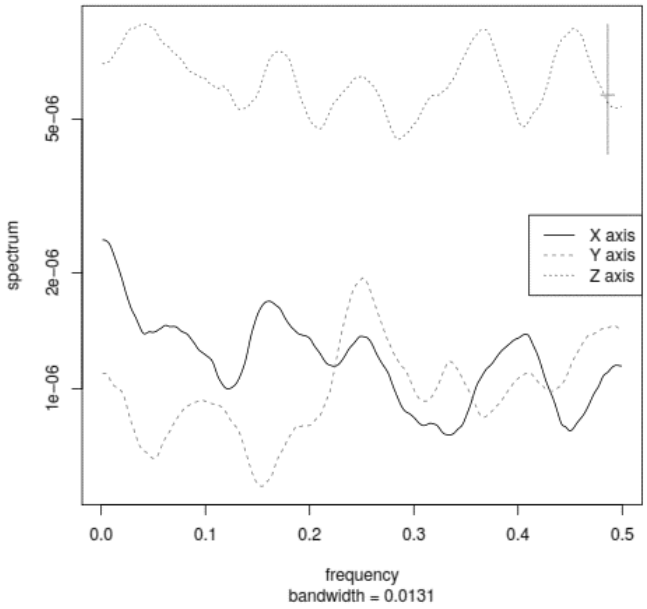

Figure 4.5: Power spectral density plot of one-second data recorded over 10 minutes on the 15th of April 2016, beginning at 12:30 in X, Y and Z directions.

To examine if higher frequency waves (wind-generated gravity waves or surf) were also inducing accelerations at the Bramley Drive site, a shorter subsample of 2 minutes' duration was analysed (Figure 4.6).

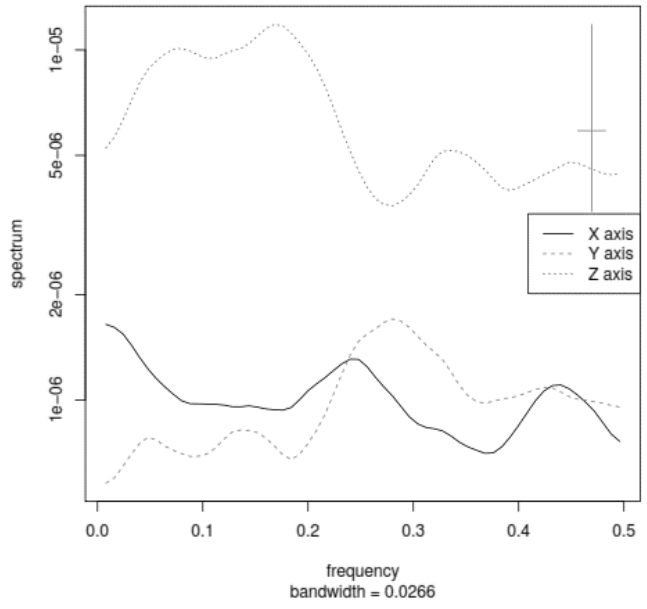

Figure 4.6: Power spectral density plot of one second data recorded over 2 minutes on the 15th of April 2016, beginning at 12:30 in X, Y and Z directions.

Large peaks were detected in the Z-axis accelerations between 0.05 and 0.2 Hz that correspond to wave periods of 6 to 24 seconds, which are expected wave periods for wind-generated gravity waves. Hence, it is evident that primary microseisms due to gravity and infragravity waves are being recorded by the accelerometer, while secondary microseisms are not. A reason why the secondary microseisms are not recorded is that they are at a higher frequency, and the 1 Hz sampling frequency may not be fast enough to detect them.

In order to have more direct control on how the data were analysed, singular spectrum analysis (SSA) was undertaken using the RSSA package created for the statistical software R. One advantage of SSA over traditional time series analysis methods like STL is that SSA can be applied to unconventional time series such as signal processing, since it does not require a reasonably deduced model for trend, period values and number of periodicities (Golyandina & Korobeynikov, 2014). Instead the RSSA package allows the visualisation of a range of components within the data (Figure 4.7-left), and provides tools to select the components that provide significant contributions to the observed variation in the signal (Figure 4.7-right).

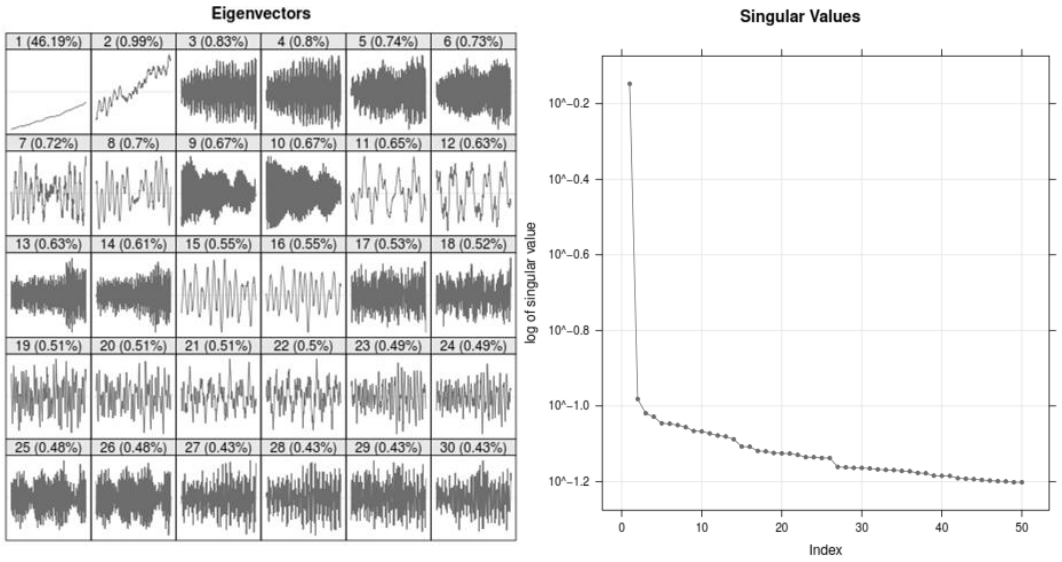

Figure 4.7: Visual detail of applied Eigenvectors (left) as well as the singular values plot used to compile Eigenvectors into groups (right)

Only results for the Z-axis are shown as the variability for both X- and Y-axes were dominated (>99%) by the trend over the 10 minutes sampled (Appendix 1). Microseisms shown in Figure 4.8 were compiled by grouping together eigenvectors that are either side of inflection points within the singular values plot (Figure 4.7-right).

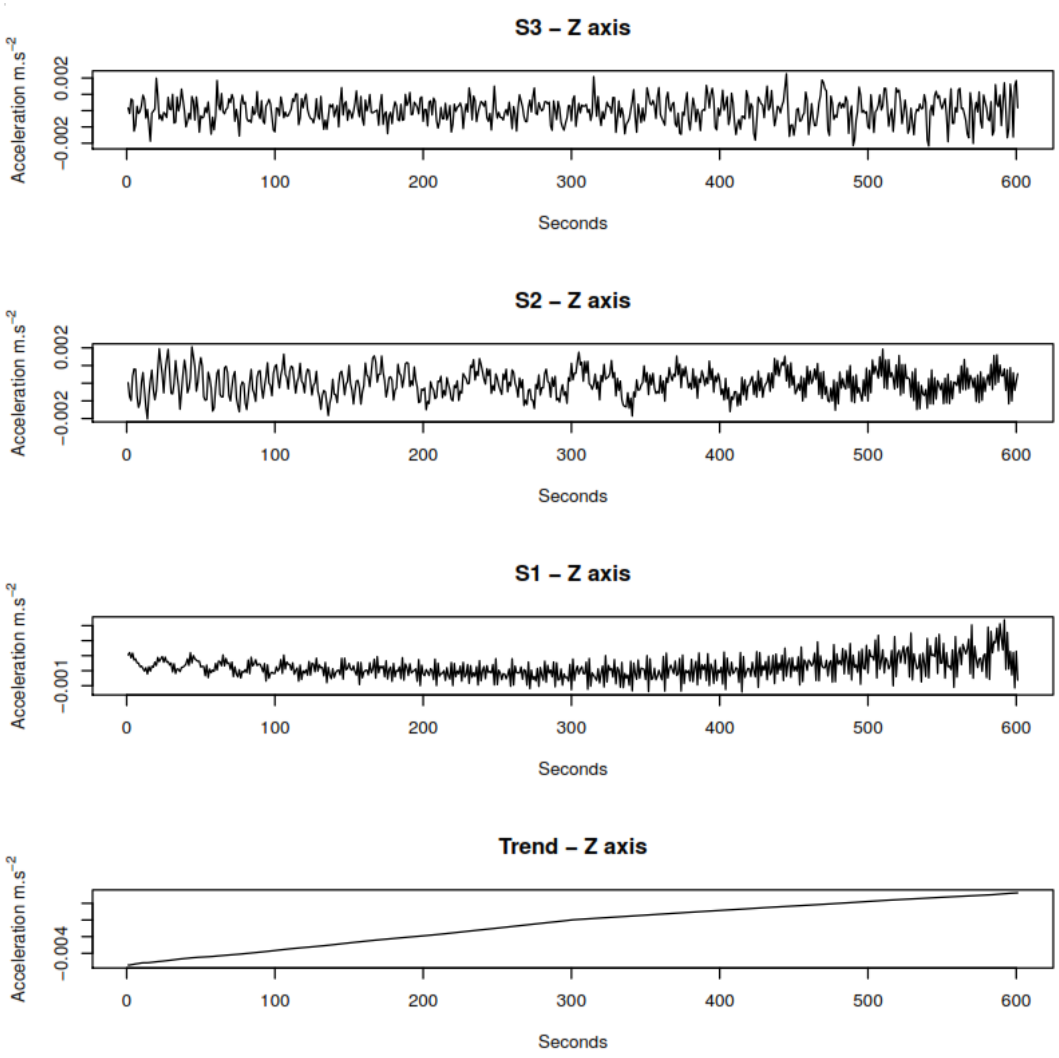

Figure 4.8: Singular Spectrum Analysis of one-second data recorded over 10 minutes on the 15th of April 2016, beginning at 12:30 in X, Y and Z directions.

As expected due to the STL analysis, the trend over 10 minutes dominates the signal components, accounting for almost 50% of the variance. Due to the large amount of noise using the one-second data, 29 additional eigenvectors were calculated (Figure 4.7-left). These were combined into three main groups, S1, S2 and S3 (Figure 4.8), which include 5%, 6% and 6% of the total recorded data respectively.

S1 shows possible short period wind/swell waves (<30 s), with changes in acceleration over time due to the heterogeneity of wind waves. Based on measurements obtained offshore from the Katikati harbour entrance at the north-western end of Matakana Island, the average swell wave periods were between 10-11 s, with measured periods ranging from 2-13 s (Macky *et al.*, 1995). Therefore, it is inferred that S1 represents primary microseisms from waves breaking on the open ocean coast of Matakana Island. S2 shows possible infragravity waves as identified by the SDE analysis, with wave periods of approximately 90 s, while S3 is predominately noise.

To assess the displacement caused by these microseisms, a double integration within the frequency space was undertaken on the same 10-minute block of data (Appendix 1). However, results were unrealistic with displacements ranging from 0.2 m to >0.8 m for all axes. Calculating displacement by double integration accumulates the errors in the measurement, and it amplifies the displacement. With the amount of high frequency noise observed in the accelerometer (e.g. component S3 in Figure 4.8), as well as the tilt bias of the instrument, the double integration results were considered to be inaccurate or unreliable for displacement measurement. Hence, no further action was made to calculate displacement from the ongoing one-second accelerometer data.

All signs point to microseisms occurring at Omokoroa Peninsula, albeit their contribution to diurnal movements at the site are minimal being at least an order of magnitude smaller than the other factors driving longer period changes. As with previously published work (Adams *et al.*, 2005) microseisms are primarily considered to be a factor that may propagate crack growth or reduce the strength of areas within a coastal cliff, but not a cause of initial cliff instability. What is different at Omokoroa compared to previously published work on rocky cliffs (Adams *et al.*, 2005; Young *et al.*, 2012) is that the primary or single frequency microseisms appeared to be predominant, instead of secondary, double frequency microseisms. Primary microseisms are expected to dissipate faster with greater distance from the coast, than secondary microseisms. Since the measurement site on Omokoroa Peninsula is approximately 5-6 km from the coast, as well as being separated from the coast by the Tauranga Harbour, it was expected that the primary microseisms would be weaker as previously recorded by Bossolasco *et al.* (1973) (Young *et al.*, 2012). It is possible that the noise component (S3) contains secondary microseisms that cannot be resolved by the 1 Hz sampling rate.

4.2.1 Limitations

There are several limitations to the interpretation of possible microseisms using the accelerometer observations. To confirm the hypothesis that microseisms are present at the Omokoroa Peninsula site, additional data are required to define the wave conditions at the same time as accelerations are recorded. This would require the deployment of a wave buoy off the Matakana Island coast to record the local gravity and infragravity waves. Also, an additional accelerometer at the seaward coast of Matakana Island would be useful to compare with the existing accelerometer. In particular it would be used to determine if the spectral density distributions are

consistent between the sites, or if the primary microseisms decrease in amplitude over the 6-7 km distance between them.

The second factor that greatly affects the existing accelerometer when interpreting microseisms is its placement at ground level, where it is directly influenced by changing temperature, insolation, and local surface vibrations. These factors, primarily temperature, appear to greatly control the overall trend of the accelerometer over time, contributing at least half to over 99% of the ground acceleration occurring at any point at this site (Section 4.2). Installing another accelerometer deep beneath the surface would return more reliable results, far away from surface processes while not affecting microseisms recording since these faint tremors, both primary and secondary, travel throughout the whole soil profile.

4.2.2 Summary

Cyclical behaviour was observed within all three components of the on-site accelerometer. While the trend of each component dominated its respective signal, the use of singular spectrum analysis (SSA) for the Z-axis component shows the appearance of possible short period wind/swell waves (<30 s) that could represent primary microseisms caused by waves breaking on the open coast of Matakana Island. Infragravity waves were also inferred by identifying wave periods of approximately 90 s.

Section 4.2 states the trend inherent in both X- and Y-axes is responsible for over 99 % of recorded variability and almost 50% for the Z-axis. While many reports have suggested the significance of primary microseisms propagating crack growth in rocky cliffs, Omokoroa's position within a sheltered harbour and its non-brittle geology would suggest contribution of these microseisms to diurnal ground displacement at the Bramley Drive site is minimal.

4.3 SOLID EARTH TIDES

Following Moon *et al.* (2015a) who suggested fluctuations within the borehole inclinometer may be a result of solid Earth tides, the response of the borehole to this force was investigated.

To understand the complexity involved in Earth tides, the number of separate contributing factors, or components must be appreciated. Doodson (1921) built upon Darwin's "Darwinian Constituents", that were first used for the harmonic

development of the tide generating potential (TGP), with a set of 377 tidal constituents that are still used in TGP models today. Subsequently, many more constituents have been proposed and catalogued resulting in thousands of additional tidal wave harmonics (Wilhelm *et al.*, 1997), most of which have very small amplitudes. Of the tidal constituents, those associated with the semi-diurnal and diurnal effects of the pull of both the Sun and Moon on Earth are most obvious. These are associated with changes to the distance of the Sun and Moon to Earth, the Moon's declination relative to the Earth's equator, the Moon's location with its monthly orbit, and the Earth's location within its yearly orbit of the Sun. Forecasting solid Earth tides at a specific location is now possible due to computer models, which usually incorporate at least the thirty largest constituents to calculate a realistic tidal curve.

These main tidal constituents will be briefly explained and related to the Omokoroa Peninsula as well as the borehole inclinometer measurements recorded on the 15th of April and 14-15th of November 2016.

4.3.1 Earth's inclination and orbit

Earth's orbit around the Sun is not circular, but is in fact elliptical. This means that throughout one full orbit of the Sun (1 sidereal year – 365.26 days), the Earth's distance from the Sun varies by around 5 million kilometres: with the perihelion (closest point to the Sun) occurring in early January; and the aphelion (furthest point from the Sun) in early July, very close to each of the year's solstices (Figure 4.9). One may assume this is what causes the separation of the seasons, however in regards to changing the TGP this variability is minimal given that the average distance between the Earth and the Sun is about 149.6 million kilometres (~3.3% annual variation). What's much more important with regard to the seasons and TGP is Earth's axial tilt and the relative orientation of the polar latitudes to the Sun.

As Omokoroa, New Zealand is situated in the Southern Hemisphere, the following discussion of seasons, solstices and equinoxes will be from the Southern Hemisphere perspective. Figure 4.9 illustrates how the Southern Hemisphere is affected by the tilted Earth and its orbit around the Sun, where the winter solstice occurs when the Sun is directly above the Tropic of Cancer located in the Northern Hemisphere, and the summer solstice occurs when the Sun is directly above the Tropic of Capricorn in the Southern Hemisphere. These, as well as the autumn and spring equinoxes that occur when the Sun is directly above the equator give Earth its four seasons and is the Sun's greatest contribution to its TGP.

For solid Earth tides the maximum TGP caused by the Sun occurs at different times throughout the day due to Earth's 23.4˚ tilt, with the maximum pull during the day at the summer solstice and maximum pull during the night at the winter solstice. Autumn and spring equinoxes thus have a smaller maximum TGP than the rest of the Earth's orbit, but both have a similar TGP as the Sun is directly above the equator in both instances.

Therefore, the Sun's contribution towards TGP at Omokoroa Peninsula, while much less than the Moon's effect, usually determines when the largest vertical displacement will occur during the day. For New Zealand the maximum TGP occurs in the afternoon or Earth at night when New Zealand is aligned with the Sun-Earth axis; and the Sun's lowest TGP occurring in the mornings and evenings when New Zealand is perpendicular to the Sun-Earth axis. This is helpful in predicting at what times of day testing would be most suitable.

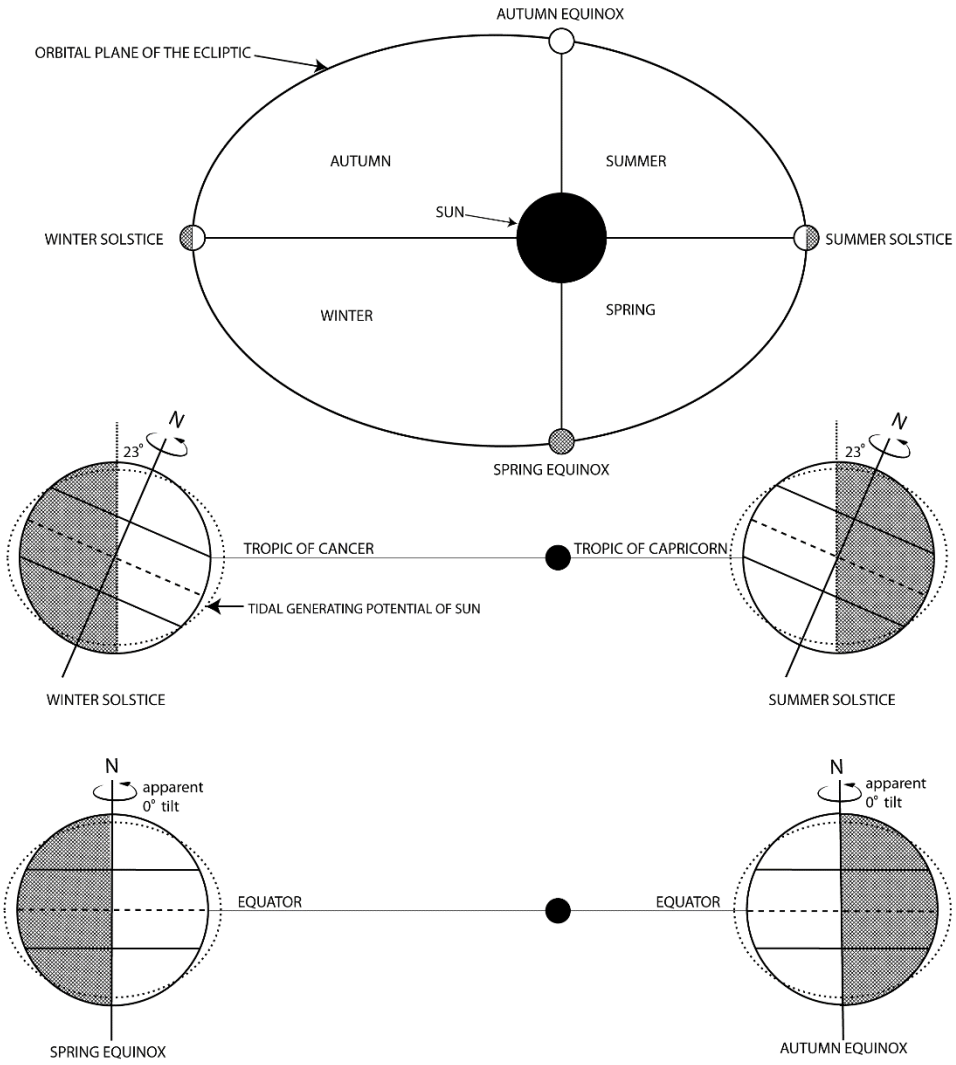

Figure 4.9: Diagram of Earth's ecliptic orbit around the Sun, along with its accompanying winter/summer solstices and spring/winter equinoxes. Dashed line shows exaggerated tidal generating potential. Note apparent tilt of Earth during the equinoxes is defined as if looking at the Earth perpendicular to the Sun, and is only a visual representation of the Sun being directly over the equator at these times. The named seasons are relevant to the southern hemisphere only.

4.3.2 The Moon's position and Earth's rotation

As the Moon's TGP (1.14 μm s^{-2}) accounts for over twice the tidal acceleration of the Sun (0.51 μm s^{-2}) (Agnew, 2015) its effect on Earth is much more pronounced. It is common knowledge that the Moon is the primary cause of the ocean tides on Earth, with the Sun contributing to the tides, however the explanation of how it works is often incorrect.

A common misconception is that the Moon orbits Earth, while the Earth stays in place rotating (ignoring the movement of the Earth relative to the Sun). However, both Earth and the Moon orbit each other around their barycenter, or the centre of mass of the two bodies, which is located approximately 4 600 km from the centre of the

Earth (mean Earth radius is ~6 378 km). Considering the mass of Earth is 81 times larger than the Moon (Pitjeva & Standish, 2009), the barycenter is located within Earth and so the Earth appears to be "wobbling" instead following a discernible orbit around the barycenter. This is important for tides as it is both the gravitational attraction of the Moon as well as the orbit of Earth around its barycenter that provides centripetal force maintains its orbital velocity.

Relating this to TGP, the Moon's gravitational attraction is strongest at the closest (nadir) side of Earth, and its attraction is at its least on the opposite (zenith) side due to the increased distance. The TGP attraction occurs throughout the Earth, meaning the elastic interior of the Earth stretches towards the Moon by varying amounts, depending on distance. Therefore, the TGP effectively drags a large part of the Earth towards the Moon, with the rest decreasing in displacement until reaching the side of Earth opposite the Moon, effectively leaving it behind and giving it an apparent negative force away from the Moon as the Moon's gravitational pull is much less than at the Earth's center (Figure 4.10). However, centripetal acceleration associated with rotation around the barycenter has the opposite effect, causing the Earth to bulge outwards on the zenith side.

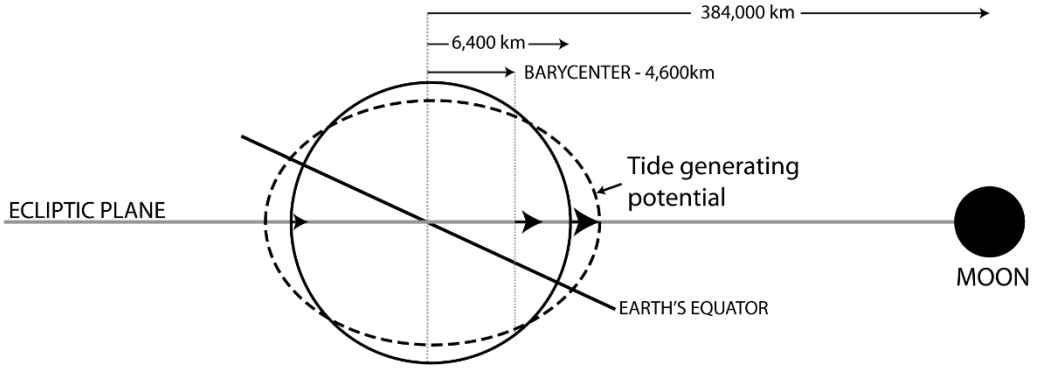

Figure 4.10: Diagram of the tide generating potential exerted on Earth by the Moon (dashed line). Arrow size indicates tidal pull.

The combined tidal forcing can be represented using force (acceleration) vectors for the Earth which are caused by the pull of the Moon (Agnew, 2015). Figure 4.11 shows the net effect on the shape of the Earth due to tidal forcing, with the sides perpendicular to the Earth-Moon axis being compressed inwards towards the centre of Earth, and the equatorial regions radiating out, giving an exaggerated elliptical shape of the Earth and oceans at "high tide".

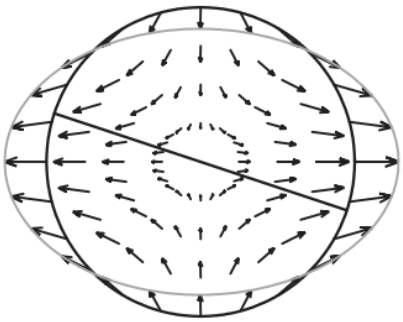

Figure 4.11: Tidal force vectors caused by the Moon on Earth's basic spherical shape with arrow size indicating magnitude. Grey line shows the exaggerated pull and compression of the solid Earth. Black line is the equator, so this figure corresponds to the average declination of the Moon (in line with the plane of the ecliptic) (Agnew, 2015).

4.3.3 Moon declination and distance

Just like Earth's ecliptic orbit around the Sun, the Moon follows an offset ecliptic orbit around the Earth, with a perigee and apogee every full rotation. This elliptical orbit also deviates slightly from year to year, so the distance to the Moon at perigee Moon-Earth each month, can also be much closer or further away depending on what year. In addition, when syzygy (full or new Moon) coincide with perigee, the Moon's TGP is at a maximum. The full Moon cycle is the time taken between consecutive full Moon's at perigee and takes about 411.8 days, so the maximum TGP occurs every 205.9 days. Other variations in the orbit result in longer period fluctuations in the perigee distance every 18 and 55 full Moon cycles (approximately every 20 and 62 years), which also affect the TGP.

This was important for the full Moon on the 14-15th of November 2016 when several cycles reached their minima, and this will be expanded upon below. The Moon, while orbiting Earth also is slightly offset from the orbital plane of the ecliptic (Earth's orbital plane with respect to the Sun) meaning that the declination of the Moon changes from a maximum positive angular distance to maximum negative angular distance from Earth's equatorial plane (Figure 4.12) over one sidereal month (27.32 days). While the difference is minor, this means the Moon will be closer to the latitude of the Omokoroa Peninsula once a month, contributing to the total TGP when coupled with Moon and Sun location at certain times throughout the sidereal month.

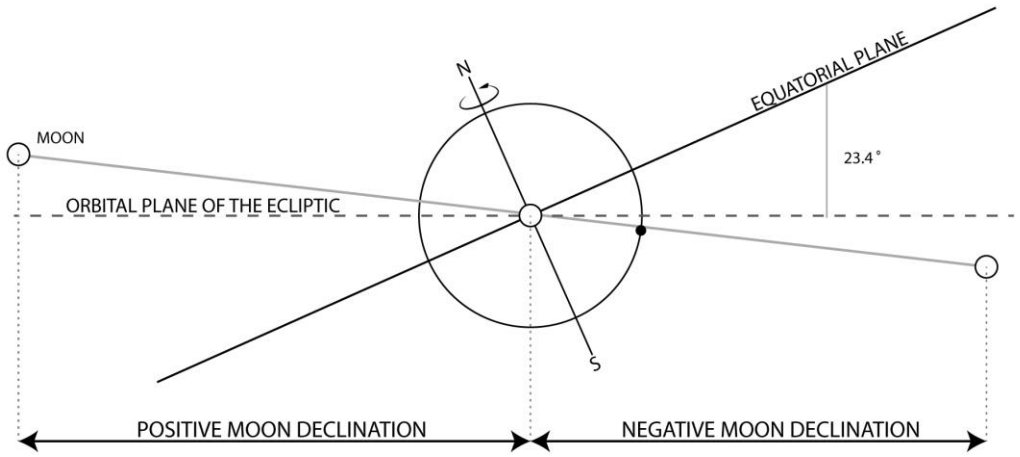

Figure 4.12: The Moons orbit over a two-week period, moving from a positive declination to neutral position near the equator, and finishing at a maximum negative declination. Black circle is Omokoroa Peninsula position.

The Moon's maximum declination over one sidereal month also varies over an 18.6-year cycle, deviating from $\pm 29^{\circ}$ at the major lunar standstill, to $\pm 18^{\circ}$ at the minor lunar standstill (Figure 4.13). The changing declination is one of the main factors affecting the timing of lunar Earth eclipses when the Moon's "new Moon" phase occurs as the Moon passes the plane of the ecliptic, situating itself between the Sun and Earth. The declination affects the TGP at Omokoroa in the same way as the Earth's inclined axis of rotation does the Sun, albeit over a longer period, as discussed above.

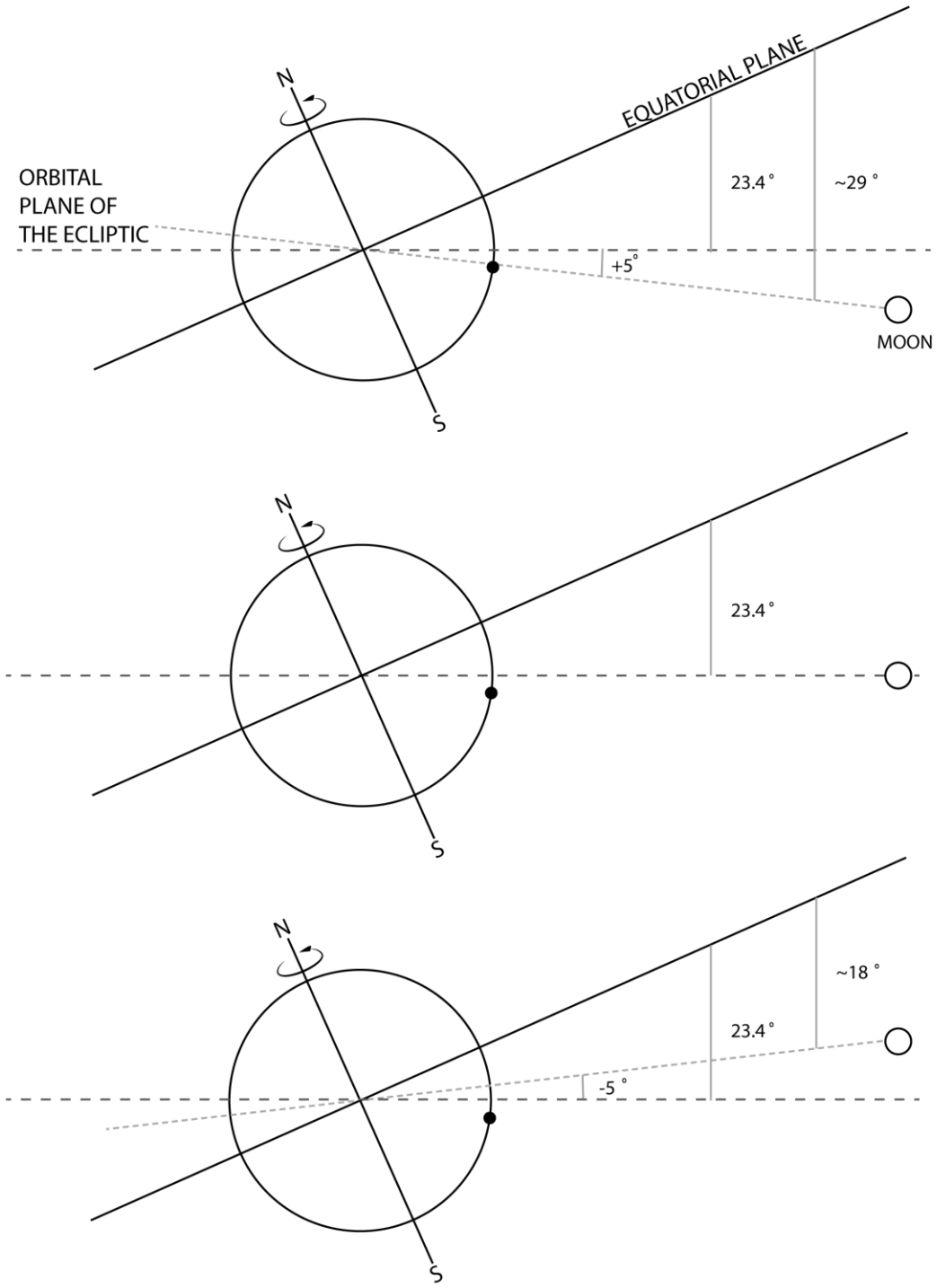

Figure 4.13: The variation of the Moon's declination from the orbital plane of the ecliptic every 18.6 years resulting in the Moon's declination varying from 18-29 ˚ over this period. The black circle corresponds to the latitude of the Omokoroa Peninsula.

4.3.4 Lunar phases

The position of the Moon is in relation to the Sun will also dictate the TGP exerted at Omokoroa Peninsula. As the Moon completes a full orbit around Earth, the Moon will have a different appearance in the sky due to sunlight reflecting off it. Eight primary phases are used to describe the Moon's location (new, waning/waxing

crescent, first and third quarter, waning/waxing gibbous and full) as the Moon orbits anti-clockwise (Figure 4.14). When the Moon is at either its new of full phase, combined TGP will be at its maximum as the Moon is in line with both the Sun and Earth (syzygy) producing spring ocean tides with the largest tidal ranges. Whereas at first and third quarter the Moon is perpendicular to the Earth-Sun axis (quadrature) producing Sun-Moon neap ocean tides with the smallest tidal ranges.

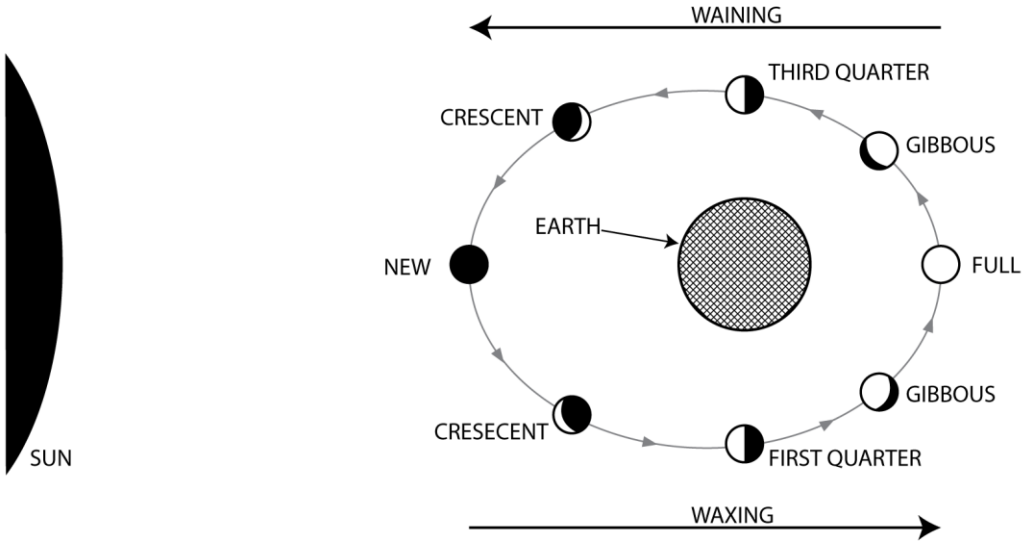

Figure 4.14: Diagram presenting all 8 primary Moon phases in relation to Earth and the Sun.

All of these components combine to form semi-diurnal fluctuations in TGP at any site on Earth, specifically the Omokoroa Peninsula for this thesis.

4.4 EARTH TIDE OBSERVATIONS AT OMOKOROA

Two datasets recording at least 12 hours of continuous, half-hourly measurements of the borehole inclinometer were obtained on: the 15th of April 2016; and the 14-15th of November 2016. CALSKY™ (Barmettler, 2016) was used to predict the vertical and horizontal displacements generated by Earth tides at Omokoroa, and these will be analysed by comparing the predicted Earth tide to measurements.

4.4.1 15th of April 2016

Figure 4.15 shows where the Earth was in relation to its yearly orbit of the Sun on the 15th of April 2016. The autumn equinox occurred on the 20th of March 2016, where Omokoroa's distance from the ecliptic plane would be the same throughout the Earth's daily rotation. By the 15th of April, the Earth was approximately one third of its way to the winter solstice (20/21 June 2016), meaning Omokoroa was well on its

way to reaching the point at which it reaches its maximum distance from the ecliptic plane in the day time and its minimum at night (winter solstice).

This is most apparent in Figure 4.16, which displays predicted vertical displacement, Moon declination and Moon distance for the first 6 months of 2016. Semi-diurnal vertical displacement clearly shows how the difference between consecutive tidal maxima decreases as it trends from the summer solstice towards the autumn equinox. The equinox (mid-March to mid-April) corresponds to similar vertical displacements twice daily, while January and May show a prominent high magnitude vertical displacement once daily, with a secondary semi diurnal spike, caused by Omokoroa's increasing distance from the ecliptic plane. Moon phases also show the expected relationship with higher vertical displacement at new or full Moon phases. The Moon's declination and distance do influence vertical displacement as well, although to a lesser extent.

The side view in Figure 4.15 shows that the TGP reached its maximum at midnight, with minimums in the early morning and afternoon at approximately 06:00 and 18:00 respectively. With regards to the Moon's placement, it was in its first quarter phase, meaning it was located perpendicular to the Sun, and exerted its maximum TGP at approximately 07:00-07:30 and 19:00-19:30 when Omokoroa lay beneath the Moon (nadir) or completely opposite it (zenith).

The predicted Earth tide displacements at Omokoroa are also shown in Figure 4.15, and once the basic processes that contribute to the Earth tides are known, the predicted patterns begin to make sense. First looking at the vertical displacement, starting at 06:00 on the 14th of April, displacement is negative until reaching its minimum at approximately 00:00 on the 15th of April. This minimum is when the TGP of the Moon and Sun are at their lowest, the vertical displacement then begins to rise reaching its peak at around 07:00-07:30, which is when the Moon is in the zenith position relative to Omokoroa, before falling to a minimum at 15:00. The deviation of these times to the expected approximately 6-hour period between high and low ocean tides is due to the Earth's tilt. This effect is most apparent at 15:00: only, considering the Moon's TGP the minimum should be at 13:00 when Omokoroa is perpendicular with the Earth-Moon axis (Figure 4.15). However, at that time the Sun's TGP is almost at one of its semi-diurnal maxima, negating part of the Moon's TGP and delaying its effect on Earth until the Earth rotates out of the Sun's direct pull, where it becomes

weaker due to the reduced TGP in the southern hemisphere during the day-time when nearing the winter solstice.

As for the predicted horizontal displacement, which is the factor most affecting the inclinometer measurements, it is necessary to consider strain, which is the response of Earth in this case to an applied stress due to the TGP. Earth is under maximum stress when either arriving at or leaving the maximum or minimum tidal force caused primarily by the Moon, and secondly by the Sun. On the 15th of April at 01:00 the horizontal displacement was zero. This coincided with the maximum TGP from the Sun (low stress) and minimum TGP from the Moon (low stress), resulting in no strain at Omokoroa at that time.

When the Earth rotates towards the maximum TGP from the Moon at ~07:30, horizontal strain begins to increase, causing approximately 3 cm of predicted eastward displacement (Figure 4.17) as Omokoroa is pulled towards the stronger tidal forces faster than the Earth rotates. Once there, the horizontal displacement plateaus as it has reached a "low stress" environment, it however does not return to zero as now stress caused by the Sun exerts additional strain. As the Earth rotates away from the Moon's strong tidal forces, horizontal strain begins to increase, this time in a western direction as the solid Earth due to tidal friction.

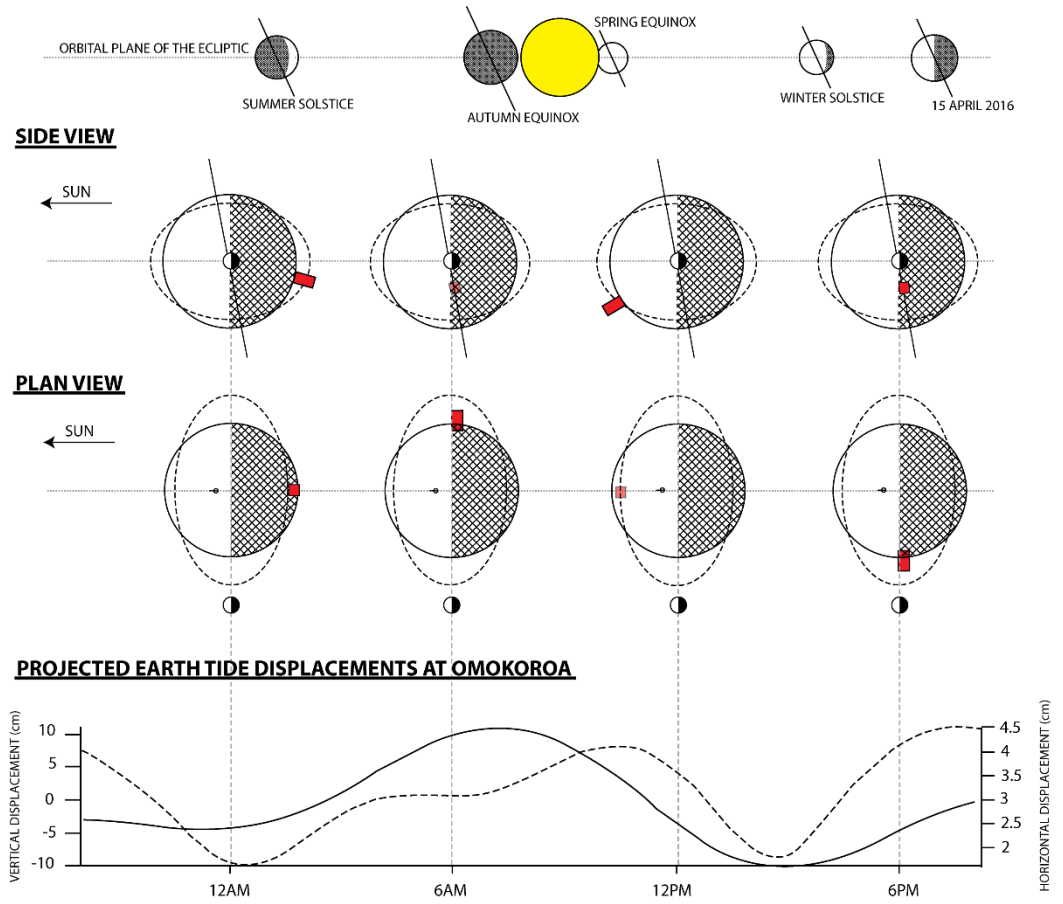

Figure 4.15: Sketch of Sun, Moon and Earth locations on the 15th of April 2016. Earth is in between the autumn equinox and winter solstice, as well as the Moon being in a first quarter phase. Note Moon location perpendicular to the Sun, as well as Earth's tilt leaning towards the Sun indicating the southern hemisphere moving into winter. Red cube is the approximate location of Omokoroa Peninsula, with its shape indicating vertical displacement causes by Sun and Moon TGP. Dashed lines for side and plan views show exaggerated tidal pull from the Sun (side view) and Moon (plan view). Predicted vertical and horizontal (dashed line) Earth tide displacements at Omokoroa generated by CALSKY™.

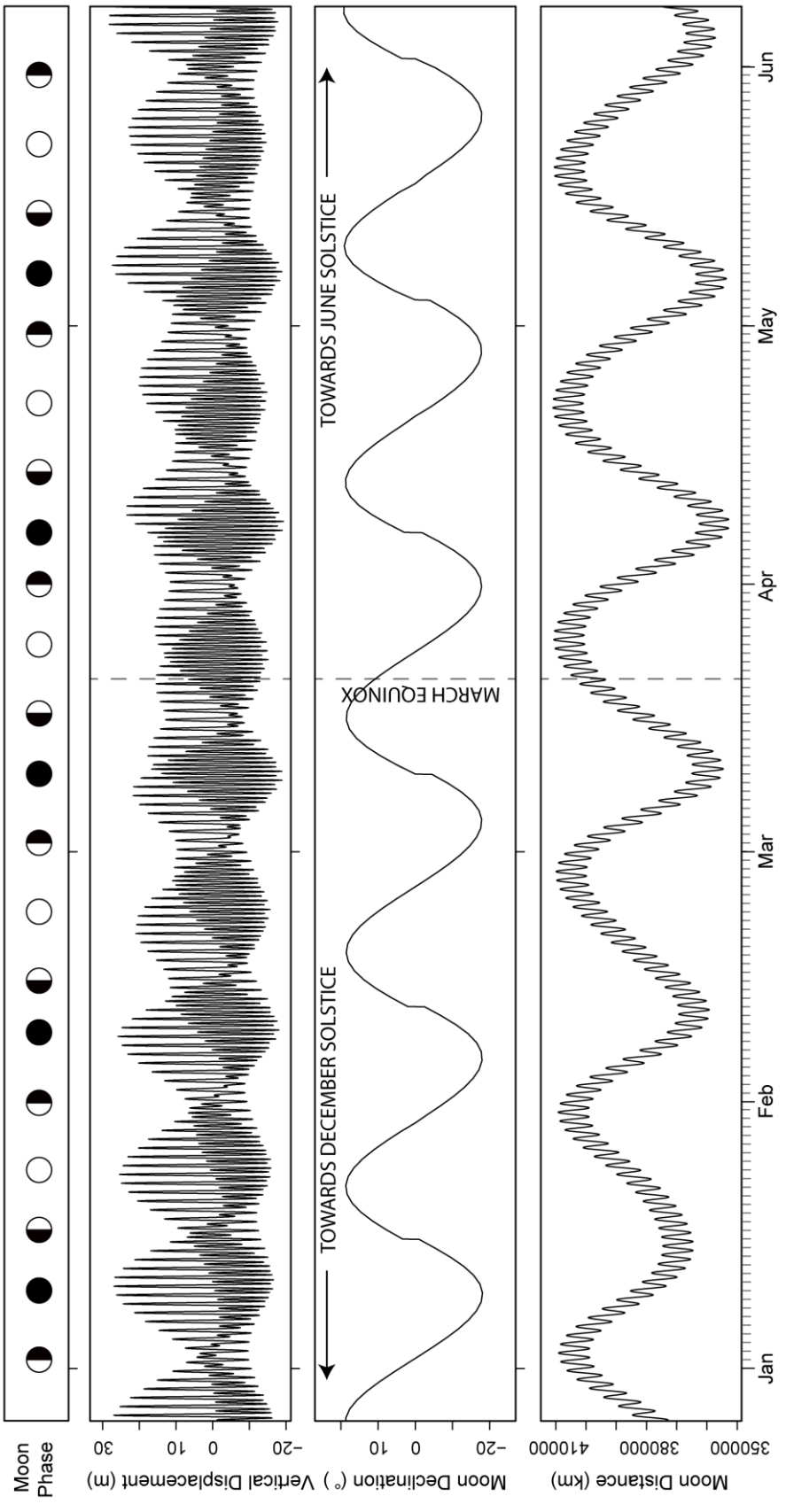

Figure 4.16: Predicted Moon phase, vertical displacement, Moon declination and Moon distance from Omokoroa Peninsula. Note the increasing vertical displacement near the solstices as well as the effect of the Moon's monthly declination and elliptical orbit of Earth on the distance to the Moon. Data generated by CALSKY™

The Earth tide induced semi-diurnal displacement is shown in Figure 4.17, where the total movement predicted for Omokoroa is plotted. All east-west displacement is caused by Omokoroa either being pulled eastwards or westwards by the maximum TGP of the Moon (primarily). The north-south displacement is dependent on the combined TGP of both the Sun and Moon, as well as the location of Omokoroa relative to the ecliptic plane. For the 15th of April, when the Earth was heading towards the winter solstice, Omokoroa's distance from the ecliptic plane was much larger around mid-day than at night. This is reflected in the large southwards-directed lobe in Figure 4.17.

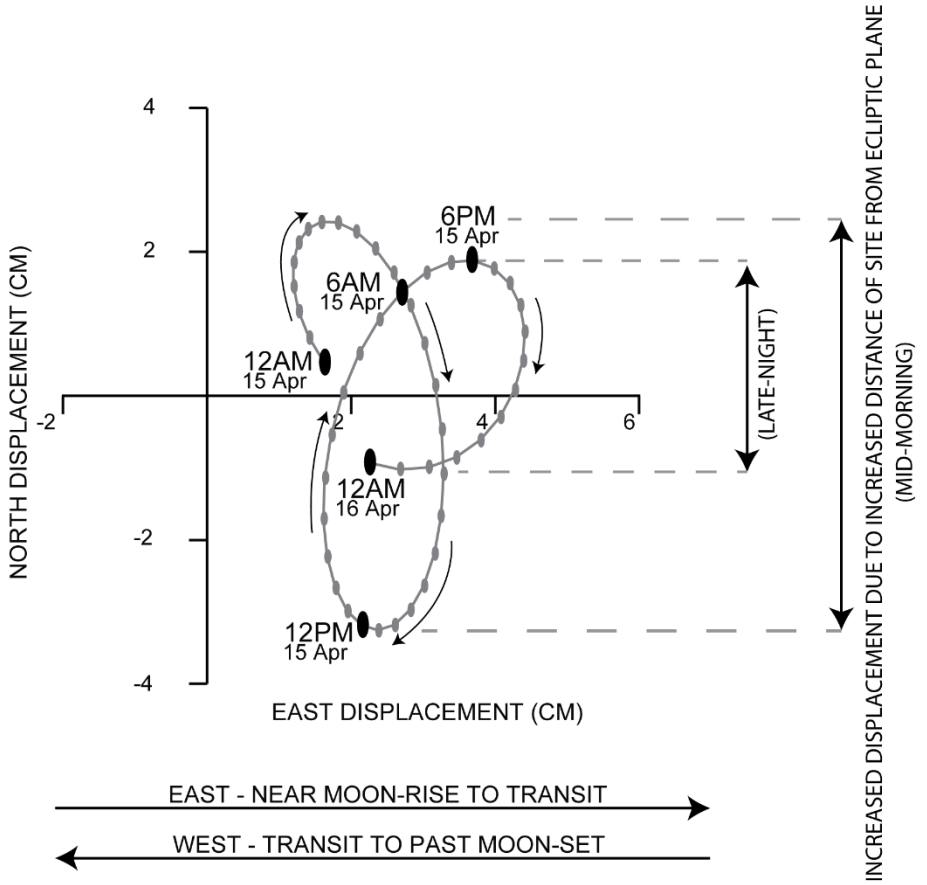

Figure 4.17: North-south, east-west plan view of project displacement at Omokoroa Peninsula beginning midnight on the 15th of April until midnight 16th of April.

The borehole inclinometer measurements were split into their north-south and east-west components, using the initial measurement recorded at 14:30 as the baseline measurement (Figure 4.18). The specific time of 14:30 was used as horizontal and vertical displacement were at a minimum, indicating a time where Omokoroa should have been exposed to the minimum horizontal stress. Therefore, it was expected that the horizontal displacements measured by the inclinometer would separate into those moving from one direction (east-west) to the other (west-east) as indicated by Figure

4.17. The CALSKY™ predicted north-south and east-west displacements are also shown in Figure 4.18.

What is most obvious is that the recorded displacement is 1-2 orders of magnitude smaller than the predicted displacement (Figure 4.18). This is due to multiple factors; the main one being that the borehole inclinometer records the borehole's shape and relative deviation from previous tests, not the exact location of the borehole itself. According to theoretical treatments of the Earth tide (Agnew, 2015), the entire 42 m length of the borehole should be displaced equally by the Earth tide. Hence, the tilt induced in a line between the top of the borehole at Earth's surface and the centre of the Earth should be too small to be detected by the inclinometer, which has a resolution of 1/25000˚ or $\pm 4 \times 10^{-5}$˚ compared to the theoretical tilt at Omokoroa of ± 100 nrad or $\pm 5.73 \times 10^{-6}$˚. However, if successive stratigraphic units respond differently to the Earth tide stress, the borehole will deform, and this deformation may be sufficient for the inclinometer to detect.

Considering the general shape of both the north-south and east-west components of the 15th of April recordings, they show similar trends throughout. When looking at the A-axis, note that the borehole inclinometer is offset approximately 40˚ from true north as it was aligned perpendicular with the most recent scarp regression and is likely the reason for sharp changes at when the east-west directions change (07:00-13:00, 13:00-07:00). Other similarities between recorded and predicted displacement in the north-south direction are the almost constant negative values, indicative of day-time when nearing the winter solstice as previously explained.

For the B-axis measurements, the observed deviation is primarily eastward consistent with the predicted east-west displacement; with the largest eastward deviation occurring in the morning and afternoon. Both the A- and B-axes also show increased ground movement towards the surface. Figure 4.18 shows how deviation at 31 m depth is much less than deviation at 21 m, which is less than 11 m and so forth, with the large deviations in the first few recordings in the morning being the most obvious. This increase in displacement is not predicted by Earth tide theory and must be caused by an additional factor that is affected by tidal forces, effectively amplifying ground movement.

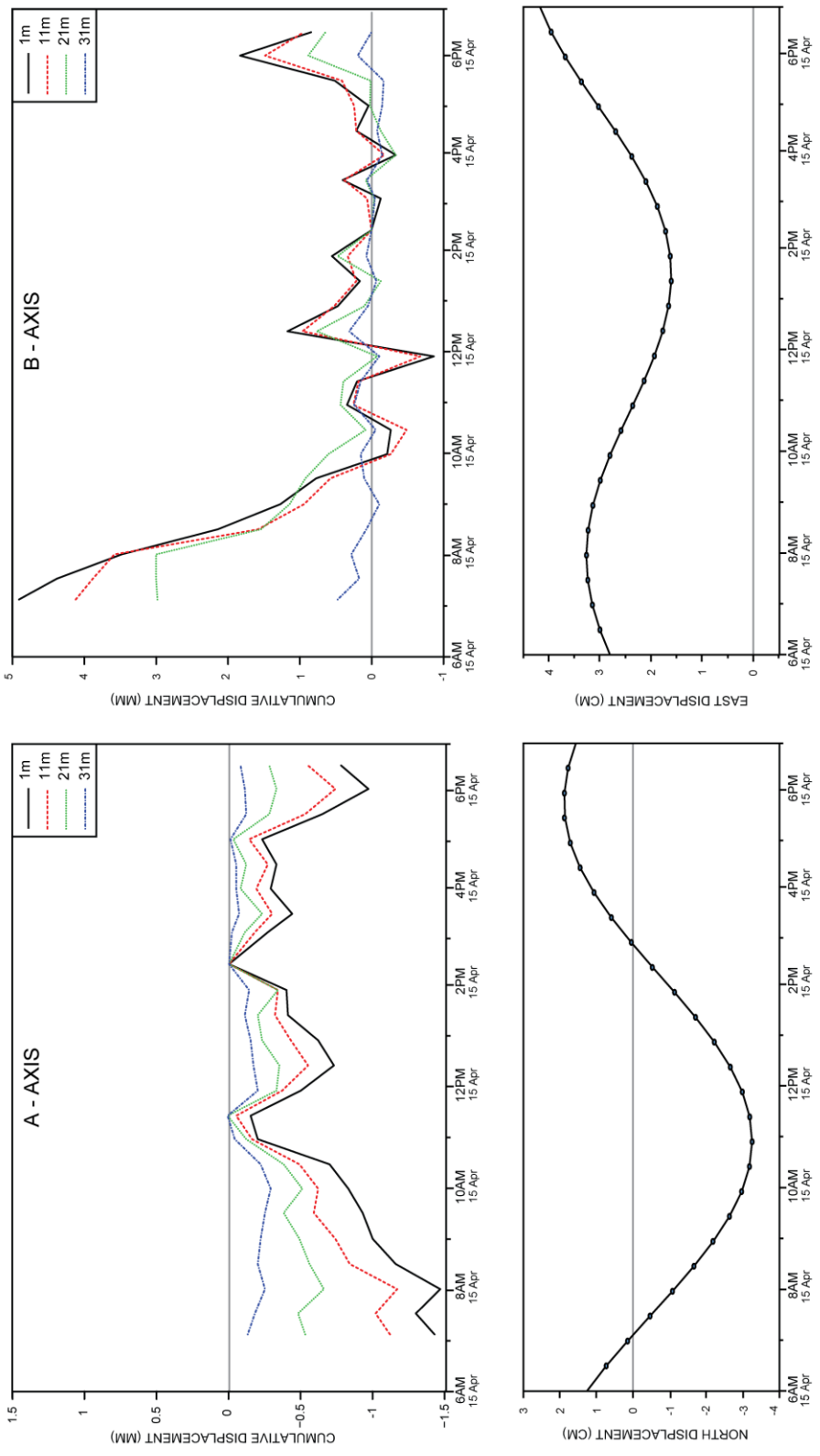

Figure 4.18: Plotted A- (north-south) and B- (east-west) axis displacements recorded from the on-site borehole inclinometer at different depths on the 15th of April (above). Predicted north-south, east-west displacements generated by CALSKY™ (below).

4.4.2 14-15th of November 2016

As with the 15th of April 2016, Figure 4.19 displays the Earth's position during the sampling period in relation to its yearly orbit of the Sun. Instead of the Earth trending towards the winter solstice, it is now close to the summer solstice (21st of December). This means that Omokoroa's distance to the ecliptic plane was at a minimum in the middle of the day, which was the opposite to what occurred on the 15th of April. The Moon was also in a "full Moon" phase, meaning it is in line with the Sun-Earth axis, while being on the opposite side of Earth from the Sun. At this time the Sun and Moon's TGP combine, in contrast to the Sun's contribution reducing total TGP on the 15th of April Moon-Sun-Moon. Further, the Moon was at perigee for the November measurements, significantly reducing the distance from Omokoroa to the Moon.

The full Moon observed at Omokoroa at midnight on the 15th of November was the largest of six supermoon's recorded in 2016. While the word "supermoon" is arbitrary, originating in modern astrology, it is widely used to define a time at which the Moon is especially close to Earth, with the 15th of November full Moon being the closest Earth since 1948. The Moon's declination in relation to the equatorial plane was also low, being approximately 10 ˚ (Figure 4.20 & Figure 4.21). Therefore, Omokoroa was close to the ecliptic plane, giving a larger TGP.

Hence, the predicted vertical and horizontal displacements at Omokoroa Peninsula, especially at mid-day, were the largest since 1948 and significantly larger than on the 15th April 2016 (Figure 4.28).The location of both the Moon and Sun in relation to Omokoroa is shown in Figure 4.19, indicating how the TGP of the Sun and Moon were combined, giving over 35 cm of predicted vertical displacement at local noon (13:00-14:00 NZST) on the 15th of November 2016. The same process explains the low maximum horizontal displacement at midnight on the 15th of April (when the Moon was directly above Omokoroa) as the Sun and Moon's TGP were much lower due to Omokoroa's greater distance to the ecliptic plane.

What does not seem to be affected by the semi-diurnal maximum peaks of the vertical displacement is the predicted horizontal displacement, with maximum horizontal displacement occurring near every vertical displacement peak. Its shape does differ slightly at mid-day, where small minimums occur, slightly decreasing horizontal displacement by a few centimetres. This is similar to the inflection point noted at approximately 07:00 on the 15th of April, and indicates that the horizontal stress at

Omokoroa decreases for a time when the Sun is almost directly overhead, and the Moon's TGP is at its maximum while the Moon is on the opposite side of Earth, effectively decreasing tidal strain at that point. As with the 15th of April, a north-south, east-west plot (Figure 4.22) of predicted displacement of Omokoroa Peninsula starting 12:00 on the 14th of November until 00:00 on the 16th of November shows than mid-afternoon, when horizontal displacement is at its lowest, is also when eastward displacement turns to westward displacement. This (as expected) then produced the minimum predicted horizontal displacement when Omokoroa was perpendicular to the Moon-Sun axis, and vertical displacement was at its lowest due to minimum total TGP.

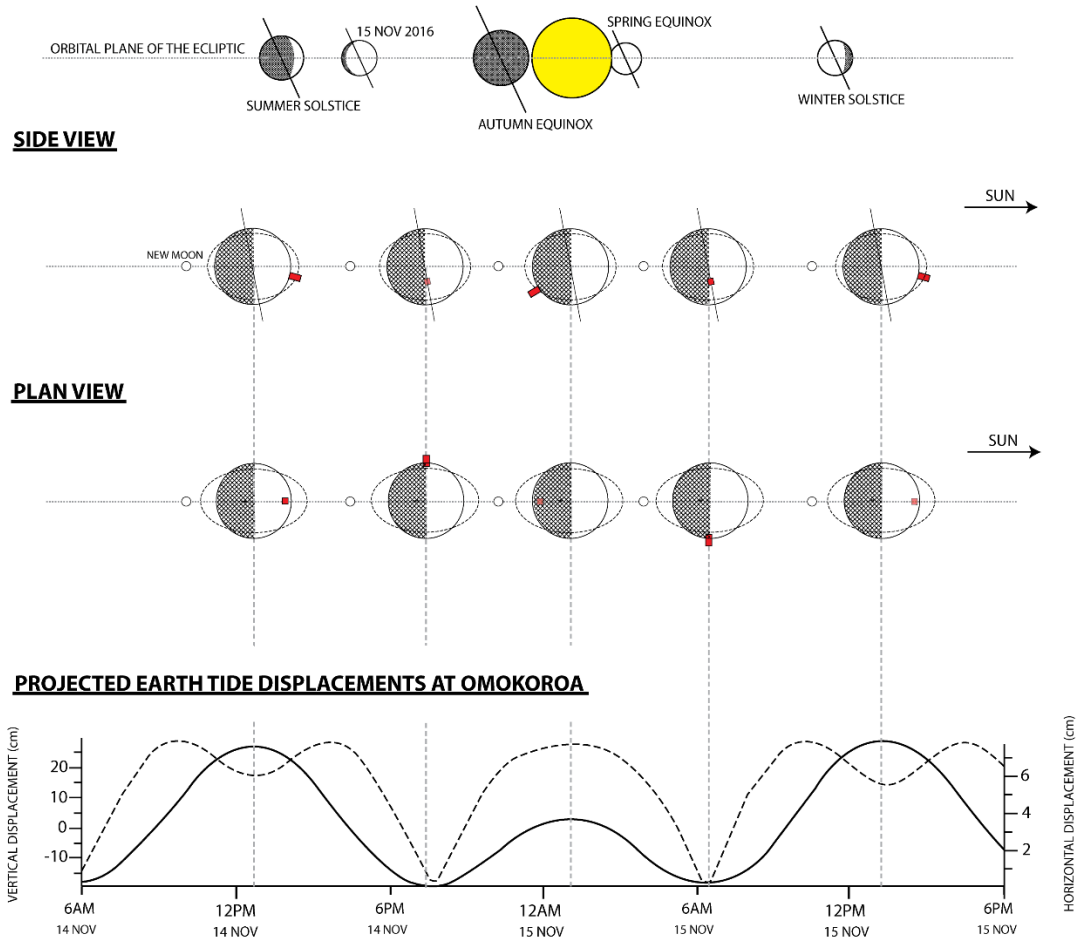

Figure 4.19: Sketch of Sun, Moon and Earth locations on the 14-15th of November 2016. Earth is in between the spring equinox and summer solstice, as well as the Moon being in a full phase. Note Earth's tilt leaning away from the Sun indicating the southern hemisphere moving into summer. Red cube is the approximate location of Omokoroa Peninsula, with its shape indicating vertical displacement caused by the Sun and Moon TGP. Dashed lines for side and plan views show exaggerated tidal pull from the Sun (side view) and Moon (plan view). Predicted vertical and horizontal (dashed line) Earth tide displacements at Omokoroa generated by CALSKY™.

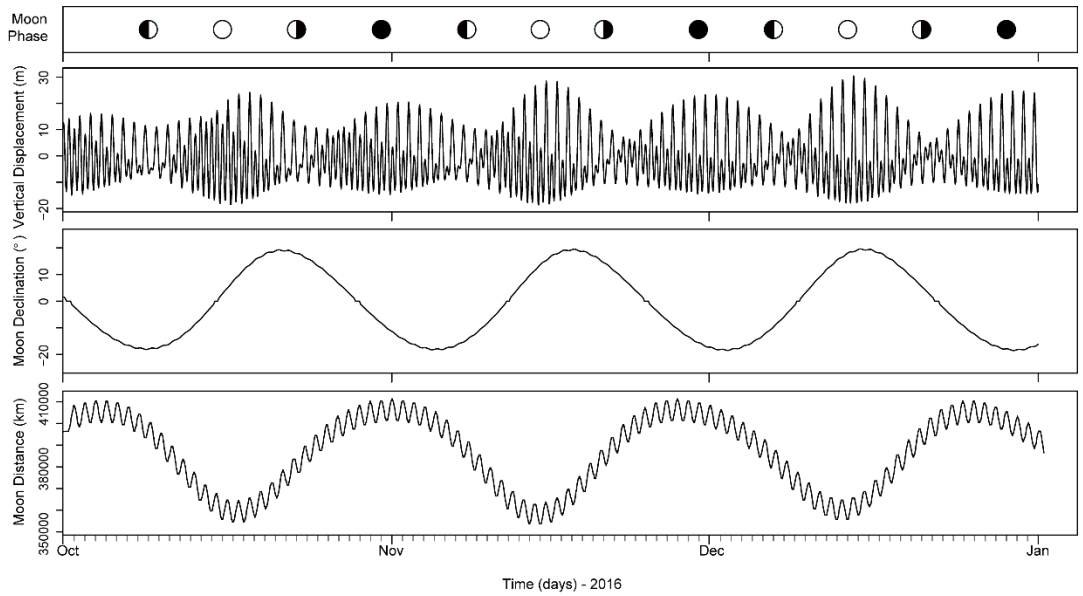

Figure 4.20: Predicted vertical displacement, Moon declination and distance from Omokoroa Peninsula. Data generated by CALSKY™.

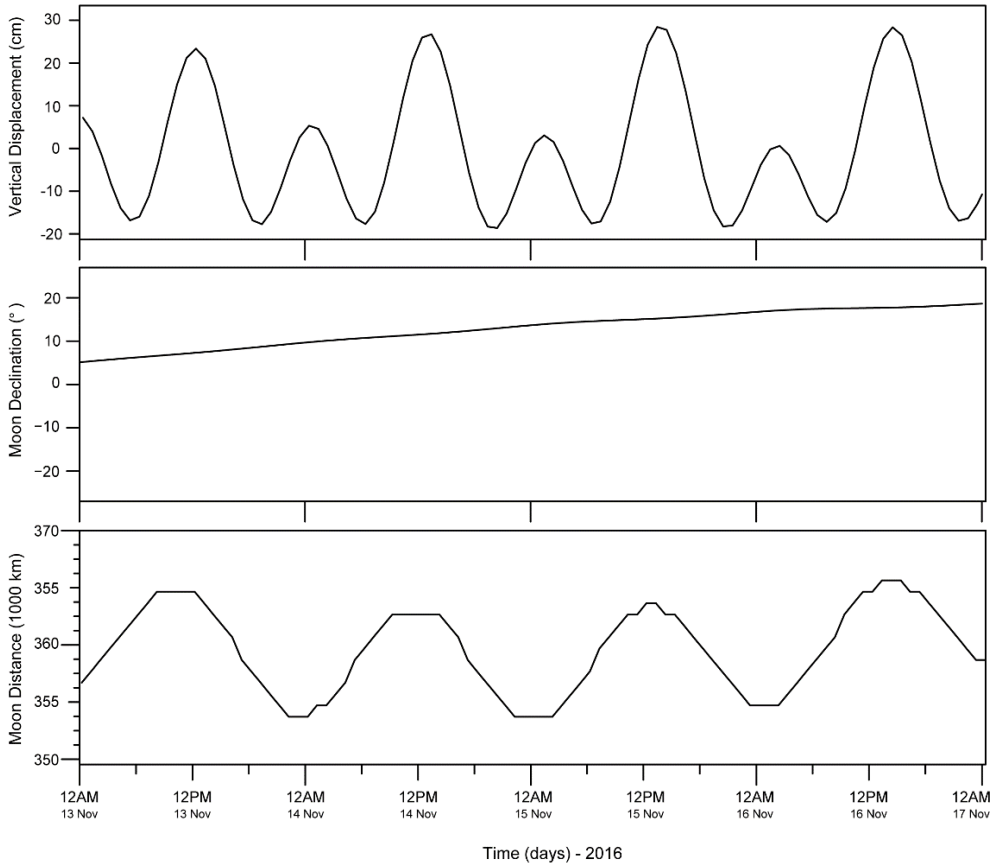

Figure 4.21: Close up of predicted vertical displacement, Moon declination and distance from Omokoroa Peninsula beginning mid-night on the 13th of November until midnight 17th of November. Note how Moon distance is not the primary factor for vertical displacement at Omokoroa, only coinciding with the less pronounced second semi-diurnal maximum Data generated by CALSKY™.

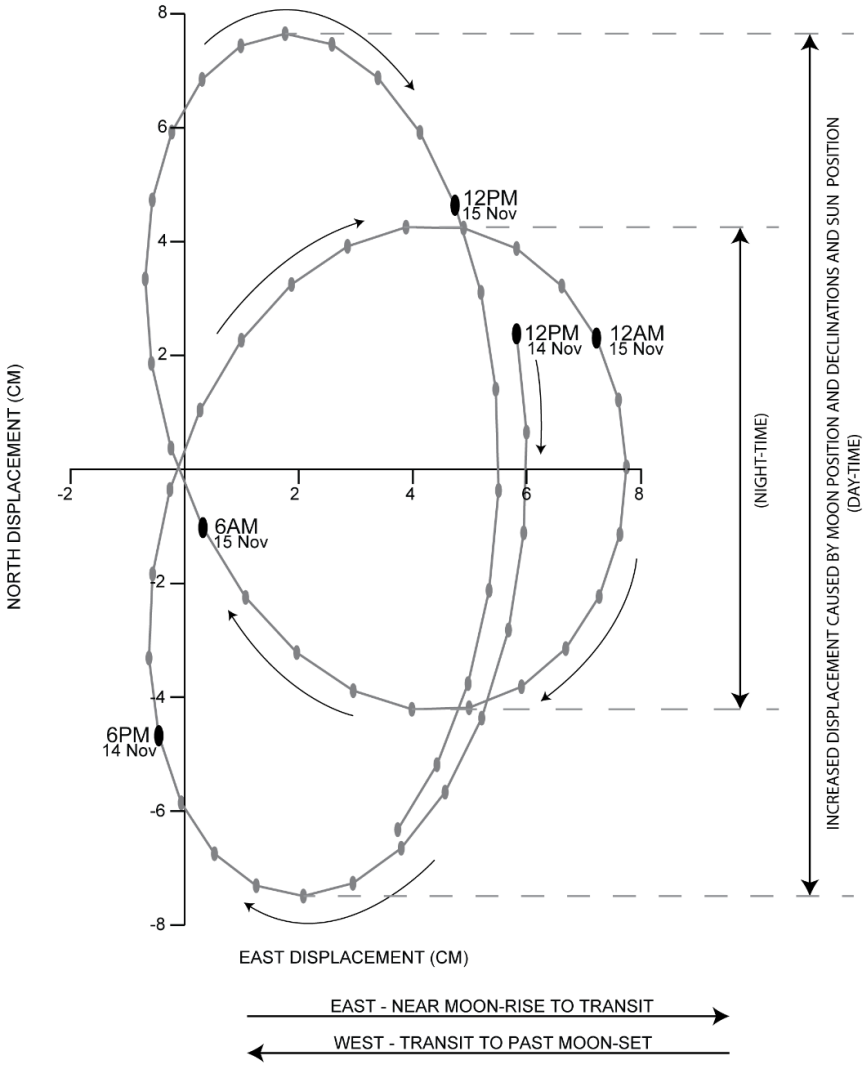

Figure 4.22: North-south, east-west plan view of predicted displacement at Omokoroa Peninsula beginning midday on the 14th of November until 15:30 15th of November.

The measurement at 06:30 on the 15th of November was used as the baseline measurement, as predicted north-south and east-west displacement was near zero in both directions. The borehole inclinometer measurements were then split into their north-south, east-west components, as previously undertaken for the 15th of April dataset (Figure 4.23). Once again, this was a time with minimum predicted vertical displacement (Figure 4.21).

Even with the A-axis only fluctuating approximately ±1 mm, the times at which the predicted northern displacement is zero coincide with zero displacement in the recorded data, while Earth tide velocity or rate of change also looks to determine inclinometer displacement amplitude. The recorded data also shows a similar wave shape as predicted for northern displacement, albeit inverted.

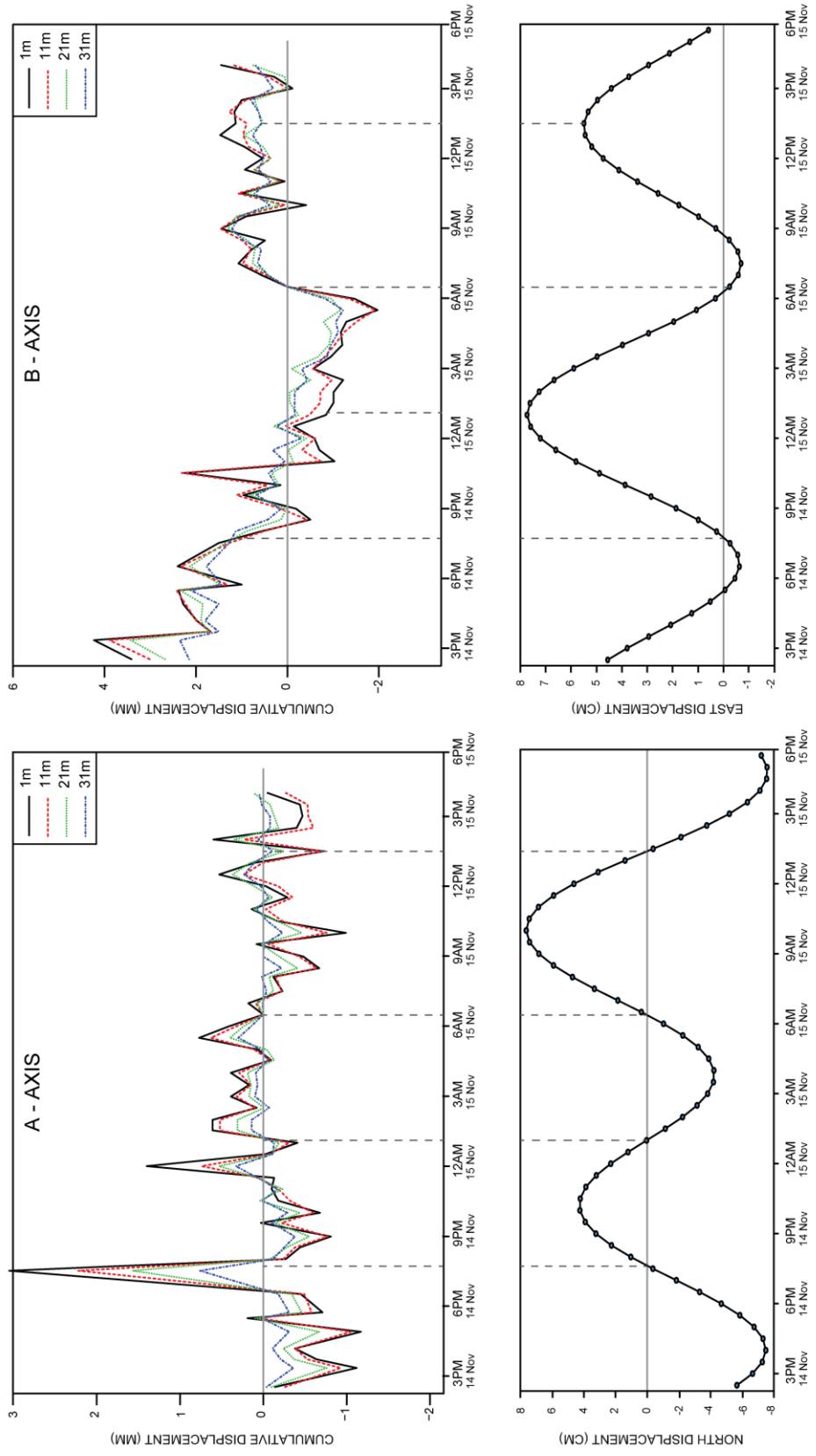

Figure 4.23: Plotted A- (north-south) and B- (east-west) axis displacements recorded from the on-site borehole inclinometer at different depths on The 14-15th of November (above). Predicted north-south, east-west displacements generated by CALSKY™ (below).

For the B-axis, the predicted eastern displacement ranges from >4 mm to -2 mm over the 25-hour period, with positive values primarily occurring in the morning and afternoon, and negative (western) values occurring late-night, and early morning. The measured borehole deviations do not directly follow the predicted east-west deviations shown in the plan view (Figure 4.22). However, some correlation does appear, namely around 19:30-20:00 (14th of November) and 06:30 (15th of November) having almost no deviation throughout the 42 m borehole inclinometer at these times, both coinciding with times where predicted vertical and horizontal displacement are at a minimum (Figure 4.23).

Although the predicted Earth tide displacements for the 14-15th of November are larger than those predicted for the 15th of April (Figure 4.28), the measured deviations are smaller. This suggests that although the Earth tides may be generating the stresses that drive the borehole shape changes, other factors affect the conversion of the horizontal stress to differential displacements along the length of the borehole.

4.4.3 Summary

Sections 4.3 and 4.4 concentrate primarily on solid Earth tides and their predicted effect on the Omokoroa Peninsula using Earth tidal models created from CALSKY™.

In Section 4.3 a definition of what Earth tides and how they are formed by the tidal generating potential (TGP) of the Moon and Sun was described. The seasons in regards to the tilt of the Earth and its distance to the Sun, as well as the Moons lunar phases, distance from Earth and declination all contribute to the TGP. The predicted Earth tides at Omokoroa were investigated in Section 4.4, with illustrations showing at what times TGP would be at its maximum on the two days where continuous recording of the borehole inclinometer was undertaken, being the 15th of April 2016 and the 14-15th of November 2016. These recordings were then interpreted in a plan view in an attempt to see if the elliptical shape the TGP follows as it pulls on Omokoroa (in a north-south east-west space) is similar to the recorded north-south, east-west displacement observed in the borehole used in conjunction with the borehole inclinometer, which does seem to correlate.

It was decided at this time that ocean tide loading would not be investigated due to evidence of its minimal contribution to vertical displacement (Goring & Walters, 2002), compared to local Earth tides.

4.5 CUMULATIVE DEVIATION AND ITS RELATION TO STRATIGRAPHY

Relative displacement of the borehole over these half-hour recordings on both the 15th of April and the 14-15th of November increase when closer to the surface. This means that from the base of the borehole at 42 m to the surface, pronounced deviations must be occurring within the surrounding materials that contribute to total displacement.

Due to the location, known history and recorded changes in displacement at 1, 11, 21 and 31 m noted in Figure 4.18 and Figure 4.23, the exaggerated ground displacement appears to be linked to the characteristics of the stratigraphic units and their boundaries throughout the measured borehole inclinometer readings. As previously described in the literature review (Chapter 2), the Bramley Drive site's stratigraphy is highly heterogeneous, with a mixture of volcanic based silts, sands and clays of various ages.

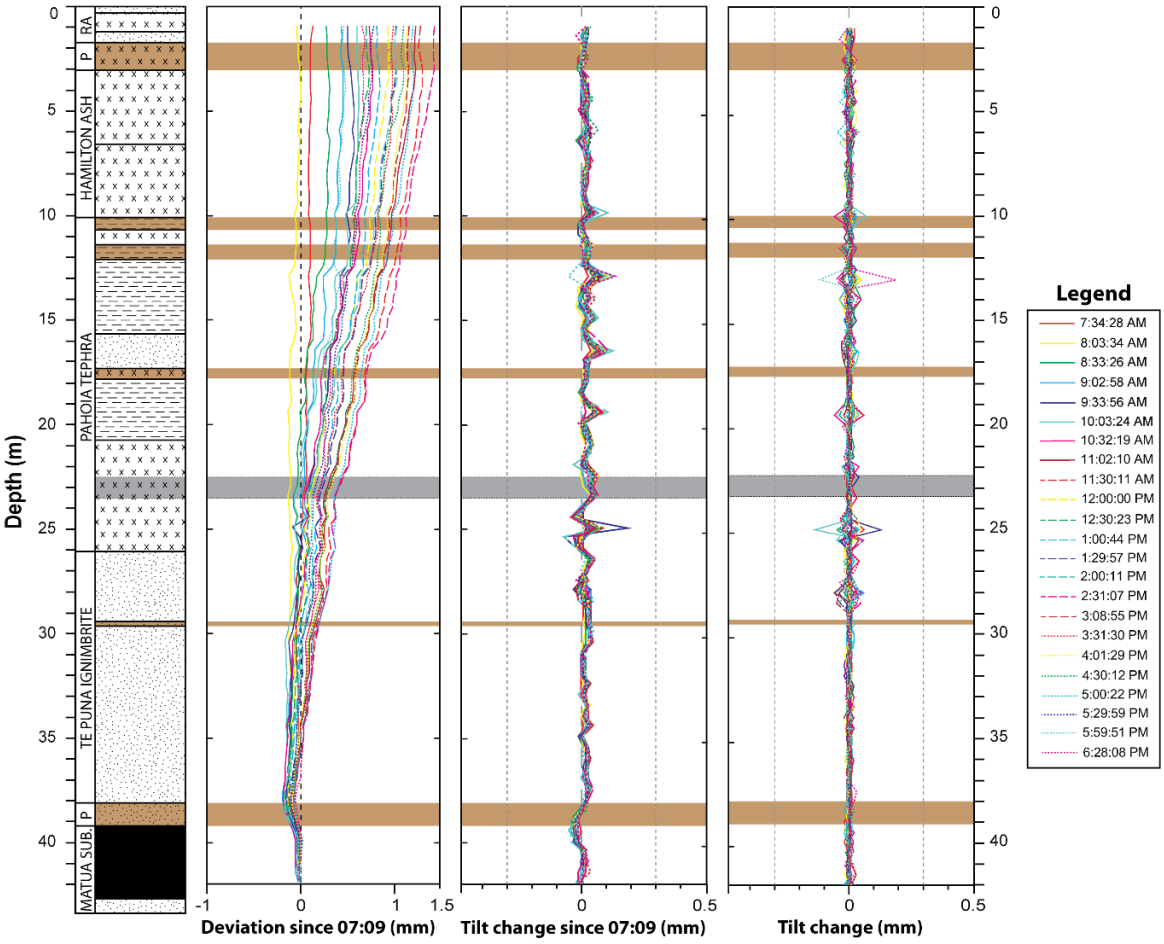

Figure 4.24: Cumulative deviation and tilt change recorded in the A-axis on 15th of April 2016, using the initial recording of 07:09 as a baseline combined with a stratigraphic log for the site displaying various stratigraphic units as well as varying soil units (left), tilt change using previous recording, better revealing times where large tilt change occurs (right). Note that paleosols (brown) and "sensitive layer" (grey) are highlighted throughout plots.

4.5.1 15th of April 2016

Beginning with the 15th of April, cumulative deviation and tilt change for the A-axis were calculated from the baseline of the initial reading recorded at 07:09 (Figure 4.24). As observed in Chapter 3, the displacement was positive. However, when considering half hourly changes, it is noted that at 08:33 ground movement in borehole is directed south until reaching the buried paleosol at ~38 m, where it then deviates in the northern direction through the Te Puna Ignimbrite and Pahoia Tephra, until reaching the two buried paleosols in the upper Pahoia Tephra, where displacement ceases. Throughout the morning cumulative deviation within the Te Puna ignimbrite overall remains negative, with the identified "sensitive layer" at approximately 24 m in depth acting as an inflection point, separating negative displacement with positive displacement. Positive deviation gradually becomes greater within the mid to lower Pahoia Tephra until 11:02 where the borehole inclinometer from 35 m upwards all moves in a positive (northward) direction through the "sensitive layer", as well as the two paleosols in the upper Pahoia Tephra, reaching a maximum positive cumulative deviation at 11:30 before trending southward. With this southern trend, zero cumulative deviation was almost constant until another large positive jump occurred at 14:31. Finally, at 17:29 displacement changed for the final time, trending negative.

What is important is the time when sharp kinks in the cumulative displacement occurred, which were 08:33, 11:02, 14:31 and 17:30. Each of these times were at or near direction changes in both north-south and east-west directions of the predicted Earth tide displacements (Figure 4.17). They also coincide with times where the predicted vertical Earth tide displacements are either at their steepest slope (fastest velocity) or before/immediately after a maximum/minimum horizontal displacement change (Figure 4.15), suggesting a link to Earth tides.

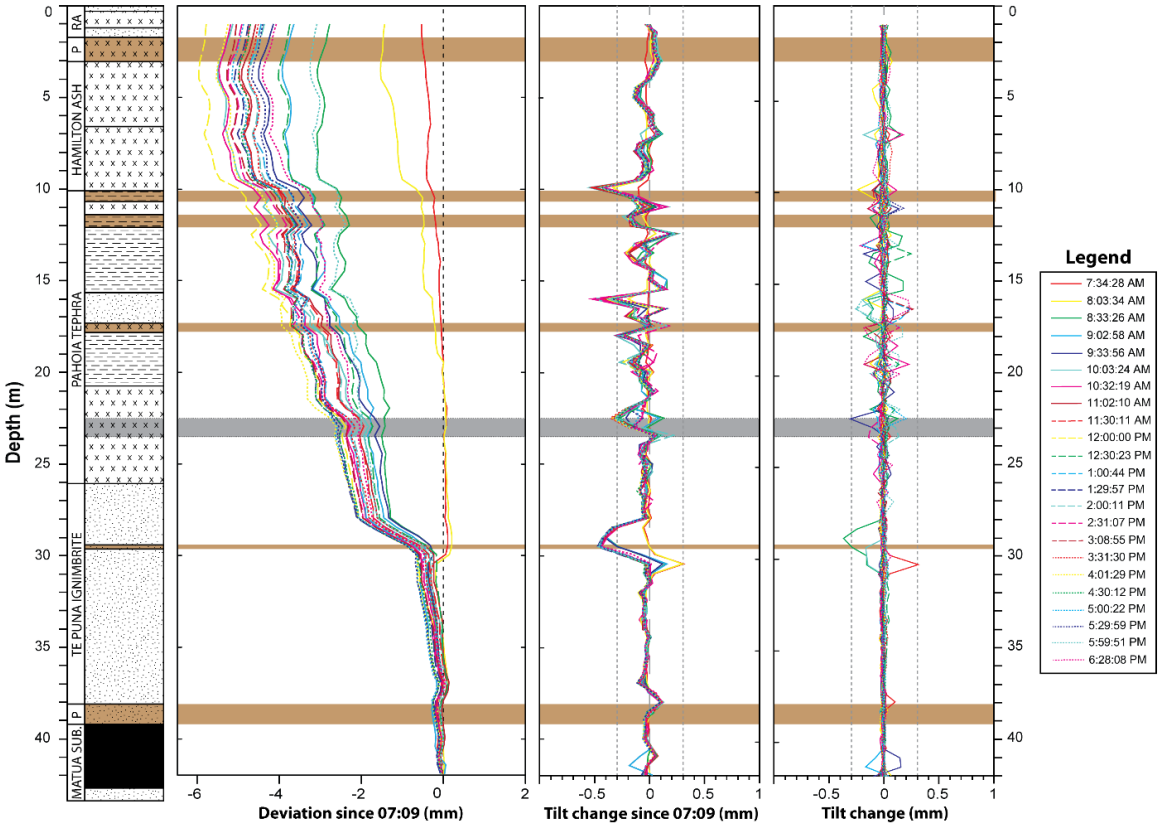

Figure 4.25: Cumulative deviation and tilt change recorded in the B-axis on 15th of April 2016, using the initial recording of 07:09 as a baseline combined with a stratigraphic log for the site displaying various stratigraphic units as well as varying soil units (left), tilt change using previous recording, better revealing times where large tilt change occurs (right). Note that paleosols (brown) and "sensitive layer" (grey) are highlighted throughout plots.

With the B-axis, the initial trend begins towards the west, with a sharp tilt change eastward at 07:34 near the buried paleosol located at ~29.5 m depth. (Figure 4.25) A second kink, albeit trending westward was also noted near the boundary between the Hamilton Ash and Pahoia Tephra. Sharp westward kinks continued to develop throughout the borehole at 08:03, primarily at or near soil unit boundaries and paleosol units.

At 08:33, the borehole inclinometer recorded multiple, sharp tilt changes throughout the borehole, most notably at ~29.5 m (paleosol), displacing the borehole westward by approximately 1 mm. Other than this kink observed in the Te Puna Ignimbrite, most of the tilt change between 08:03 until 08:33 was within the Pahoia Tephra. After 08:33 tilt change is primarily westward, with cumulative displacement also trending westward, resulting in almost 6 mm of displacement 1 m below the surface at 12:00. At 12:30 deviation near the base of the borehole straightens out, which in-turn pulls the rest of the borehole eastward by approximately 2 mm, 1 m below the surface. This eastward change is short lived as very minor westward displacement continues from

13:00 until 17:59. Finally, a distinct eastward tilt occurred at 17:59 when the observations ended.

Based on the predicted Earth tide, Omokoroa would be leaving the high TGP of the Moon at 08:33, causing a sharp westward tilt change, as well as driving the general trend of the entire borehole. At 12:30 a minor, short lived tilt change eastward should occur, while movement should still be continuing in a westward direction. It should be noted that the A- and B axes are not directly recording north-south, east-west components due to its installation position, so the directions of the measured tilts will not match exactly with the predicted ones. The 12:30 measurement follows the change of direction of the predicted tides from south-north to north-south (Figure 4.17). The period of minor deviation from 13:00 until 17:59 coincides with low predicted vertical displacement (low tide) as well as low predicted horizontal displacement, thus this period is seen as a time in which tidal strain would be minimal. At 17:59 where the distinct eastward tilt is observed, this is the same time at which vertical displacement velocity is at its highest, while horizontal displacement eastward is approaching its peak, which occurred at approximately 20:00 that evening.

Thus, looking at the distinct kinks and generally trends of movement in regards to Earth tides and the TGP of both the Moon and Sun, is its evident that changes between stratigraphic units, as well as presumed lower strength sub-units within units, such as the "sensitive layer" and various paleosols, have a high tendency to cause localised exaggeration of displacement, possibly being points where the pressure caused by the strain created by tidal forces is relieved.

4.5.2 14-15th of November 2016

Cumulative deviation and tilt change for the A-axis were calculated using the initial recording at 14:32 on the 14th of November (Figure 4.26) as the baseline. Excluding 17:29, all recordings up until 19:30 have a prominent southern displacement (the 19:00 recording has been removed due to a measurement error while on-site). 19:30 may also be user error due to its sharp kink beginning at ~38 m, which is dissimilar to previous and future values. However, it should be noted that 19:30 coincides with both minimum predicted horizontal and vertical displacement, as well as a direction change from west to east, so a positive value would be expected here as both predicted north and east displacement are near zero (low stress), but the magnitude of the effect is larger than the data trends observed in the other April and November recordings.

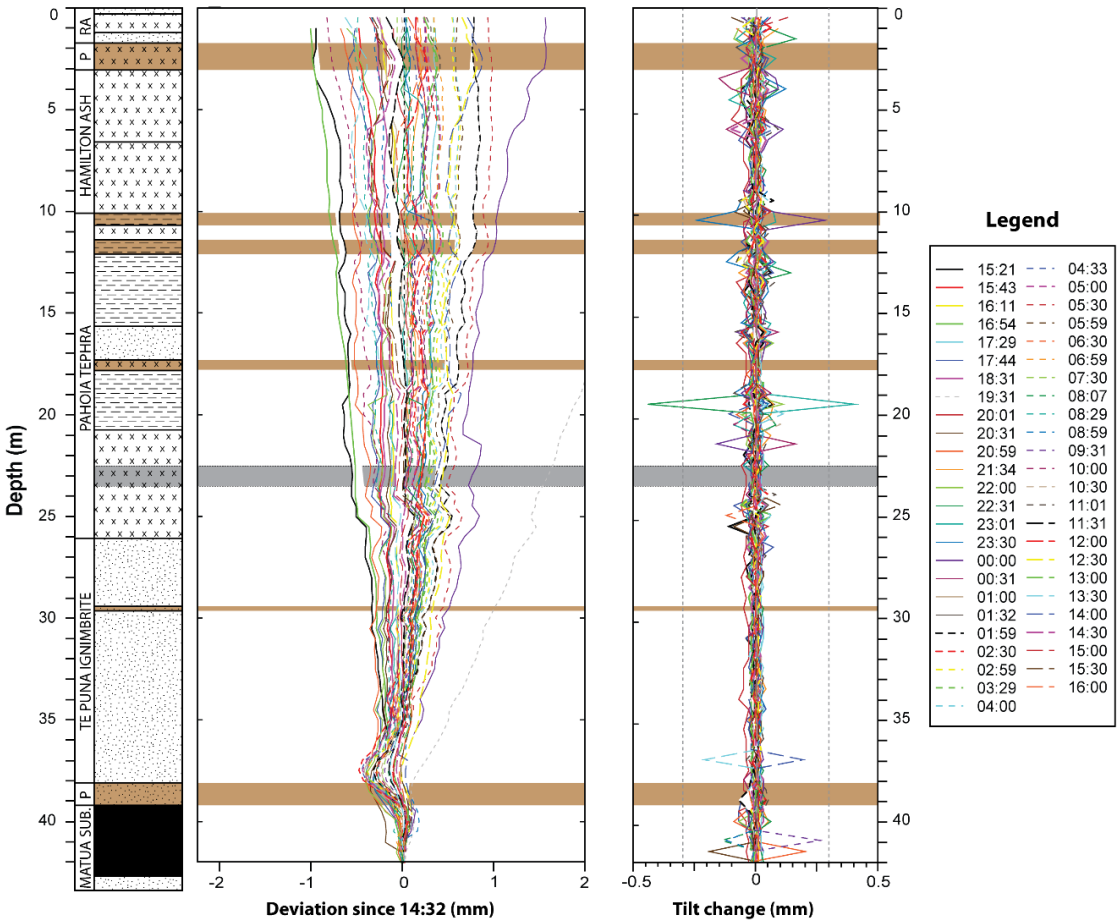

Figure 4.26: Cumulative deviation recorded in the A-axis on 14-15 November 2016, using the initial recording of 14:32 (14 Nov) as a baseline combined with a stratigraphic log for the site displaying various stratigraphic units as well as varying soil units (left), tilt change using previous recording, better revealing times where large tilt change occurs (right). Note that paleosols (brown) and "sensitive layer" (grey) are highlighted throughout plots.

As observed in April, when predicted vertical displacement reaches its maximum velocity and horizontal displacement (Figure 4.24), tilt changes become more pronounced. For the 14th of November this begins to occur at 21:00 when deviation sways south, then negating the previous deviation by 21:30. Between 22:00 and 22:31 this sway begins again, first southward, then northward. By 23:01, primary deviation begins to occur at the unit boundary between the Hamilton Ash and Pahoia Tephra (Figure 4.26), where 23:30 and 00:00 (15th of November) display sharp tilt changes at this location. By 1:00 tilt change became minimal, as well as trending northwards.

By 08:07, the cumulative deviation from the initial recording (14:32) is almost zero, with only the now pronounced curve in the borehole located at approximately 37.5 m which is near the unit boundary of the Te Puna Ignimbrite and Matua Subgroup. The familiar trend of increased fluctuations and displacement begin at 08:29, where predicted Earth tide vertical displacement is rising and horizontal displacement begins to reach its peak. The time between 09:31 until 11:01 is important, as 09:31 almost

coincides with the maximum predicted northern displacement (Figure 4.22) and thus shows minor northern displacement. 10:00 (15th of November) then moves in a southern direction, coinciding with maximum predicted northern displacement, consistent with a similar southward trend recorded 12 hours earlier at 22:00 (14th of November).

Another observation when the cumulative displacement is also zero compared to the initial reading is 11:30. Finally, as per the 15th of April, as the eastward displacement changes to westward displacement, the A-axis is influenced due to its offset installation. This occurs at 13:30 with a quick change southward, which immediately recovers by 14:00. This is short lived however, as by 14:30 the southern displacement occurs again, remaining there until testing concluded at 16:00 on the 15th of November.

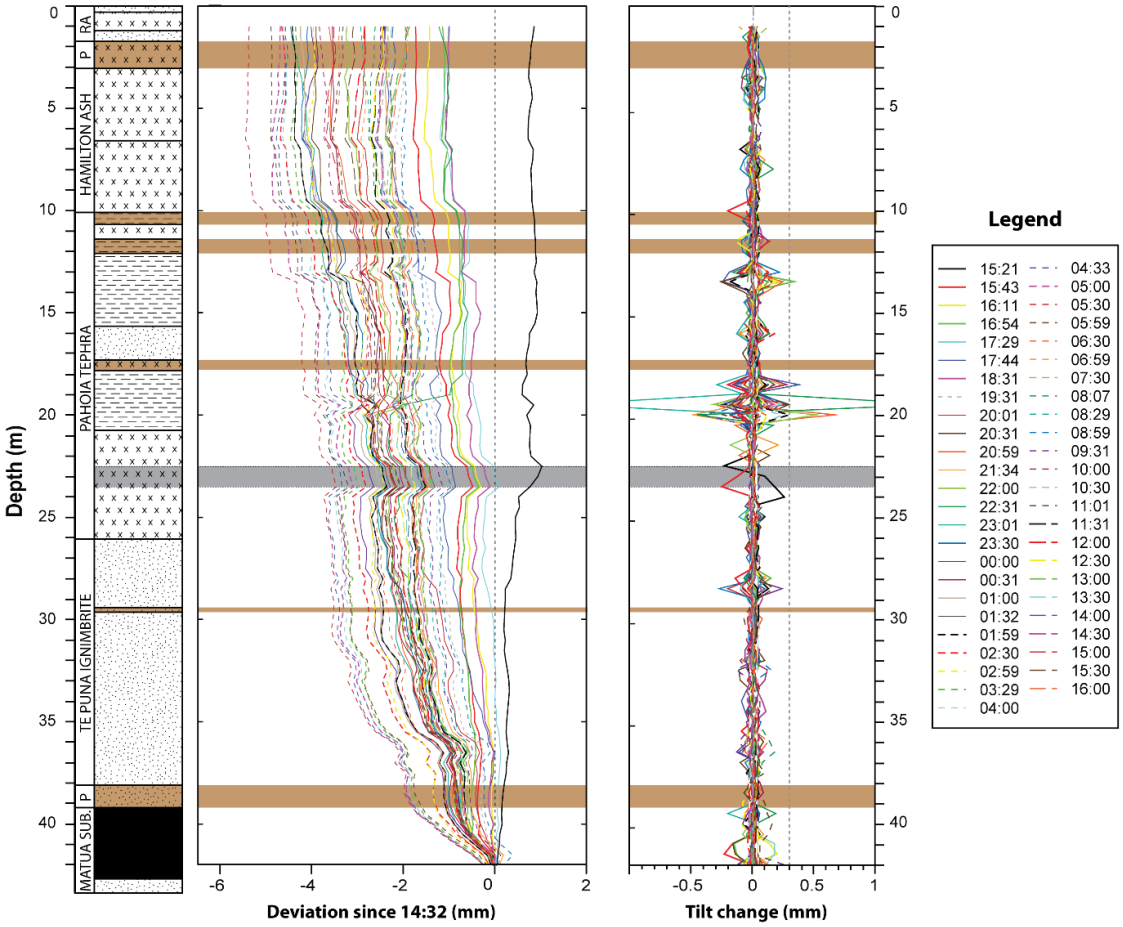

Figure 4.27: Cumulative deviation recorded in the B-axis on 14-15th of November 2016, using the initial recording of 14:32 (14 Nov) as a baseline combined with a stratigraphic log for the site displaying various stratigraphic units as well as varying soil units (left), tilt change using previous recording, better revealing times where large tilt change occurs (right). Note that paleosols (brown) and "sensitive layer" (grey) are highlighted throughout plots.

Displacement in the B-axis is much more pronounced compared to the A-axis, and this has been consistent throughout the years of borehole inclinometer recordings. Deviation from 14:32 (14th of November) begins with multiple sharp kinks within the Pahoia Tephra, mainly within the "sensitive layer". Deviation in the buried lignite within the Matua Subgroup is also observed, following the westward trend of the afternoon recordings. This westward trend, as well as recurring tilt changes throughout the Pahoia Tephra occurs until 20:59 where a sharp tilt change eastward occurs at 20 m depth, in a clayey soil unit located within the Pahoia Tephra. While not exactly at a soil unit boundary, it is close (within 1 m), and it is possibly a result of relieving strain as the predicted east-west displacement had changed from westward to eastward at approximately 18:30-19:00.

Sharp tilt change at 20 m eastward at 21:34 and seems to almost trigger multiple displacements eastward directly after. The main being at 22:30 where cumulative displacement at 20 m depth, as well as at 1 m below the surface was almost 2 mm east.

By 23:00 any previous displacement at 20 m had disappeared, and only minor westward displacement occurred until 05:30.

As discussed above, after 06:00 the predicted north-south, east-west Earth tide displacement is approximately zero. Recorded displacement from 05:30 begins to trend eastward slowly, and other than a minor eastward kink occurring at the base of the borehole at 09:30 coinciding with near maximum Earth tide horizontal displacement, all further observations fluctuate collectively less than 2 mm, never moving eastward enough to return to the initial reading at 14:32 the previous day.

4.6 COMPARISONS OF 15TH APRIL AND 14-15TH NOVEMBER 2016

For animated slideshows of Figure 4.26 and Figure 4.27 depicting the borehole inclinometer cumulative deviations and tilt change over their respected time periods, please refer to the CD-ROM located at the end of this thesis. These animations were used to inform the interpretations and comparisons between the observations.

Considering the deviations of the stratigraphic units are in response to the effects of the Earth tides, the most obvious difference between the recordings undertaken in April and November is the much larger TGP exerted on Omokoroa Peninsula in November due to the occurrence of a full Moon, and the closer distance of the Moon to Earth (Section 4.4.2). Figure 4.28 shows the differences between the Earth tides on the two testing days, and indicates how much larger tidal forces were in November. The north-south, east-west displacement plot of the 14-15th of November is almost twice as large as the 15th of April, while predicted vertical displacement have a much large range of -15 to 25 cm compared to April's -10 to 10 cm. Horizontal displacement velocity is also much higher as shown by the steepness of the slopes, as well as their shapes being different, with November having three pronounced diurnal horizontal maximas compared to April's two; predominantly caused by the different Moon phases (full Moon compared to first quarter).

Looking at Figure 4.24 and Figure 4.26 that both display A-axis deviation and tilt change, the differences were primarily in the tilt change magnitude throughout testing, with November returning almost 0.5 mm of tilt change multiple times throughout testing. These constant minor but observable tilt changes are likely due to increased tidal forces due to the time of year and Moon position (stated previously). Working

from the base of each borehole recording, both April and November tests were influenced by the buried paleosol beginning at 38 m. The direction of the deviations either east or westward were then dictated by the sites position relative to "high" and "low" stress periods. Other stratigraphic units of significance are located in the zone at approximately 25-26 m in depth, which is inferred to be the boundary between the Pahoia Tephra and Te Puna Ignimbrite, with the November data showing a clear change in tilt. Tilt change was also observed at ~20 m depth coinciding with a boundary between a clay and silt within the Pahoia Tephra. Both tests also show tilt changes at 13 m, located slightly beneath a buried paleosol, as well as within a buried paleosol at 10 m. Tilt change from 1-10 m was minor in April, especially compared to November and may be due to additional factors closer to the surface, such as soil responses to temperature, insolation and rainfall.

As previously stated, most ground displacement occurs in in the east-west direction due to strain exerted by tidal forces. Comparison of Figure 4.25 and Figure 4.27, which show the cumulative displacement of the B-axis in April and November recordings, identifies multiple depth zones within the borehole that are more susceptible to tidal strain than others.

Beginning from the base of the borehole recordings, November measurements indicate much higher deviation within the Matua Subgroup lignite than what occurred in April. This is likely due to the much larger tidal strain occurring in November, which could affect soil units to a greater depth. This suggests that a deeper borehole may return a much higher total deviation and that the current boreholes depth of 42 m limited the amount of deviation observed in November.

The paleosol between 38-39 m is a point at which no deviation occurs in either April and November recordings. For the Te Puna Ignimbrite minor tilt change, thus cumulative deviation occurs throughout both records; however, at 29.5 m April recordings reveal a sharp deviation at the point where predicted west-east displacement changes to east-west displacement as previously explained. This kink occurs within a thin sandy paleosol.

The presence of this paleosol suggests that the Te Puna Ignimbrite unit above this paleosol is younger than the Ignimbrite beneath, and is either another unclassified ignimbrite or reworked material. In any case, this upper Te Puna Ignimbrite will have slightly different characteristics than the mid-lower Ignimbrite, further proving

changes in soil units may be an area of stress relief. It is not known why November did not show any observable change at this depth; however, a similar sharp deviation occurred at approximately 20 m which was not observed in the April recordings, and may have relieved the same tidal stress albeit at a shallower depth.

The "sensitive layer" at ~23 m depth, previously discussed as a problematic unit due to its high susceptibility to moisture content change, was observed as a soil unit that displayed minor tilt change throughout both testing periods. Tilt change throughout the Pahoia Tephra is also much more apparent than other soil unit groups (Te Puna Ignimbrite, Hamilton Ash, Rotoehu Ashes). Moving up through the Pahoia Tephra, the April recordings showed a sharp kink between the boundary of a clay and sand unit at ~16 m, while the November results showed one at 13 m, which doesn't match with a known soil unit change. Finally, the two paleosols between 10-12 m depth are zones where increased borehole tilt changes are apparent; both testing periods showing sharp kinks near the soil boundary between the Hamilton Ash and Pahoia Tephra.

Interestingly both periods of half hourly measurements showed a maximum of approximately 6 mm cumulative deviation, independent of the total recording times (12 hours and 25 hours) and the Earth tide magnitude.

4.6.1 Summary

In Sections 4.5 and 4.6 the hypothesis of pronounced deviations within the surrounding stratigraphy was introduced. With the Bramley Drive sites highly heterogeneous, volcanic based stratigraphy of various ages it is believed that sharp changes in soil strength and structure between each layer may be an outlet for where the pressure caused by the strain created by tidal forces is relieved. Areas that include but are not limited to unit boundaries, paleosols and the characteristic "sensitive" clay-rich layer located in the lower Pahoia Tephra show recorded tilt change, dependent on the time of day, contributing to cumulative deviation throughout the borehole.

The direction of the predicted Earth tides seems to dictate the borehole's tilt, moving eastward when the Moon begins to rise and westward when the Moon begins to set, with periods of little to no movement when vertical velocity of the Earth tides are low, which are usually at the same times as no horizontal displacement. Times where horizontal displacement are at maximums are times at which the tide generating potential (TGP) of the Moon and Sun change directions. This quick change in direction, caused by the location of the Moon and Sun correlate with the periods where

noteworthy tilt change occurs and may be times where the amount of tidal strain was enough to form a shear surface that over time could increase with successive diurnal tides. This is probably due to recorded data from both April and November 2015 not completely returning to the same location it began every 12.5 to 25 hours (lunar day).

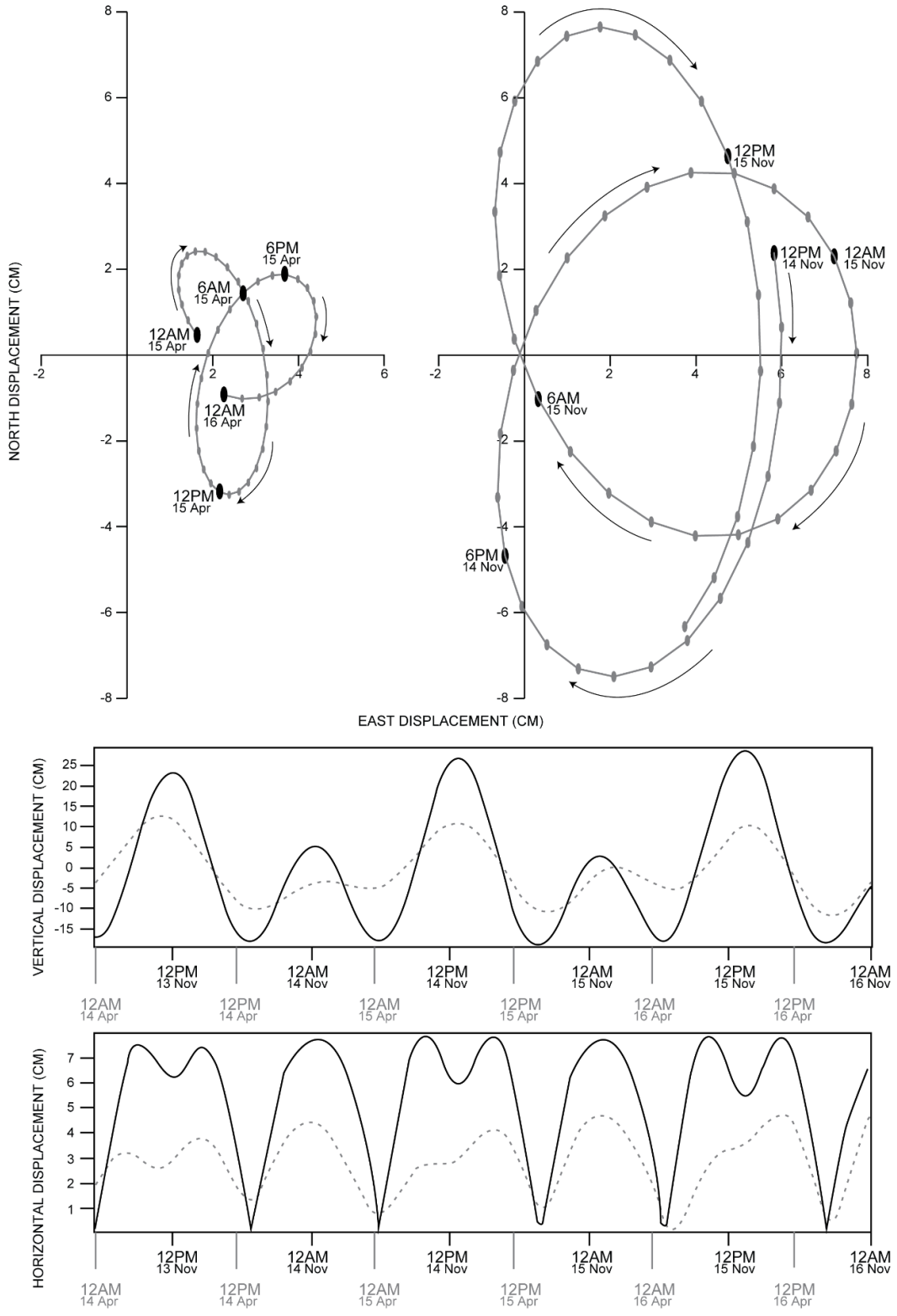

Figure 4.28: Comparison of predicted north-south, east-west displacement (above), as well as vertical and horizontal displacement between the 15th of April (grey and dashed) and 14-15th of November 2016 (below).

4.7 THE EFFECT OF RAINFALL AND TEMPERATURE

From the observed changes in the Z-axis (elevation) acceleration presented in Chapter 3, it was apparent temperature variation was a major cause of acceleration change, while rainfall tended to cause a dampening effect that could last up to several days after the event. However, while the accelerometer data followed a diurnal cycle, the timing of the prominent peak in cycle varied, occurring at either mid-day or mid-night depending on the time of year. It was not immediately obvious why this pattern was present, as it didn't consistently follow the diurnal temperature cycle, and rainfall didn't follow a diurnal cycle. Weather and tidal effects on the accelerometer, and hence their effect on the surficial materials at the Bramley Drive site, will be split into separate sections that will deal with the diurnal and seasonal effects with regards to temperature, solar irradiance and Earth tides, as well as short-term acceleration dampening and its link with rainfall.

4.7.1 Diurnal and seasonal effects

As previously suggested in Chapter 3, warmer months (summer) are associated with larger fluctuations in the Z-axis (ground elevation), which is presumably caused by the larger diurnal variations in air temperature, easily fluctuating over 10 °C over 24 hours (Figure 4.29). During summer months an increase in air temperature coincides with a sharp positive acceleration of the Z-axis, the larger the temperature delta over a given day, the larger the acceleration change. In spring and autumn months this same trend occurs, although to a lesser extent.

The accelerometer measurements indicate that the Z-axis tends to most closely follow the air temperature, as the soil temperature measured at 5 cm depth lags behind both the air temperature and the Z-axis acceleration. This is presumably due to the accelerometer being installed at the surface (Chapter 3). If the accelerometer was partially or completely buried in the soil, one could assume that similar trends would be observed, albeit to a lesser and slightly lagged extent due to soils higher specific heat (more energy to heat than air) as well as the soils ability to retain heat compared with air. Hence, it is assumed that whatever is measured by the accelerometer is representative of the changes occurring with the surficial materials of the Bramley Drive site.

The surface temperature of the soil surrounding the accelerometer is given by the surface energy balance, which comprises the radiation balance, thermal properties of

the soil (Table 4.1), atmospheric exchange processes and the presence of vegetation (Arya, 2001). Typically, on clear days the maximum soil temperature occurs 1-2 hours after the maximum insolation and minimum soil temperature in the early mornings. The maximum diurnal ranges occur when the soil is relatively dry, under clear skies and calm weather (Arya, 2001). What is of great importance to this typical diurnal temperature change is the presence of moisture within the soil. This is due to a substantial proportion of the available insolation being dispersed by latent heat due to evaporation if the soil is moist or saturated.

Recording the moisture content of the surface soil would confirm the presumption of drier soil in warmer months and moister soil in wetter months. However, as moisture content data are not available, it will be assumed that the effect of increased insolation and increased temperature range in summer/warmer months dry out the surface of the soil sufficiently, to prevent or restrict water evaporation from within the soil's pore spaces. Therefore, the available heat energy primarily heats the soil itself, which would minimise the effect of soil shrinkage, common in soils where pore space filled with water is replaced with air (until the moisture content reaches the shrinkage limit). Depending on the structure and makeup of the soil this could also lead to surface cracking, however as the site is covered in thick, unkempt grasses, shallow surface cracking could not be observed on site.

Another effect of a dry surficial soil is its ability to greatly increase in temperature in response to heating due to the low specific heat values of both the soil and the air found in its pore spaces compared to water (Table 4.1). The direct temperature increase could possibly trigger thermal expansion of the soil, where the minerals within the soil increase in volume, thus possibly causing a positive direction response in the Z-axis. While this is a possibility, no published research has been found on the expansion of dry soil in response to a minor increase in temperature. Instead, mineral expansion is widely acknowledged to be in response to temperatures exceeding 100 °C due to fire, radioactivity, or a gas/electrical pipeline releasing thermal energy into a soil that cannot dissipate the heat quickly enough. This can result in an exponential increase in the soil temperature, known as thermal runaway (New Zealand. Ministerial Inquiry into the Auckland Power Supply, 1998).

Table 4.1: Thermal properties of materials (Arya, 2001)

Material	Condition	Mass Density (ϱ) ($kg\ m^{-3} \times 10^3$)	Specific Heat (C) ($J\ kg^{-1}\ K^{-1} \times 10^3$)	Thermal Conductivity (k_g) ($W\ m^{-2}\ K^{-1}$)	Thermal Diffusivity (v_g) ($m^2\ s^{-1} \times 10^{-6}$)
Air	20 °C	0.0012	1.01	0.025	20.5
Water	20 °C	1.00	4.19	0.57	0.14
Ice	0 °C	0.92	2.10	2.24	1.16
Sandy Soil	Fresh	1.60	0.80	0.30	0.24
Clay Soil	Dry	1.60	0.89	0.25	0.18
Peat Soil	Dry	0.30	1.92	0.06	0.10
Rock	Solid	2.70	0.75	2.90	1.43

In the colder, winter months solar insolation is much lower due to the more acute angle of the Sun's rays and cloud cover, and rainfall tends to be more common, so that the soil moisture content at the surface increases. If the rate of rainfall is fast enough to overcome the subsurface infiltration rate, thereby saturating the surface soil, excess pore water pressure can rise causing a temporary, positive volume change. Also, pore space filled with water from recent rainfall will remain for longer within the soil pore space as the specific heat required to evaporate the water is much higher, effectively damping the change in soil temperature. This also means on warm days where insolation is high and rainfall does not occur, evaporation may occur, causing the surface of the soil to contract, triggering a negative direction response in the Z-axis (Figure 4.29).

Without additional information on the soil temperatures at different depths, as well as the soil moisture contents, it is not possible to quantify the effects of temperature and rainfall directly. However, the available data allow preliminary interpretation of the effect of temperature on diurnal ground movements, primarily in the Z-axis, which indicates that temperature change is a factor in Z-axis direction change. However, the direction changes in the accelerometer are not only affected by local weather conditions. such as insolation, rainfall and temperature, but also the Earth tides that have been observed in the inclinometer measurements. A potentially important factor is that the magnitude of the Earth tides forcing doesn't follow a seasonal pattern, while the weather conditions do. Therefore, it is possible that the relative contributions of the weather and tidal force will vary over the seasons.

In Figure 4.29 the predicted Earth tide vertical displacement provided by CALSKY™ has been superimposed over the Z-axis accelerations. While not an exact match due to the other factors contributing to Z-axis acceleration, I believe that Earth tides are the primary cause for the "mirrored" or inverted observations in June observed in Chapter 3 and Figure 4.29, where Z-axis acceleration is positive near mid-night where air temperature is near the lowest point of the diurnal cycle, opposite to what is observed in January, March and September. As previously explained, the June temperature change is much less than in December due to decreased insolation and wetter soils, so the temperature effect on acceleration is greatly reduced.

However, this does not necessarily explain the sudden shift to the maximum positive Z-axis acceleration occurring at night instead of the day like most other months. Evaporation of saturated or semi-saturated soils may be the cause of the negative trend of acceleration in the day, but with no recorded moisture contents this cannot be quantified. Further, the observable trend of a similar Z-axis minimum of approximately -0.1 ms^{-2} in all four months suggests that this may be an offset resulting from the installation as discussed earlier for the X- and Y-axis offsets. The only other factor which could cause a diurnal, positive direction change is the TGP of the Moon and Sun. As discussed in Section 4.3, the tilt of the Earth with regards to the Sun is the primary influence of when the maximum combined TGP by the Sun and Moon occurs during the daily cycle; with the Sun's maximum TGP occurring in the day-time at the December Solstice, and the Sun's maximum TGP occurring in the night-time at the June Solstice.

This hypothesis would also explain the much larger accelerations in December compared to March and September, as maximum TGP would combine with the hypothesised thermal effect that occurs each day when temperature is at its highest. Both March and September do not follow the predicted vertical displacement quite as well, instead appearing to be more affected by the temperature differentials occurring each day, and would be why acceleration change is higher in March, compared to September.

Another less obvious trend is the minor downward step change in the Z-axis during prolonged rainfall, possibly indicating a slight drop in the surface position. In both December 2015 and June 2016 (Figure 4.29) prolonged rainfall results in diurnal Z-axis minimums being visibility lower. The likely cause is the introduction of additional mass provided by the infiltrating water, filling pore space, which in turn increases the

soils ability to transport water further into the soil profile. With enough rain over a short period (>20 mm in 24 hours in December and >70mm in 24 hours in June) the added weight of water infiltrating through the shallow tephras increases the loading on the deeper stratigraphic units resulting in compression of the soil structure for a short period until the water can evaporate, dissipate by reaching groundwater or escaping out from the face of the slope from perched groundwater aquifers located within the Pahoia Tephra.

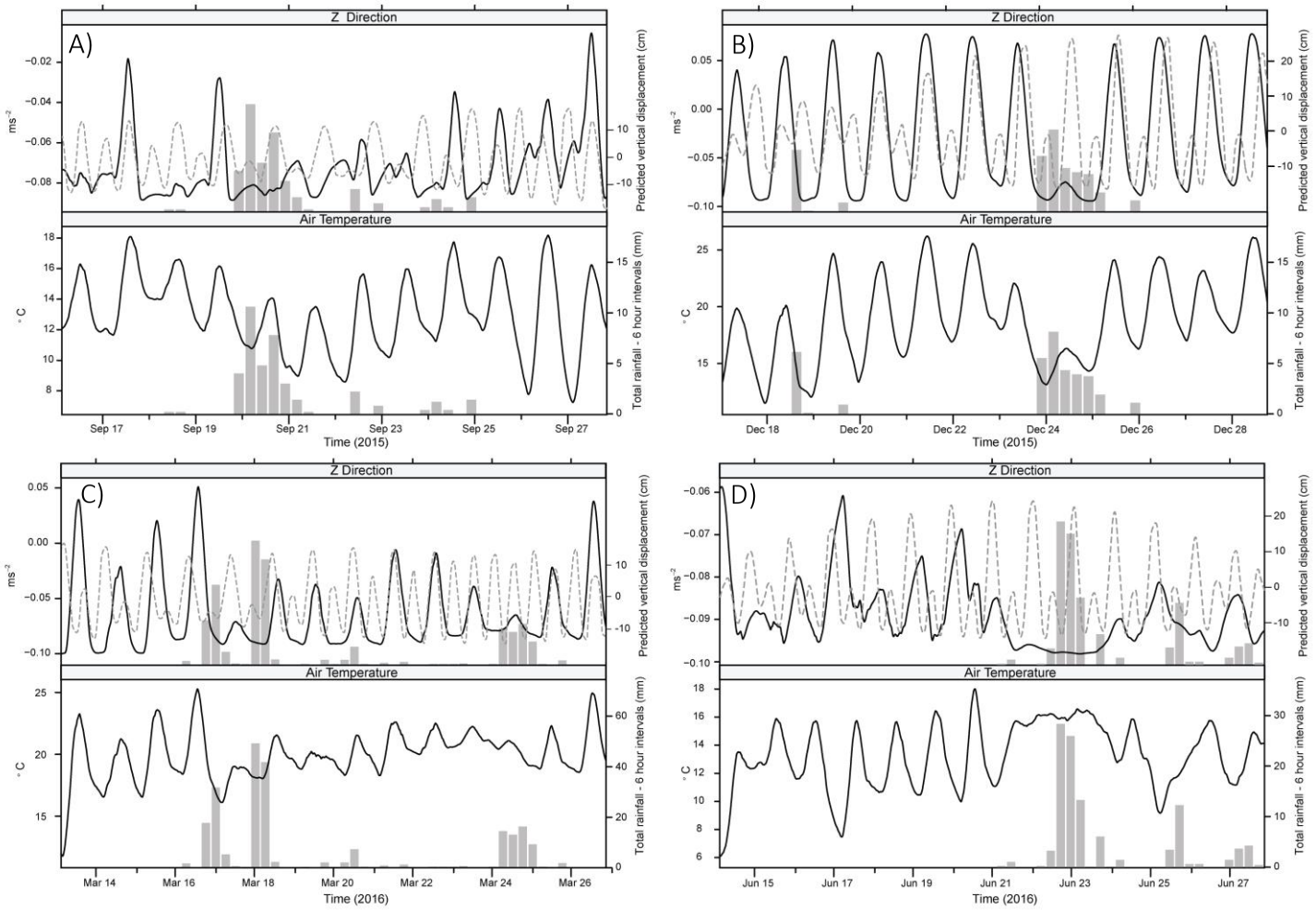

Figure 4.29: Plots of two week periods at 4 different months that are at the September Equinox (A), June Solstice (B), March Equinox (C) and December Solstice (D). Each plot includes recorded Z-axis acceleration change imposed with predicted vertical Earth tides (grey dotted) at the Bramley Drive site (upper), as well as recorded air temperature and total rainfall over 6 hour periods (grey). Note: Z-axis and air temperature data have been smoothed by taking a 1 hour rolling mean.

4.7.2 Acceleration dampening

What was also observed in Chapter 3, as well as Figure 4.29, is the dampened acceleration during periods when the diurnal air temperature range is temporally reduced. This decrease in temperature change is the combination of local cloud cover, insolation, precipitation and wind, all of which are important factors that affect local air temperature. This is consistent with the suggestion that the reduced diurnal temperature range during colder months' results in a reduced influence of weather conditions relative to Earth tide effects outlined above.

It's now clear that changes in air temperature, as well as changes in soil temperature do affect the surface of the Bramley Drive site, causing it to lift and fall in a diurnal cycle. The extent of the lift and fall is dependent on the diurnal temperature range, which is at a maximum during warm months and a minimum during cold months. This dampened effect is most obvious in June 2016 (Figure 4.29) where between the 22nd and 24th air temperature fluctuates less than 2 $^{\circ}$C, much less than any other time over the two weeks shown and coincides with a constant acceleration of -0.10 ms^{-2} which is more likely a period of no acceleration or movement and a product of the slightly off centred placement of the accelerometer

4.7.3 Summary

Whereas previous sections indicated that microseisms and Earth tides have an effect on the Bramley Drive site throughout the soil profile, the effect of temperature on diurnal ground movement is restricted to near the surface. Accelerometer measurements indicate that the Z-axis follows a daily cycle of rising and falling, with its amplitude dependent on the magnitude of the temperature change. The larger the temperature change over a day, the larger the amplitude of the Z-axis. This is due to two primary effects, one being the amount of available solar radiation and the other, the moisture of the soil. Due to the tilt of the Earth, summer months are exposed to much more insolation due to the angle of Sun rays, compared to in winter months, thus increasing the energy budget at the surface which in turn is used to heat the soil. The moisture content is dependent primarily on rainfall, which is much more common in winter months. The moisture content effect is due to the thermal properties of water, which needs a larger amount of energy to heat a given amount compared to air, while conversely loosing heat much slower than air. Thus when water infills soil pore space near the surface, temperature change throughout the day will be dampened.

CHAPTER 5

EARTH TIDE PHASE AND AMPLITUDE AT TIMES OF SLOPE FAILURE

5.1 INTRODUCTION

After interpreting the borehole inclinometer at the Bramley Drive site, it is clear that there is a diurnal effect of the Earth tides, particularly in an east-west direction. Further, all major movements observed within the borehole inclinometer occurred at times when the predicted rate of vertical Earth tide displacement (velocity) was at a maximum, as well as when predicted horizontal displacement was near or following its maximum. This occurs when the TGP of both the Moon and Sun were about to or had just changed direction (Chapter 4). Therefore, it is possible that the risk of slope failure at Bramley Drive may be higher at these times. This hypothesis was examined further.

Going back to August 1979, when the initial failure of the Bramley Drive Landslide occurred, past Moon phases, as well as predicted vertical and horizontal displacement by Earth tides were calculated using CALSKY™ (Figure 5.1 and Figure 5.2). As previously explained in Section 4.3, these predicted displacements are formed by the TGP of the Moon and Sun. Being that August follows the June Solstice, the maximum TGP occurs at night due to the Earth tilt at that time. Figure 5.1 also shows how the amplitude of these displacements are influenced by the Moon lunar phase, with the period of the full Moon returning the highest displacements both vertically and horizontally.

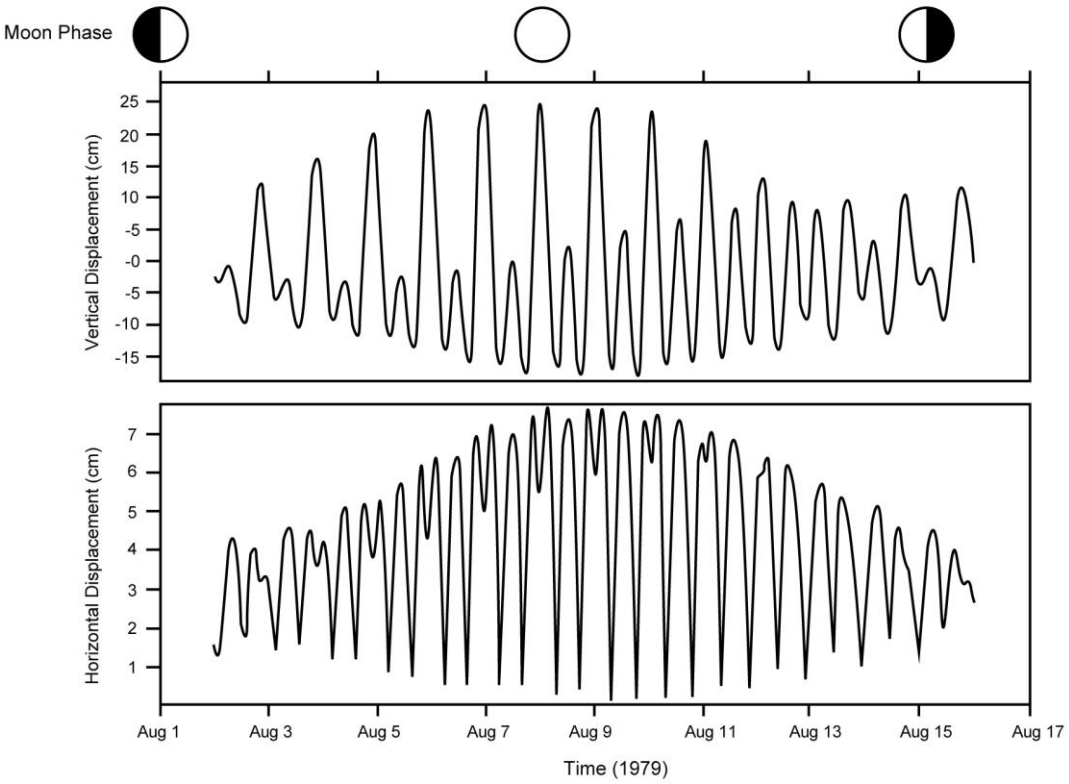

Figure 5.1: Predicted vertical and horizontal displacements, as well as lunar phases at Omokoroa Peninsula for the beginning of August 1979.

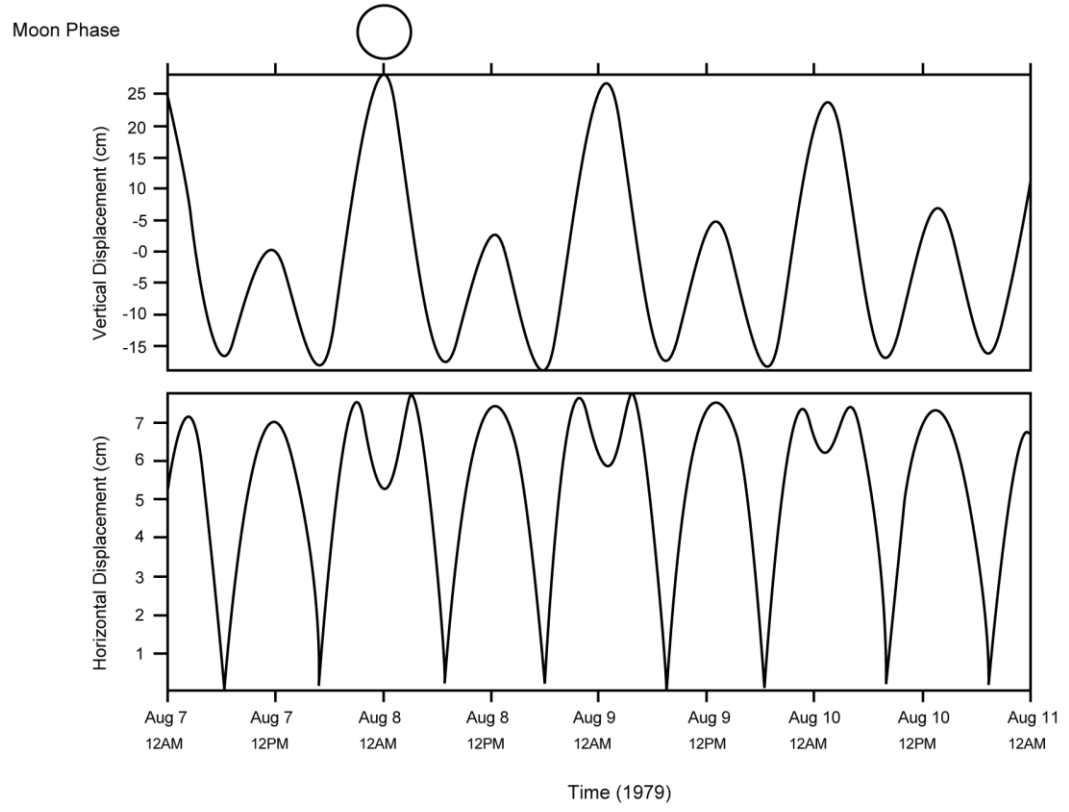

Figure 5.2: Predicted vertical and horizontal displacements, as well as lunar phases at Omokoroa Peninsula over 4 days in August 1979.

Fortuitously, the failure times of the two major Bramley Drive Landslides in 1979 were recorded in the investigation report completed by T&T (Gulliver & Houghton, 1980).

These predicted tidal displacements were calculated using CALSKY™ and failure times were overlain in

Figure **5.3**. Beginning with the initial failure that occurred at approximately 11:00 on the 9th of August 1979, the similar trend of the rate of vertical displacement being close to maximum velocity, as well as horizontal displacement almost reaching maximum is observed.

What is surprising for this time however is that it occurred near noon and not in the middle of the previous night as the TGP was predicted to be much greater with vertical displacement being over 40 cm at its maximum compared to less than 20 cm, with correspondingly greater rates of change (Figure 5.2).

The second failure, which occurred only one day later at around 05:00 on the 11th of August 1979 once again occurs at a time of maximum vertical velocity, although this time in a negative direction. Horizontal displacement again was at a point where there was a direction change, and just like the vertical displacement it was opposite, this time occurring as the Earth rotated away from the full Moon.

Failure at the site didn't occur for the next 32 years, finally reactivating on the 11th of May 2011. Unfortunately, the following investigation report didn't not specify a time for the failure, unlike the previous T&T report (Keam & Milner, 2011). There was, however, an interview of a neighbour by the local newspaper that commented that it happened around "lunchtime" (Hunter, 2011). While being an ambiguous time, where many would assume it being at noon, due to the interviewee being a mother with a new-born, any time leading up to noon could be a possibility. While a failure time of 12:00 deviates a lot from what was happening with the Earth tides in 1979, a more reasonable time of 10:00 shows an almost identical trend as the second failure that occurred on the 11th of August 1979. Although the Bramley Drive site did fail again in 2012, no time was recorded and there was no other evidence to indicate a time, the three largest failures show remarkably similar patterns of Earth tide conditions, occurring just before or just after maximum horizontal strain and maximum vertical stress.

Given the consistent pattern at Bramley Drive, a database of specific times of other documented landslides was compiled to determine if the same pattern held elsewhere. This was much harder than expected, as many newspaper articles, as well as worldwide landslide databases only record the day a failure occurred and do not include the time, which was not exact enough to be able to relate the failures to the Earth tides diurnal fluctuations. However, a few landslides could be found with sufficient data. Fortunately, the video platform YouTube™ had an unexpected assortment of dash-cam and amateur footage of landslides occurring with local times etched onto the video (Appendix 2), which could be linked with news articles of the landslide to determine approximate locations and times for slope failures. This provided additional case studies to analyse.

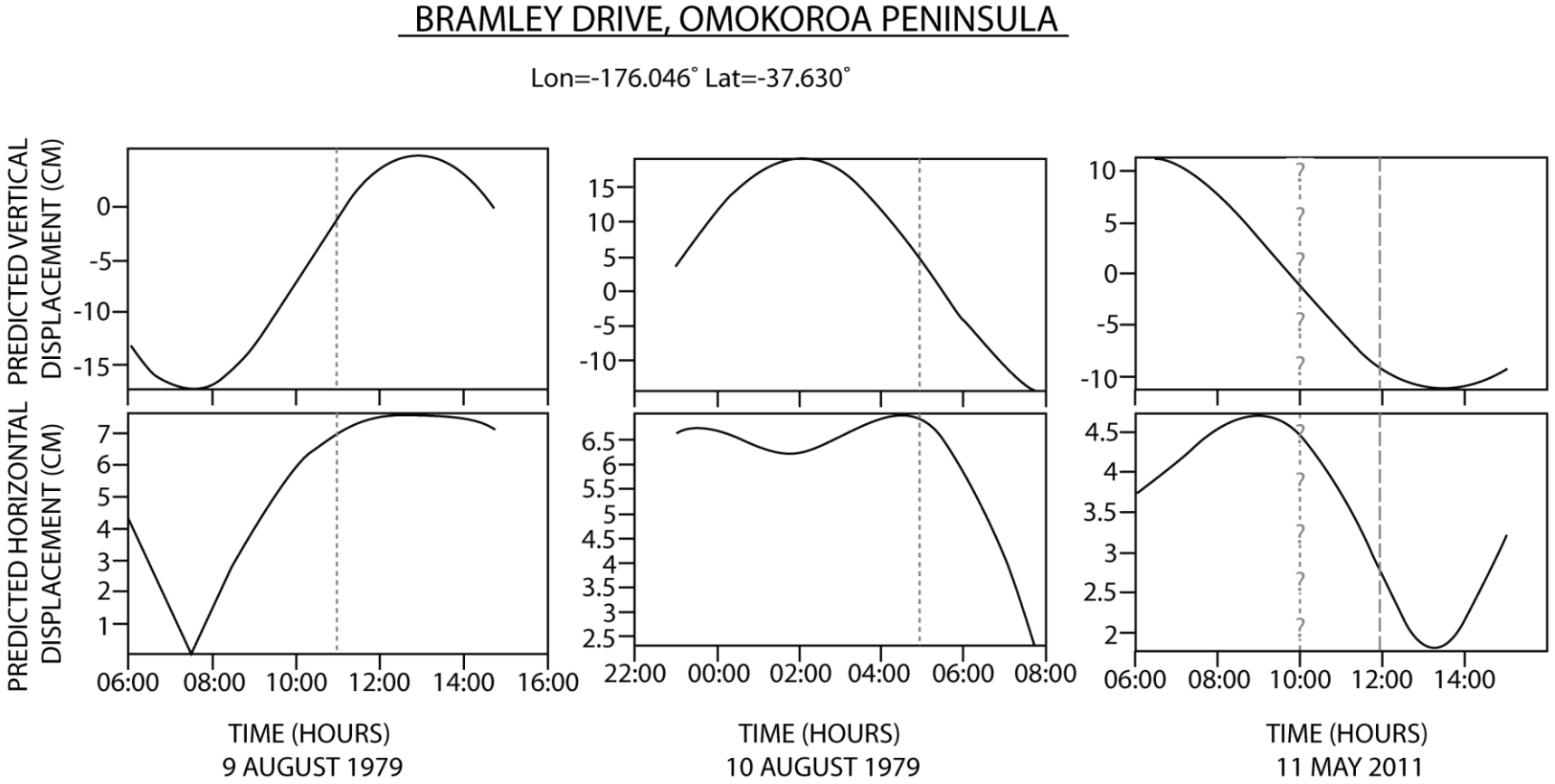

Figure 5.3: Predicted vertical and horizontal displacements at Omokoroa Peninsula around the time of the multiple slope failures at the Bramley Drive site, with grey dotted line giving approximate time of failure event. Note dashed grey line (right) represents "lunchtime" as per newspaper article (Hunter, 2011) , stating when the event may have occurred, compared to the question marked grey dashed line which is what time would agree with the other failures (left & middle) onsite. Earth tide displacements at Omokoroa generated by CALSKY™

A well-documented New Zealand slope failure, was the Abbotsford landslide in Dunedin (Figure 5.4) that occurred at approximately 9 pm on the 8th of August 1979 after several weeks of slow movements, resulting in a ~5 million m^3 block slide (Hancox, 2008) and was the largest landslide in a urban environment in New Zealand's history.

Its failure mechanism was said to be caused by weak clay layers at a 7° dip and a long-term rise in groundwater levels due to a leaking water main, as well as increased rainfall over the previous decade. What's interesting however, is the time and date of the final failure, especially in comparison to the Bramley Drive site. The Abbotsford Landslide occurred the night before the first Bramley Drive slope failure (

Figure **5.3**), at a time where predicted vertical velocity was at a maximum, as well as where predicted horizontal displacement was near its maximum (Figures 5.1, 5.2 and 5.4). While the Earth tides acting on New Zealand over these few days in August 1979 are not likely to have caused the Bramley Drive and Abbotsford landslides, the similar patterns at the times of the slope failures may be more than just coincidence.

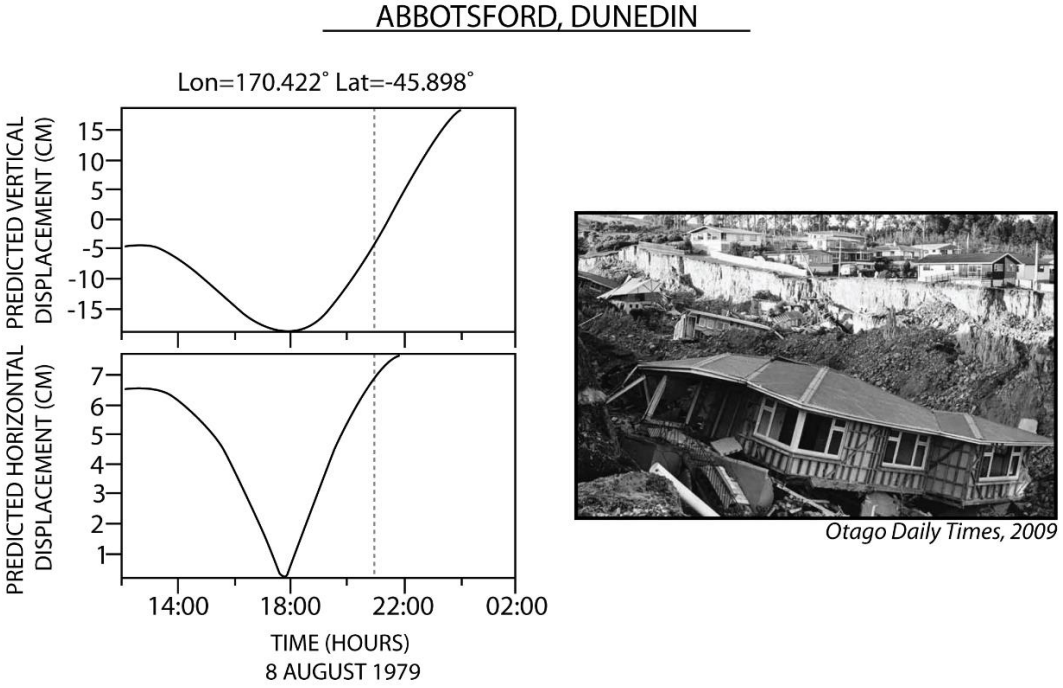

Figure 5.4: Predicted vertical and horizontal displacements at Abbotsford, Dunedin around the time of the large block slide failure, occurring at approximately 9 pm, 8th August 1979 (grey dashed line). Earth tide displacements generated by CALSKY™.

Considering other examples from around the world, including multiple different failure types including a rock topple, slump, translational slide and complex failure to flow failures (Figure 5.5 & Figure 5.6), most slope failures analysed showed a consistent

pattern of the Earth tides producing a high vertical velocity and near maximum horizontal displacement at the time of failure.

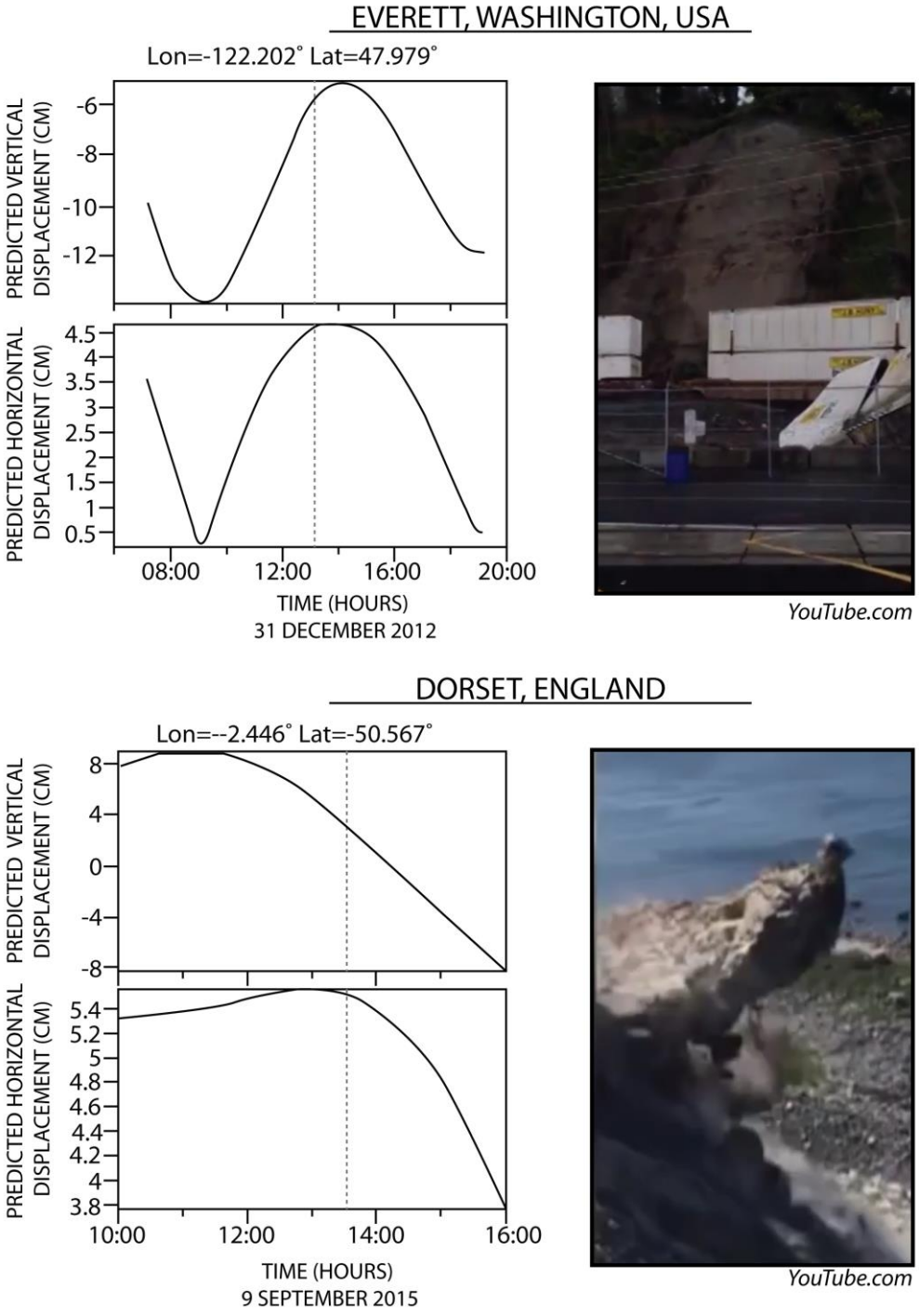

Figure 5.5: Predicted vertical and horizontal displacements at Everett, USA (above) where a translational slide derails a moving locomotive after recent heavy rainfall and Dorset, England (below) where a rock topple is observed by onlookers. Note: grey dotted line giving approximate time of failure event. Earth tide displacements generated by CALSKY™.

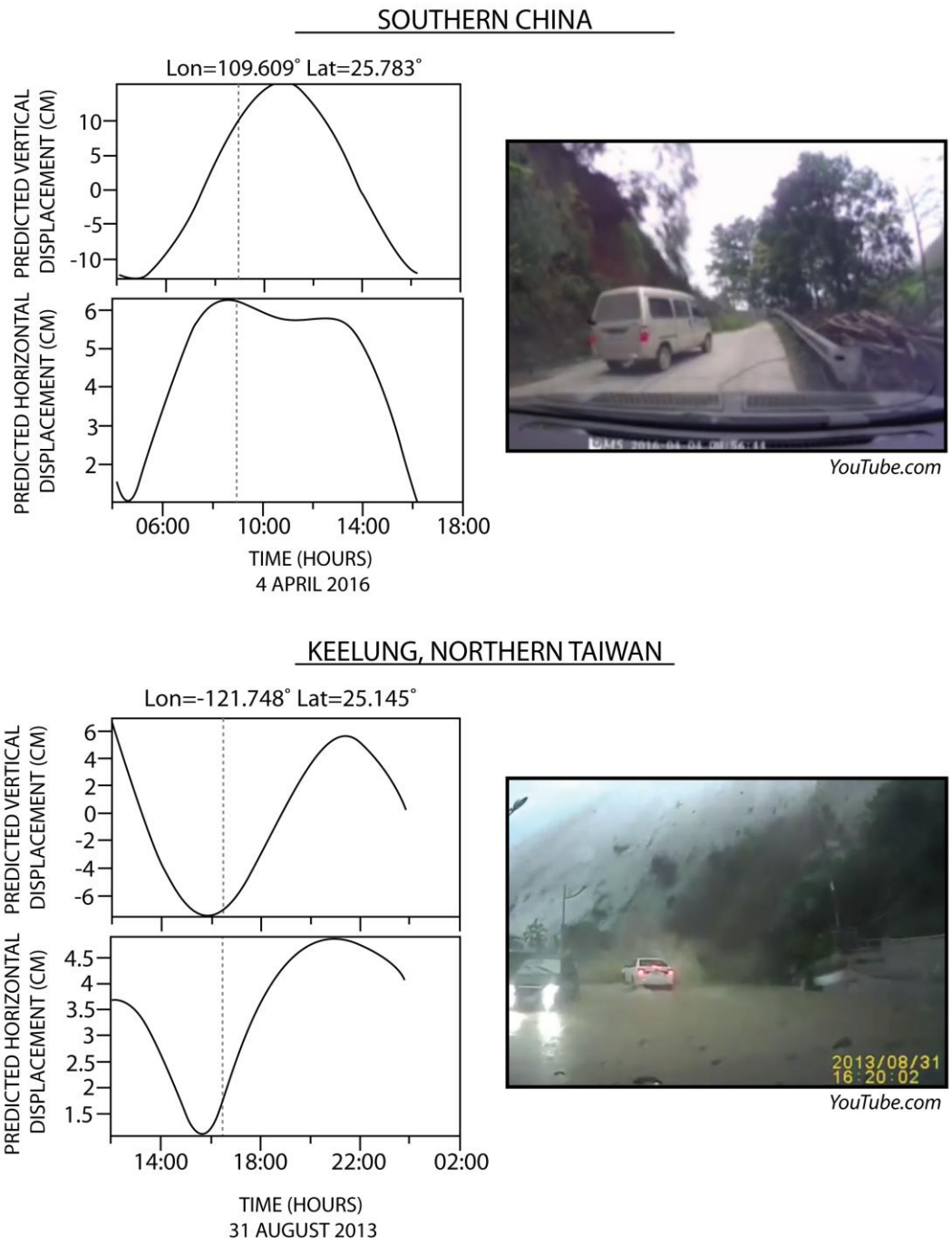

Figure 5.6: Predicted vertical and horizontal displacements near Southern China (above) where a translational slide almost hits two vehicles after recent heavy rainfall and Keelung, Taiwan (below) where a complex failure and flow covers a highway, bringing with it large boulders that almost crush traffic. Note: grey dotted line giving approximate time of failure event. Earth tide displacements generated by CALSKY™.

Of the four examples shown, the large rockfall from Badouzih, Leelung, in northern Taiwan deviates from the consitent pattern noted eariler. Instead is is almost the opposite, being near the maxium negative displacement, while having almost no horizontal displacement. Fourtunatley this rockfall has been studied, likely because of the viral video of a car almost being crushed by a roughly 150 t boulder (Wei *et al.*, 2014).

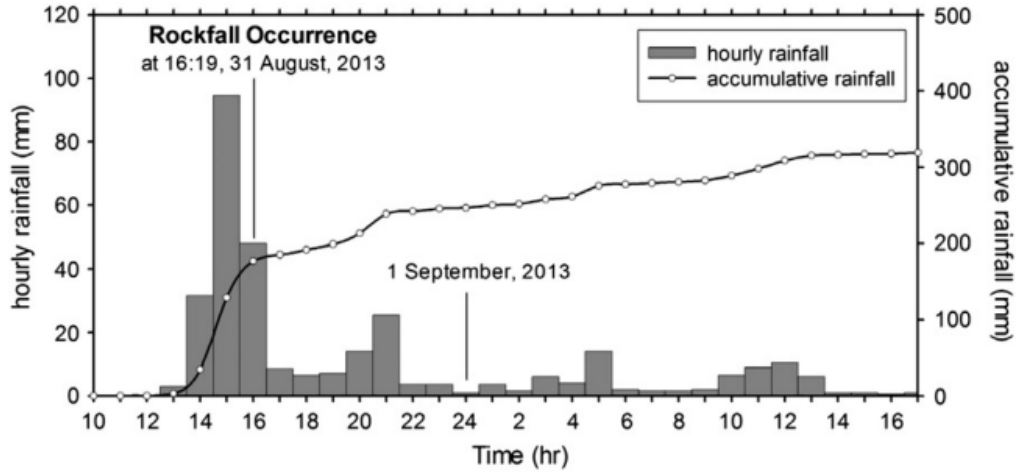

Figure 5.7: Rainfall pattern of local rain gauge during 31th August – 1st September 2013 (Wei *et al.*, 2014).

The rock fall occurred during the Typhoon Kongrey, with short-term rainfall of roughly a 100-year recurrence period (Ching-Fang Lee *et al.*, 2016), with rainfall reaching 94.5 mm/h between 15:00-16:00 (Figure 5.7)(Wei *et al.*, 2014; Ching-Fang Lee *et al.*, 2016). Both reports are of the opinion that intense rainfall accelerated the natural weather process, eroding highly weathered bedrock along discontinuities, with this same material known to fail during high-intensity rainfall events.

For this case, other influences triggered the rock falls timing at 16:19 on the 31st of August 2013, not the Earth tides, reaffirming that while Earth tides may contribute to the timing of a landslide if conditions are primed for failure, other contributing factors, namely rainfall intensity and duration have the ability to activate slope instability at any time.

5.2 TIDAL INFLUENCE ON EARTHQUAKE POTENTIAL

The concept of Earth tides affecting ground movement is not new, with multiple published papers reporting borehole strain and tiltmeter measurements in response to Earth tides (Levine & Harrison, 1976; Linde *et al.*, 1993; Kohl & Levine, 1995);

however, the potential for Earth tides to trigger earthquakes has started to gain momentum more recently.

The concept of tidal triggering of earthquakes was first proposed by Schuster (1897) and was greeted with intense scrutiny. However, with the rapid increase in computing power and accurate instrumentation in the late 20th century, Earth tides could finally be widely modelled. Earthquake prediction was attempted by Beaumont and Berger (1974) by monitoring seismic p velocity (V_p) and its positive effect on both tilt and strain tides when a reduction is noted, effectively inducing dilantancy. Since then, various papers have attempted to provide clear evidence of earthquake triggering by the Earth tides with mixed success. Métivier *et al.* (2009) reported a clear correlation (with ~99% confidence) that earthquakes occur more often when the ground is uplifted by the Earth tide, reducing the normal stresses in the lithosphere (Figure 5.8). It is also stated this trend is larger for smaller and shallower earthquakes and suggest an event is slightly more probable (~0.5-1.0%) when tidal displacement is at its maximum.

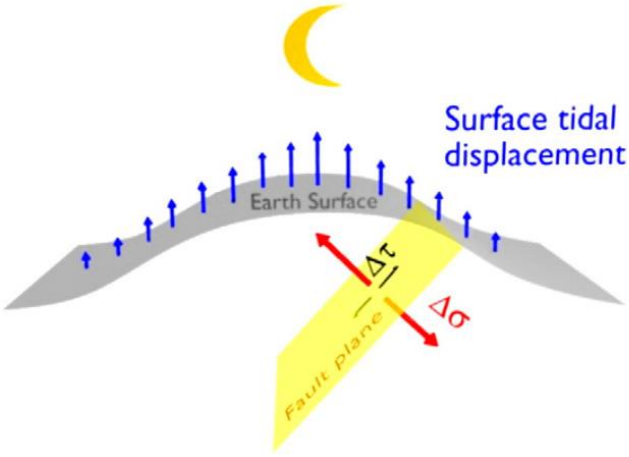

Figure 5.8: Solid tide stress variations within the Earth, as well as a fault plane (Métivier *et al.*, 2009). The diagram suggests tidal stress variations normal to the fault (Δσ) are larger than tidal shear stresses on the fault (Δτ), thus probable to induce failure.

The most recent paper linking tidal stress with the triggering of earthquakes by Ide *et al.* (2016) concludes that periods of high tidal stress increases the likelihood of large earthquakes, suggesting that minor rock failure may expand into gigantic rupture with an accompanying increase in tidal stress. Unlike similar papers that investigated the tidal phase in relation to triggering, Ide *et al.* (2016) attempted to investigate the possible effects of the tidal stress amplitude, since tidal stress amplitude is variable and not always regular. They argued that simple phase analysis with fixed periods may not be an effective technique in examining the effect of tidal stress on seismicity.

5.3 The possible link between Earth tides and slope failure

What I propose is a link between tidal strain and slope failure, similar to how multiple scientists have attempted to find a definitive link between Earth tides and the possibility of earthquake triggering (Métivier *et al.*, 2009; Ide *et al.*, 2016).

Where my hypothesis differs is the reliance on horizontal displacement and its connection with shear stress within the soils, and less about the total vertical displacement caused by the gravitational pull on the Moon and Sun (Figure 5.9).

Moon *et al.* (2015a) suggests that the tilt changes observed in the borehole inclinometer are due to successive layers volcanic tephras with contrasting elastic properties that may cause significant exaggeration of the overall strain. This stems from previous work by Kohl and Levine (1995) showing strain-induced tilt tides can be as much as 75% of the strain tide.

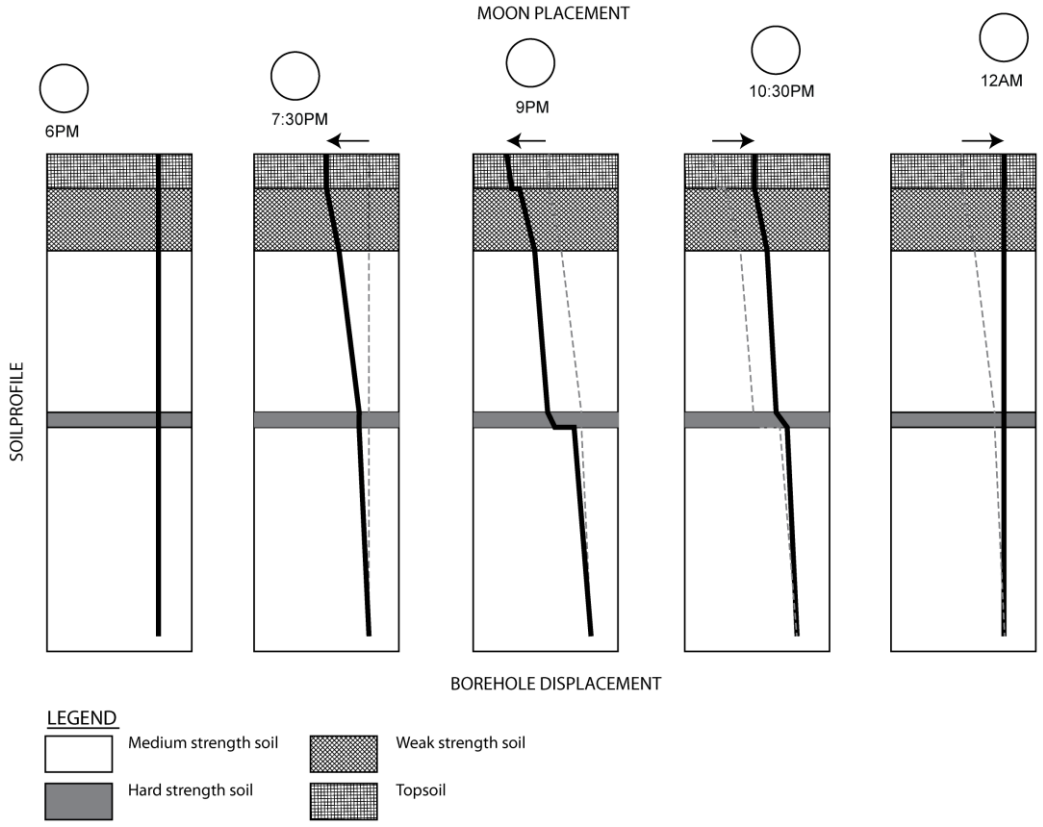

Figure 5.9: Sketch diagram showing the effect of horizontal shear stress caused by horizontal strain induced by the tidal pull of the Moon. Note borehole is static around 18:00 as horizontal and vertical displacement would be zero, as the Earth rotates, horizontal stress increases as the location is pulled toward the Moon, reaching a maximum at 21:00. As the Earth continues to rotate, the Moon begins to locate itself over the location, thus horizontal stress begins to decrease as the Moon's tidal pull exerts only a vertical stress.

While not the direct cause of slope failure, I suggest that under the right circumstances, a change in Earth tide direction and its accompanying predicted horizontal displacement change as the Earth rotates toward or away from an area with high TGP may be the final trigger for an "at risk" slope that is already preloaded and ready to fail.

Elevated ground water or increased pore water pressure by ongoing and heavy rain preceding failure, cyclic loading caused by anthropogenic or natural vibrations, crack propagation caused by shrink-swell soils, defrosting or salt crystallization, along with multiple other factors all may contribute to slope instability, leading to the triggering effect of Earth tides.

CHAPTER 6

CONCLUSIONS

6.1 BACKGROUND SUMMARY AND OBJECTIVES

The Bramley Drive landslide located on the Omokoroa Peninsula, is a slope at risk of future failure. Various work by many researchers (Gulliver & Houghton, 1980; Wyatt, 2009; Keam & Milner, 2011; Cunningham, 2012; Moon *et al.*, 2013; Moon *et al.*, 2015a; Steinborn, 2015; Kluger *et al.*, 2016; Mills, 2016) tend to agree that highly sensitive volcanic tephras are the primarily cause of failure, usually due to an increase in pore water pressure.

What has not been widely researched at the Bramley Drive site, is all of the other potential processes that may contribute to diurnal ground displacement in the unfailed material behind the landslides headscarp. Recent work by the University of Waikato and the University of Bremen, Germany noted in a recent conference paper (Moon *et al.*, 2015a) that a borehole inclinometer that was originally installed to measure if any shear surface may be forming in the problematic Pahoia Tephras was recording measurable deviations when measured on different days. This sparked an interest in the possibility of the borehole fluctuating throughout the same day which it did. Measurable displacement was occurring in a borehole near the headscarp of a landslide with equipment that is supposed to be used to measure cumulative change over days, weeks, months or even years, not hours.

These variations were presumed to be formed by solid Earth tides, which are the semi-diurnal movements in the Earth due to the gravitational attraction of the Moon and Sun. However measured strain was two orders of magnitude greater than predicted Earth tide strain, with a defined elliptical motion.

Unravelling the unknown cause(s) of these exaggerated diurnal solid Earth tide strains at the Bramley Drive landslide was the aim of this thesis, and by following the objectives outlined in Chapter 1, a possible hypothesis has been proposed.

6.1.1 Summary of research findings

Processes that contribute to the daily ground movements at the Bramley Drive Site have been interpreted and discussed in Chapter 4 and Chapter 5, with each section concluding with a summary of that processes suggested contribution.

6.2 PROPOSED DIURNAL PROCESSES CAUSING GROUND MOVEMENT AT OMOKOROA PENINSULA

As stated previously, previous work suggests that unknown factors contribute to the exaggerated ground movements observed at the Bramley Drive site located on the Omokoroa Peninsula. This thesis investigated multiple cyclic and non-cyclic processes, including microseisms, Earth tides, insolation, rainfall and temperature, all of which do contribute to the observed ground movements.

6.2.1 Below the surface

Moon *et al.* (2015a) was correct is suggesting Earth tides may have been observed within the borehole inclinometer readings, as Sections 4.3 and 4.4 show correlations with predicted Earth tide north-south, east-west displacements that occur throughout a lunar cycle, and the direction at which the borehole inclinometer measured tilt. Multiple illustrations in these sections show the tide generating potential (TGP), which is the pulling force acting on the Earth by the Moon and Sun affect Omokoroa on the days where continuous borehole inclinometer readings were completed over 12 hours (15th of April 2016) and 25 hours (14-15th of November 2016). Figure 4.15 and Figure 4.19 show the location of Omokoroa, the sun and the Moon on these days and illustrate how and why vertical displacement increased when Omokoroa was in line with the moon on either side of Earth and horizontal displacement increased as it is pulled towards or away from the moons pull, then relaxed once either directly under the Moon, thus no horizontal strain or on the sides of Earth perpendicular to the Moon.

The elliptical shape of the TGP as it pulls on Omokoroa (in a north-south east-west space) was found to be similar to the recorded north-south, east-west displacements observed in the borehole inclinometer recordings in Figure 4.18 and Figure 4.23, which indicate the borehole will fluctuate east as the Moon rises and west as the Moon sets. However, what this didn't explain is why deviations throughout the borehole are different sizes, in fact due to the low sensitivity of the inclinometer used, north-south, east-west displacement of the borehole should not be observed, as the 43 m borehole

should move as one continuous unit making it impossible to record a deviation from an initial recording.

To explain these sharp tilt changes throughout the borehole on the recorded dates, they were compared to a stratigraphic log of a core drilled in close proximity to the borehole used with the inclinometer. With the sites highly heterogeneous, volcanic based stratigraphy of various ages it is thought that sharp changes in soil strength and structure between each layer may be an outlet for where the pressure caused by the strain created by tidal forces is relieved. Areas that include, but are not limited to unit boundaries, paleosols and the characteristic "sensitive" clay-rich layer located in the lower Pahoia Tephra show recorded tilt change, dependent on the time of day, contributing to cumulative deviation throughout the borehole.

Periods of little to no movement correlate to the Earth tide having a low vertical velocity, which are usually at the same times as no horizontal displacement. Times where horizontal displacement are at maxima are times at which the TGP of the Moon and Sun change directions. This quick change in direction, caused by the location of the Moon and Sun correlate with the periods where noteworthy tilt change occurs and may be times where the amount of tidal strain was enough to form a shear surface that over time could increase with successive diurnal tides. This is suggestion is due to recorded data from both April and November 2016 not completely returning to the same location it began every 12.5 to 25 hours (lunar day).

While Earth tides are observed in the borehole inclinometer and primarily explain ground displacement beneath the surface, results from the on-site accelerometer provide additional cyclic processes that contribute to ground movement at the Bramley Drive site at the surface.

6.2.2 At the surface

Cyclical behaviour was observed within all three components (X, Y, Z) of the on-site accelerometer, and recorded both one-second data as well as ten-minute averaged data.

The one-second data showed the presence of possible primary microseisms caused by waves breaking on the open coast of Matakana Island. Infragravity waves microseisms were also inferred by identifying wave periods of approximately 90 s. While these microseisms are recorded at the surface, these primary waves would be felt throughout the Bramley Drive site. While primary microseisms contribute to crack growth in rocky

cliffs, due to the location and non-brittle geology, it was determined that microseism contribution to diurnal ground displacement at the Bramley Drive site would be minimal.

As for the 10-minute averaged data, air and soil temperature, along with rainfall and solar radiation were correlated with the Z-axis (elevation). Accelerometer measurements indicate that the Z-axis follows a daily cycle of rising and falling, with its amplitude dependent on the magnitude of temperature change. This is due to two primary effects, one being the amount insolation determining the energy available for heating, and the soil moisture controlling the rate of heating. Hence, drier soils in the summer display a larger temperature change than wet soils in the winter.

6.3 RESEARCH BENEFITS

The proposed hypothesis that tidal stress caused by the TGP of the Sun and Moon, may exaggerate ground displacement and possibly causing minor (usually temporary) shear surfaces at depths where there are changes in soil strength and structure, as well as changes in Earth tide direction and accompanying predicted horizontal displacement change possible being the final trigger for an "at risk" slope that is already preloaded and ready to fail would be beneficial when considering more likely times that the slope may fail.

At risk slopes already on the brink of collapse due to elevated ground water or increased pore water pressure by ongoing and heavy rain preceding failure, cyclic loading caused by anthropogenic or natural vibrations, crack propagation caused by shrink-swell soils, defrosting or salt crystallization, may be more likely to fail at times where the Moon's maximum TGP nears or follows a chosen location. This is due to the increased vertical velocity that forces the surface to move either in a positive or negative direction at a much faster rate than the rest of the semi-diurnal cycle, while also being a point where horizontal strain in a predominantly east-west direction is nearing or leaving its maximum.

6.4 SUGGESTIONS FOR FUTURE WORK

As section 1.2 suggests, literature regarding an exaggeration of the Earth tides caused by unknown cyclic factors resulting in ground movement was minimal when preparing this thesis. Also, the ground movements recorded in the borehole inclinometer were unexpected. Therefore, this thesis is seen as a starting point for additional work to

further investigate and unravel each cyclic process found total contribution to the exaggerated Earth tide. Further research efforts could involve:

- Additional days where continuous recordings of the borehole inclinometer are taken place on days of interest. Possibly at each Moon phase or the Earth solstice's and equinox's in an attempt to further understand vertical and horizontal amplitude and its effect of the degree of ground movement at the site;
- The installation of additional accelerometer at the seaward coast of Matakana Island would be useful to compare with the existing accelerometer, as well as the deployment of a wave buoy off the coast of Matakana Island to record the local gravity and infragravity waves.
- The installation of thermal probes and moisture meters at varying depths from the surface behind the headscarp. This would confirm or refute assumptions made in this thesis in regards to temperature fluctuations within the soil being dampened with depth, as well as the effects of insolation and soil moisture content on surface displacements.

REFERENCES

Abu-Hamdeh, N. H. (2003). Thermal properties of soils as affected by density and water content. *Biosystems Engineering, 86*(1), 97-102.

Adams, P. N., Storlazzi, C. D., & Anderson, R. S. (2005). Nearshore wave-induced cyclical flexing of sea cliffs. *Journal of Geophysical Research-Earth Surface, 110*(F2), 19.

Agnew, D. (2015). Earth Tides. In G. Schubert (Ed.), *Treatise on Geophysics* (2nd ed., pp. 151-178): Elsevier.

Ardhuin, F., Stutzmann, E., Schimmel, M., & Mangeney, A. (2011). Ocean wave sources of seismic noise. *Journal of Geophysical Research: Oceans, 116*(C9).

Arthurs, J. M. (2010). *The nature of sensitivity in rhyolitic pyroclastic soils from New Zealand.* thesis, The University of Auckland.

Arya, P. S. (2001). Soil temperatures and heat transfer. In J. R. Holton (Ed.), *Introduction to Micrometeorology* (2nd ed., Vol. 79, pp. 420): Academic Press.

Barmettler, A. (2016). *Solid Earth tide*. Retrieved December, 2016, from http://www.calsky.com/cs.cgi/Calendar/3/6?obs=81483635011045.

Beaumont, C., & Berger, J. (1974). Earthquake Prediction: Modification of the Earth tide tilts and strains by dilatancy. *Geophysical Journal of the Royal Astronomical Society, 39*(1), 111-121.

Bhatt, K. M. (2014). Microseisms and its impact on the marine-controlled source electromagnetic signal. *Journal of Geophysical Research: Solid Earth, 119*(12), 8655-8666.

Bossolasco, M., Cicconi, G., & Eva, C. (1973). On microseisms recorded near a coast. *Pure and Applied Geophysics, 103*(1), 332-346.

Brain, M. J., Rosser, N. J., Norman, E. C., & Petley, D. N. (2014). Are microseismic ground displacements a significant geomorphic agent? *Geomorphology, 207*, 161-173.

Briggs, R. M., Hall, G. J., Harmsworth, G. R., Hollis, A. G., Houghton, B. F., Hughes, G. R., Morgan, M. D., & Whitbread-Edwards, A. R. (1996). *Geology of the Tauranga Area.* Department of Earth Sciences, University of Waikato.

Brooks, S. M., Spencer, T., & Boreham, S. (2012). Deriving mechanisms and thresholds for cliff retreat in soft-rock cliffs under changing climates: Rapidly retreating cliffs of the Suffolk coast, UK. *Geomorphology, 153–154*, 48-60.

Byers, H. R., Moses, H., & Harney, P. J. (1949). Measurement of rain temperature. *Journal of Meteorology, 6*(1), 51-55.

Cessaro, R. K. (1994). Sources of primary and secondary microseisms. *Bulletin of the Seismological Society of America, 84*(1), 142-148.

Ching-Fang Lee, Ting-Chi Tsao, Lun-Wei Wei, & Huang, W.-K. (2016). *The case study of Badouzih rockfall in northern Taiwan: mechanism, numerical simulation and hazard assessment*. Presented at the 13th Congress INTERPRAEVENT 2016.

Cleveland, R. B., Cleveland, W. S., McRae, J. E., & Terpenning, I. (1990). STL: A seasonal-trend decomposition procedure based on loess. *Journal of Official Statistics, 6*(1), 3-73.

Crozier, M., & Eyles, R. (1980). *Assessing the probability of rapid mass movement*. Presented at the Third Australia–New Zealand Conference on Geomechanics.

Cunningham, M. J. (2012). *Sensitive rhyolitic pyroclastic deposits in the tauranga region: Mineralogy, geomechanics and microstructure of peak and remoulded states.* thesis, The University of Waikato.

Darwin, G. H. (1989). The tides and kindred phenomena in the Solar System. *Science, 8*(208), 911-912.

Doodson, A. T. (1921). The harmonic development of the Tide-Generating Potential. *Proceedings of the Royal Society of London. Series A, 100*(704), 305-329.

Ekman, M. (1993). A concise history of the theories of tides, precession-nutation and polar motion (from antiquity to 1950). *Surveys in Geophysics, 14*(6), 585-617.

Fernandes, M., Denis, A., Fabre, R., Lataste, J.-F., & Chrétien, M. (2015). In situ study of the shrinkage-swelling of a clay soil over several cycles of drought-rewetting. *Engineering Geology, 192*, 63-75.

Gislason, S. R., & Oelkers, E. H. (2003). Mechanism, rates, and consequences of basaltic glass dissolution: II. An experimental study of the dissolution rates of basaltic glass as a function of pH and temperature. *Geochimica et Cosmochimica Acta, 67*(20), 3817-3832.

Glade, T. (1997). *The Temporal and Spatial Occurrence of Rainstorm-triggered Landslide Events in New Zealand: an Investigation Into the Frequency, Magnitude and Characteristics of Landslide Events and Their Relationship with Climatic and Terrain Characteristics.* thesis, Victoria University of Wellington.

Glade, T., Crozier, M., & Smith, P. (2000). Applying probability determination to refine landslide-triggering rainfall thresholds using an empirical "Antecedent Daily Rainfall Model". *pure and applied geophysics, 157*(6-8), 1059-1079.

GNS Science. (n.d). *Bramley Drive slip, Omokoroa*. Retrieved January 2016, from https://vml.gns.cri.nz/asset-bank/action/viewAsset?id=106298&index=5&total=34&categoryId=1100&categoryTypeId=1&collection=Bay%20of%20Plenty&sortAttributeId=0&sortDescending=false.

Golyandina, N., & Korobeynikov, A. (2014). Basic singular spectrum analysis and forecasting with R. *Computational Statistics & Data Analysis, 71*, 934-954.

Goring, D. G., & Walters, R. A. (2002). Ocean ‐ tide loading and Earth tides around New Zealand. *New Zealand Journal of Marine and Freshwater Research, 36*(2), 299-309.

Graham, S. (1991). *Clouds & radiation*. Retrieved January, 2016, from http://earthobservatory.nasa.gov/Features/Clouds/.

Gulliver, C. P., & Houghton, B. F. (1980). *Omokoroa Point Land Stability Investigation.* Tauranga County Council, Tonkin & Taylor Ltd. 54p.

Hancox, G. T. (2008). The 1979 Abbotsford Landslide, Dunedin, New Zealand: a retrospective look at its nature and causes. *Landslides, 5*(2), 177-188.

Haubrich, R., Munk, W., & Snodgrass, F. (1963). Comparative spectra of microseisms and swell. *Bulletin of the Seismological Society of America, 53*(1), 27-37.

Houghton, J. T. (1996). *Climate change 1995: The science of climate change: contribution of working group I to the second assessment report (SAR) of the Intergovernmental Panel on Climate Change (IPCC)*. Cambridge University Press.

Hsi, G., & Nath, J. H. (1970). Wind drag within simulated forest canopies. *Journal of Applied Meteorology, 9*(4), 592-602.

Hunter, M. (2011). Massive landslide in Omokoroa, *Bay of Plenty Times*.

Ide, S., Yabe, S., & Tanaka, Y. (2016). Earthquake potential revealed by tidal influence on earthquake size-frequency statistics. *Nature Geoscience, 9*(11), 834-837.

Jentzsch, G. (1997). Earth tides and ocean tidal loading. In H. Wilhelm, W. Zürn & H.-G. Wenzel (Eds.), *Tidal Phenomena* (Vol. 66, pp. 145-171): Springer Berlin Heidelberg.

Johnson, J. W., & Council on Wave Research (Compiler) (1951). *Proceedings of First Conference on Coastal Engineering: Long Beach, California, October 1950*: The Engineering Foundation.

Keam, M., & Milner, D. (2011). *Bramley Drive landslip hazard assessment.* Western Bay of Plenty District Council, Tonkin & Taylor Ltd.

Kedar, S., Longuet-Higgins, M., Webb, F., Graham, N., Clayton, R., & Jones, C. (2008). The origin of deep ocean microseisms in the North Atlantic Ocean. *Proceedings of the Royal Society of London A: Mathematical, Physical and Engineering Sciences, 464*(2091), 777-793.

Kiehl, J. T., & Trenberth, K. E. (1997). Earth's annual global mean energy budget. *Bulletin of the American Meteorological Society, 78*(2), 197-208.

Kluger, M. O., Moon, V. G., Kreiter, S., Lowe, D. J., Churchman, G. J., Hepp, D. A., Seibel, D., Jorat, M. E., & Mörz, T. (2016). A new attraction-detachment model for explaining flow sliding in clay-rich tephras. *Geology, G38560.1, first published on December 8, 2016*.

Kohl, M. L., & Levine, J. (1995). Measurement and interpretation of tidal tilts in a small array. *Journal of Geophysical Research: Solid Earth, 100*(B3), 3929-3941.

Lal, R., & Shukla, M. K. (2004). Soil Structure. In *Principles of soil physics* (pp. 736): CRC Press.

Levine, J., & Harrison, J. C. (1976). Earth tide strain measurements in the Poorman Mine near Boulder, Colorado. *Journal of Geophysical Research, 81*(14), 2543-2555.

Linde, A. T., Gladwin, M. T., & Johnston, M. J. (1993). Borehole strain measurements of solid-earth-tidal amplitudes. In *The Loma Prieta, California Earthquake of October 17, 1989 - Preseismic Observations* (Vol. 1550, pp. 81-85): U.S. Geolgical Survey.

Longuet-Higgins, M. S. (1963). The generation of capillary waves by steep gravity waves. *Journal of Fluid Mechanics, 16*(1), 138-159.

Macky, G. H., Latimer, G. J., & Smith, R. K. (1995). Wave climate of the western Bay of Plenty, New Zealand, 1991–93. *New Zealand Journal of Marine and Freshwater Research, 29*(3), 311-327.

McCully, J. G. (2006). *Beyond the moon: A conversational common sense guide to understanding the tides*. New Jersey: World Scientific.

Métivier, L., de Viron, O., Conrad, C. P., Renault, S., Diament, M., & Patau, G. (2009). Evidence of earthquake triggering by the solid earth tides. *Earth and Planetary Science Letters, 278*(3–4), 370-375.

Mills, P. (2016). *Failure mechanisms in sensitive volcanic soils in the Tauranga Region, New Zealand.* thesis, The University of Waikato.

Milner, D., & Taylor, D. (2014). *Bramley Drive landslip hazard assessment.* Western Bay of Plenty District Council, Tonkin & Taylor Ltd.

Moon, V., de Lange, W., Garae, C., Mörz, T., Jorat, M., & Kreiter, S. (2015a). *Monitoring the landslide at Bramley Drive, Tauranga, NZ*. Presented at the 12th Australia New Zealand Conference on Geomechanics.

Moon, V. G., Cunningham, M. J., Wyatt, J. B., Lowe, D. J., Mörz, T., & Jorat, M. E. (2013). *Landslides in sensitive soils, Tauranga, New Zealand*. Presented at the 19th New Zealand Geological Society (NZGS) Geotechnical Symposium.

Moon, V. G., Lowe, D. J., Cunningham, M. J., Wyatt, J. B., de Lange, W. P., Churchman, G. J., Mörz, T., Jorat, M. E., Kreiter, S., & Kluger, M. O. (Compiler) (2015b). *Sensitive pyroclastic-derived halloysitic soils in northern New Zealand: interplay of microstructure, minerals, and geomechanics*. International Workshop on Volcanic Rocks and Soils (3-21). Lacco Ameno, Ischia Island, Italy.

New Zealand Geotechnical Society (NZGS). (2005). *Guidelines for the field classification and description of soil and rock for engineering purposes*. New Zealand Geotechnical Society.

New Zealand. Ministerial Inquiry into the Auckland Power Supply, F. (1998). *Auckland power supply failure 1998: the report of the Ministerial inquiry into the Auckland Power Supply* Ministerial inquiry into the Auckland Power Supply Failure. Wellington: Wellington: Ministry of Commerce.

O'Reilly, M. P., & Brown, S. F. (Compiler) (1991). *Cyclic loading of soils: From theory to design*. Glasgow, UK: Blackie.

Oliver, R. C. (1997). *A geotechnical characterisation of volcanic soils in relation to coastal landsliding on the Maungatapu Peninsula, Tauranga, New Zealand.* thesis, The University of Canterbury.

Pidwirny, M. (2006). Earth-Sun relationships and insolation. In *Fundamentals of Physical Geography* (2 ed.). University of British Columbia Okanagan.

Pitjeva, E. V., & Standish, E. M. (2009). Proposals for the masses of the three largest asteroids, the Moon-Earth mass ratio and the Astronomical Unit. *Celestial Mechanics and Dynamical Astronomy, 103*(4), 365-372.

Poulsen, S. K. (2009). *Tidal deformation of the Solid Earth - A finite difference discretization.* thesis, University of Copenhagen.

Quayle, A. M. (1984). The climate and weather of the Bay of Plenty Region. *NZ Meteorological Service, Wellington*, p. 56.

Rafiq, M., & Santos, M. C. (Compiler) (2004). *Study of eastern Canadian coastal site displacement due to ocean tide loading using a GPS network in Atlantic Canada*. Joint AGU/CGU Scientific Meeting. Montreal, Canada.

Romagnoli, C., Zerbini, S., Lago, L., Richter, B., Simon, D., Domenichini, F., Elmi, C., & Ghirotti, M. (2003). Influence of soil consolidation and thermal expansion effects on height and gravity variations. *Journal of Geodynamics, 35*(4–5), 521-539.

Salih Kirkgöz, M. (1990). An experimental investigation of a vertical wall response to breaking wave impact. *Ocean Engineering, 17*(4), 379-391.

Schulz, W. H., Kean, J. W., & Wang, G. (2009). Landslide movement in southwest Colorado triggered by atmospheric tides. *Nature Geoscience, 2*(12), 863-866.

Schuster, A. (1897). On Lunar and Solar Periodicities of Earthquakes. *Proceedings of the Royal Society of London, 61*(369-377), 455-465.

Selby, M. J. (1993). *Hillslope materials and processes* (2nd ed.). Oxford, England: Oxford University Press.

Steinborn, B. (2015). *Multidisciplinary soil characterization of a coastal Omokoroa peninsula, NZ slope sequence, prone to slope failure, using correlations of in-situ and laboratory data.* thesis, University of Bremen.

Torrance, J. K. (2014). Chemistry, Sensitivity and Quick-Clay Landslide Amelioration. In J.-S. L'Heureux, A. Locat, S. Leroueil, D. Demers & J. Locat (Eds.), *Landslides in Sensitive Clays: From Geosciences to Risk Management* (pp. 15-24). Dordrecht: Springer Netherlands.

Wei, L.-W., Chen, H., Lee, C.-F., Huang, W.-K., Lin, M.-L., Chi, C.-C., & Lin, H.-H. (2014). The mechanism of rockfall disaster: A case study from Badouzih, Keelung, in northern Taiwan. *Engineering Geology, 183*, 116-126.

Wilhelm, H., Zürn, W., & Wenzel, H.-G. (1997). Tidal phenomena. *Lecture Notes in Earth Sciences, Berlin Springer Verlag, 66*.

Wyatt, J. (2009). *Sensitivity and clay mineralogy of weathered tephra-derived soil materials in the Tauranga region.* thesis, The University of Waikato.

Young, A. P., Adams, P. N., O'Reilly, W. C., Flick, R. E., & Guza, R. T. (2011). Coastal cliff ground motions from local ocean swell and infragravity waves in southern California. *Journal of Geophysical Research: Oceans, 116*(C9), 11.

Young, A. P., Guza, R. T., Adams, P. N., O'Reilly, W. C., & Flick, R. E. (2012). Cross-shore decay of cliff top ground motions driven by local ocean swell and infragravity waves. *Journal of Geophysical Research: Oceans, 117*(C6), 12.